Synthesis and Electrochemical Cycling of Nanostructured Ti_2C Mxene as Anode Materials for Lithium-ion Batteries

This thesis is submitted to the Department of Mechanical Engineering of Chittagong University of Engineering & Technology as a partial fulfillment of requirement for the degree of

MASTERS OF SCIENCE IN MECHANICAL ENGINEERING

Submitted by

Mohammad Nezam Uddin Chy

Student ID: 20MME028P

Supervised by

Dr. Md. Arafat Rahman

Professor, Department of Mechanical Engineering

Department of Mechanical Engineering

Chittagong University of Engineering & Technology

Approval

The thesis titled **"Synthesis and Electrochemical Cycling of Nanostructured Ti_2C MXene as Anode Materials for Lithium-ion Batteries"** submitted by Mohammad Nezam Uddin Chy, ID- 20MME028P, Session: 2020-2021 has been accepted as satisfactory in partial fulfillment of the requirement for the degree of Masters of Science (M.Sc.) in Mechanical Engineering dated on 14th August 2024.

Board of Examiners

1.	**Dr. Md. Arafat Rahman** Professor, Department of Mechanical Engineering, CUET	**Chairman** **(Supervisor)**
2.	**Head** Department of Mechanical Engineering, CUET	**Member** **(Ex-Officio)**
3.	**Dr. Sheikh Muhammad Humayun Kabir** Professor, Department of Mechanical Engineering, CUET	**Member**
4.	**Dr. Md. Sanaul Rabbi** Professor, Department of Mechanical Engineering, CUET	**Member**
5.	**Dr. Md. Shamimur Rahman** Professor, Department of Glass and Ceramic Engineering, RUET	**Member** **(External)**

List of Publications

Parts of this M. Sc Engineering thesis have already been published in referred scientific journals as follows:

1. **Mohammad Nezam Uddin Chy**, Md. Arafat Rahman, Jin-Hyuk Kim, Nirjhor Barua and Wasif Abu Dujana."**MXene as Promising Anode Material for High-Performance Lithium-Ion Batteries: A Comprehensive Review**". *Nanomaterials*. 2024; 14(7):616. Impact factor = 5.3, Cite Score =Q1. Published: 31 March 2024.

Declaration

I hereby confirm that my work is represented in this thesis, which has been done after registration for the degree of M.Sc. in Mechanical Engineering at CUET and has not been previously included in a thesis or dissertation submitted to this or any other institution for a degree, diploma, or other qualification.

Name: Mohammad Nezam Uddin Chy

Student ID: 20MME028P

Date: ……

Acknowledgment

I would like to pray to Allah without whose blessing we couldn't complete this thesis and my heartfelt appreciation goes out to everyone who helped me finish this thesis.

Above all, I owe a debt of gratitude to my supervisor Dr. Md. Arafat Rahman, Professor, Department of Mechanical Engineering, CUET, for his essential advice during the research process. His knowledge, tolerance, and insightful feedback were invaluable in helping to shape this thesis.

I express my heartfelt gratitude to Prof. Dr. Mohammad Mizanur Rahman, Head of the ME Department at CUET, for his invaluable help throughout the research process. I express my sincere gratitude to all members of my thesis committee, namely Dr. Sheikh Muhammad Humayun Kabir and Dr. Md. Sanaul Rabbi, Professor, Department of Mechanical Engineering, CUET, and Dr. Md. Shamimur Rahman, Professor, Department of Glass and Ceramic Engineering, RUET, for their invaluable time, expertise, and critical assessment of this work

I would like to thank Dr. Md. Saiful Islam, Associate Professor, Department of Glass and Ceramic Engineering, BUET and Mr. Radheshyam Nath Jisu, Assistant Professor, CUET for their support and co-operation in this thesis work.

My heartfelt gratitude goes out to the Department of Mechanical Engineering's faculty and staff for creating an engaging learning environment and giving me access to valuable resources that helped me in my research.

Dedication

This dissertation is dedicated to my beloved parents and my siblings who are the source of my inspiration and strength.

Abstract

By offering a high energy density, long cycle life, and relatively low self-discharge rates, LIBs have become the preferred choice for powering everything from smartphones to electric vehicles. Their ability to be rapidly charged and discharged while maintaining a compact and lightweight form has also made them essential in renewable energy systems, where they facilitate the storage of solar and wind energy. The electrochemical performance of a LIB greatly depends upon the anode material. The essential requirements for excellent anode material of Lithium-ion batteries (LIBs) are high safety, minimal volume expansion during the lithiation/de-lithiation process, high cyclic stability, and high Li+ storage capability. However, most of the anode materials for LIBs, such as graphite, SnO_2, Si, Al, $Li_4Ti_5O_{12}$, etc., have at least one issue. Hence, creating novel anode materials continues to be difficult. Broad adoption has already been started of MXenes materials in various energy storage technologies such as super-capacitors and batteries due to the increasing versatility of the preparation methods as well as the ongoing discovery of new members. Few MXenes have been investigated experimentally as anode of LIBs till date due to their distinct active voltage windows, large power capabilities, and longer cyclic life. Here, Ti_2C MXene was synthesized by using an efficient NaOH etching technique. The surface appearance, structural composition, and crystalline structure were assessed using X-ray diffraction, SEM, and EDX analysis. The as-synthesized MXene were used as negative electrode in LIB and electrochemical performance were evaluated. First cycle charge-discharge capacities are found 658.02 $mAhg^{-1}$ and 419.11 $mAhg^{-1}$ respectively with an initial columbic efficiency of 63.6% and excellent capacity retention of 259.1 $mAhg^{-1}$ is obtained after 100 cycles at a current density of 50 mAg^{-1}. The excellent cyclic performance and stability of this cell are attributed to the unique properties of MXene structure such as high electronic conductivity, low operating voltage, large surface area and fast Li ion diffusion characteristics.

সারসংক্ষেপ

উচ্চ শক্তির ঘনত্ব, দীর্ঘ চক্র জীবন এবং তুলনামূলকভাবে কম স্ব-স্রাবের হার অফার করার মাধ্যমে, স্মার্টফোন থেকে বৈদ্যুতিক যানবাহন পর্যন্ত সবকিছু পাওয়ার জন্য LIBs পছন্দের পছন্দ হয়ে উঠেছে। একটি কমপ্যাক্ট এবং লাইটওয়েট ফর্ম বজায় রাখার সময় তাদের দ্রুত চার্জ এবং ডিসচার্জ করার ক্ষমতা তাদের পুনর্নবীকরণযোগ্য শক্তি ব্যবস্থায় অপরিহার্য করে তুলেছে, যেখানে তারা সৌর এবং বায়ু শক্তি সঞ্চয় করার সুবিধা দেয়। একটি LIB এর ইলেক্ট্রোকেমিক্যাল কর্মক্ষমতা অ্যানোড উপাদানের উপর নির্ভর করে। লিথিয়াম-আয়ন ব্যাটারির (LIBs) চমৎকার অ্যানোড উপাদানগুলির জন্য প্রয়োজনীয় প্রয়োজনীয়তাগুলি হল উচ্চ নিরাপত্তা, লিথিয়েশন/ডি-লিথিয়েশন প্রক্রিয়া চলাকালীন ন্যূনতম আয়তনের প্রসারণ, উচ্চ চক্রীয় স্থিতিশীলতা এবং উচ্চ Li^+ স্টোরেজ ক্ষমতা। যাইহোক, LIB-এর জন্য বেশিরভাগ অ্যানোড উপাদান, যেমন গ্রাফাইট, SnO_2, Si, Al, $Li_4Ti_5O_{12}$, ইত্যাদির অন্তত একটি সমস্যা আছে। অতএব, অভিনব অ্যানোড উপকরণ তৈরি করা কঠিন হতে চলেছে। প্রস্তুতির পদ্ধতির ক্রমবর্ধমান বহুমুখিতা এবং সেইসাথে নতুন সদস্যদের চলমান আবিষ্কারের কারণে সুপার-ক্যাপাসিটর এবং ব্যাটারির মতো বিভিন্ন শক্তি সঞ্চয় প্রযুক্তিতে ইতিমধ্যেই MXenes উপকরণগুলির ব্যাপক গ্রহণ শুরু হয়েছে। কিছু MXenes তাদের স্বতন্ত্র সক্রিয় ভোল্টেজ উইন্ডো, বৃহৎ বিদ্যুতের ক্ষমতা এবং দীর্ঘ চক্রাকার জীবনের কারণে আজ পর্যন্ত LIB-এর অ্যানোড হিসাবে পরীক্ষামূলকভাবে তদন্ত করা হয়েছে। এখানে, Ti_2C MXene একটি দক্ষ NaOH এচিং কৌশল ব্যবহার করে সংশ্লেষিত হয়েছিল। এক্স-রে ডিফ্র্যাকশন, এসইএম এবং ইডিএক্স বিশ্লেষণ ব্যবহার করে পৃষ্ঠের চেহারা, কাঠামোগত গঠন এবং স্ফটিক কাঠামো মূল্যায়ন করা হয়েছিল। হিসাবে-সংশ্লেষিত MXene এলআইবিতে নেতিবাচক ইলেক্ট্রোড হিসাবে ব্যবহার করা হয়েছিল এবং ইলেক্ট্রোকেমিক্যাল কর্মক্ষমতা মূল্যায়ন করা হয়েছিল। প্রথম চক্রের চার্জ-ডিসচার্জ ক্যাপাসিটি পাওয়া যায় যথাক্রমে 658.02 $mAhg^{-1}$ এবং 419.11 $mAhg^{-1}$ যার একটি প্রাথমিক কলম্বিক দক্ষতা 63.6% এবং 259.1 $mAhg^{-1}$ এর চমৎকার ক্ষমতা ধারণ করা হয় 100 চক্রের পরে 50 mAg^{-1} কারেন্টে। এই কোষের চমৎকার চক্রীয় কর্মক্ষমতা এবং স্থায়িত্ব MXene গঠনের অনন্য বৈশিষ্ট্য যেমন উচ্চ ইলেকট্রনিক পরিবাহিতা, কম অপারেটিং ভোল্টেজ, বৃহৎ পৃষ্ঠ এলাকা এবং দ্রুত লি আয়ন বিচ্ছুরণ বৈশিষ্ট্যের জন্য দায়ী।

Table of Content

Approval ..... **i**

List of Publications ..... **ii**

Declaration ..... **iii**

Acknowledgment ..... **iv**

Dedication ..... **v**

Abstract ..... **vi**

সারসংক্ষেপ ..... **vii**

LIST OF FIGURES ..... **xii**

List of Tables ..... **xvi**

Chapter 01 Introduction **17**

1.1 Background 17

1.2 Electrochemical Energy Storage 18

1.2.1 Capacitor *19*

1.2.2 Supercapacitor *20*

1.2.3 Fuel cell *21*

1.2.4 Battery *22*

1.3 Working of LIB 26

1.4 Motivation and objectives 28

1.5 Thesis Outline 29

Chapter 02 Literature Review **31**

2.1 Background 31

2.2 Structural Framework of MXene 33

2.3 Synthesis of MXene....36
2.3.1 Wet Chemical Etching....36
2.3.2 Molten Salt Etching....38
2.3.3 Electrochemical Etching....39
2.4 MXenes in LIBs....40
2.4.1 Mono Transition Metal MXene as Anode of LIBs....41
2.4.2 Double Transition Metal MXene (DTM) as anode of LIBs....54
2.4.3 Composite MXene as anode of LIBs....58
Chapter 03 Materials and Methods....90
3.1 Background....90
3.2 List of Equipment and Chemicals....91
3.2.1 Lithium Cobalt oxide....92
3.2.2 Battery Electrode Separator....93
3.2.3 Ti_2AlC Powder....94
3.2.4 NaOH etchant....95
3.2.5 Precision electronic balance machine....96
3.2.6 Lithium battery-grade electrolyte....96
3.2.7 Ethanol....97
3.2.8 Acetone....98
3.2.9 Distilled water....98
3.2.10 Electric Oven....99
3.2.11 Magnetic Stirrer....99
3.2.12 Coin cell case....100
3.2.13 Hydraulic crimping machine....100

3.2.14 Battery tester *101*

3.2.15 CV and EIS tester *101*

3.2.16 Multimeter *102*

3.2.17 SEM machine *102*

3.2.18 XRD machine *103*

3.3 Etching 103

3.4 Filtration, Heating, and Ball milling 103

3.5 Characterization 105

3.5.1 X-ray diffraction (XRD) *105*

3.5.2 Scanning electron microscopy (SEM) *106*

3.5.3 Energy-Dispersive X-ray Spectroscopy (EDX) *107*

3.6 Anode Preparation 108

3.7 Coin Cell assembly 109

3.8 Electrochemical Measurement 110

Chapter 04 Result and Discussion 111

4.1 Background 111

4.2 XRD Analysis 112

4.3 SEM and EDX analysis 113

4.4 Electrochemical analysis 117

4.5 Summery 123

Chapter 05 Conclusion and Future Study 124

5.1 Conclusions 124

5.2 Limitations 125

5.3 Future Study 125

REFERENCES **128**

LIST OF FIGURES

Figure 1.1 Comparative performance graph of various energy storage devices[8]....19

Figure 1.2 Illustration of supercapacitor[12].....21

Figure 1.3 Illustration of fuel cell working [13]......22

Figure 1.4 Working of LIB.[15].....27

Figure 2.1 A typical M_2X MXene structure without termination.....34

Figure 2.2 (a) Schematic diagram of the synthesis of MXene by HF etching (Adapted from [62,63]) and (b) The synthesis and structure diagram of $Ti_3C_2T_x$ MXene (Adapted from [64]).....37

Figure 2.3 Schematic of the etching and delamination process (Adapted from [35]) (a) Molten salts etching. (b)Electrochemical etching (Adapted from [68]).....39

Figure 2.4 Schematic representation of MXene as anode of LIB.....41

Figure 2.5 SEM image of Ti_2C MXene [23].....42

Figure 2.6 a) SEM and b) TEM image of Ti_3C_2 MXene [76].....43

Figure 2.7 Schematic of 3D macroporous PANI@M-Ti3C2Tx frame-works using PS spheres as templates (Adapted from [81]).....44

Figure 2.8 (a) Schematic illustration of the preparation process of SnS/Ti3C2Tx MXene and (b) Cycling performance of SnS/Ti3C2Tx , pure Ti3C2Tx and commercial SnS at a current rate of 500 mAg^{-1}. (Adapted from [84]).....46

Figure 2.9 (a) Schematic drawing depicting the preparation steps of OMPDA/$Ti_3C_2T_x$ composite and(b) Cycling stability of OMPDA/$Ti_3C_2T_x$ anode.(Adapted from [87]).47

Figure 2.10 (a) SEM of Nb_2AlC and (b) SEM of Nb_2C [92].....49

Figure 2.11 (a) Charge-discharge cycle performance curves of different samples at different current densities, (b) Cycle stability curves of different samples at current density of 500 mA/g. [95].....51

Figure 2.12 Representation of structure of (a) ordered DTM and (b) solid solution of MXene. (Two colors of molecules represent two types of transition metals) (Adapted from [44]).....55

Figure 2.13 (a) SEM image of VNbAlC and (b) SEM image of multi-layer VNbCTx [102]. 56
Figure 2.14 Schematic representation of synthesis process of MXene/Metal composite. 59
Figure 2.15 (a) SEM images of pristine Ti_3C_2 MXene. (b) SEM image of as-prepared NiCoLDH/Ti_3C_2 Nanosheets [109]. 60
Figure 2.16 (a) SEM image of Ti_3C_2 (b) SEMimage of Si/Ti_3C_2 [112]. 61
Figure 2.17 Schematic representation of synthesis and cyclic performances of different samples at 0.5 Ag^{-1}. (Adapted from [114]) 62
Figure 2.18 SEM images of (a) the prepared Ti_3C_2 and (b) FeOOH/Ti_3C_2 composite (adapted from [125]**)**. 66
Figure 2.19 Schematic representation of C-TiO_2/Fe_2O_3-Ti_3C_2 MXene with cyclic performance curves at 1 Ag^{-1}. (Adapted from[127]) 67
Figure 2.20 Cyclic performance curves for S-$Ti_3C_2T_x$ MXene with CMC and PVDF binder (Adapted from [142]) 73
Figure 2.21 (a) SEM image of 3D Ti_3C_2; (b) SEM image of 3D Ti_3C_2/Ag [144]. 74
Figure 2.22 Cyclic stability curves of VNbC@VNO-500 and $VNbCT_x$ MXene at 0.1 Ag^{-1}. (Adapted from [154]) 78
Figure 2.23 (a) SEM images of as-etched $Ti_3C_2T_x$ particles and (b) the Ti_3C_2-CNF [170]. 84
Figure 3.1 Battery fabrication and performance measurement process. 90
Figure 3.2 Lithium cobalt oxide cathode. 92
Figure 3.3 Battery electrode separator. 94
Figure 3.4 Ti_2AlC powder. 95
Figure 3.5 Sodium hydroxide pellets. 96
Figure 3.6 Image of electric balance 96
Figure 3.7 Battery electrolyte ($LiPF_6$). 97
Figure 3.8 Image of ethanol. 97
Figure 3.9 Image of acetone. 98

Figure 3.10 Image of distilled water.....98
Figure 3.11 Image of electric oven.....99
Figure 3.12 Image of magnetic stirrer.....99
Figure 3.13 Image of coin cell case.....100
Figure 3.14 Image of a hydraulic crimping machine.....101
Figure 3.15 Image of battery tester.....101
Figure 3.16 Image of CV and EIs tester.....102
Figure 3.17 Image of a multimeter.....102
Figure 3.18 Etching process under stirring.....103
Figure 3.19 Filtration process of Ti_2C MXene.....104
Figure 3.20 Ball milling process.....104
Figure 3.21 Schematic of Braggs law.....106
Figure 3.22 Schematic diagram of SEM working.....107
Figure 3.23 Anode preparation process.....108
Figure 3.24 CR2032 coin cell preparation process.....109
Figure 4.1 XRD pattern of Ti_2AlC precursor before and after etching.....112
Figure 4.2 a) Low Magnification b) High magnification image of precursor before etching and c) Low Magnification d) High magnification image after etching.....114
Figure 4.3 EDX analysis of Precursor before etching (a,b) after etching (c,d).....115
Figure 4.4 a) Low Magnification b) High Magnification image of anode (c,d) EDX analysis of anode.....116
Figure 4.5 Change of Current and Voltage with respect to Time for 1-20 Charge-Discharge cycles.....117
Figure 4.6 Change of Current and Voltage with respect to Time for 21-40 Charge-Discharge cycles.....118
Figure 4.7 Cycling performance of Ti_2C MXene at 50 mAg^{-1}.....119
Figure 4.8 Cycling performance of Ti_2C MXene at different current densities.....120
Figure 4.9 CV curves at 0.2 mVs^{-1}.....122
Figure 4.10 Comparison with different anode materials.....123

Figure 5.1 Schematic representation of LIB with MXene as anode. 126

List of Tables

Table 2.1 Summery of cyclic performance of mono transition metal MXene as anode of Lithium Ion Batteries. 53

Table 2.2 Summery of Cyclic performance of 2D DTM as anoe of LIB. 57

Table 2.3 Summery of cyclic performance of composite MXene as anode of LIBs.....85

Table 3.1 Equipment and chemicals required for the battery fabrication process 91

Table 3.2 Characteristics of Separator 93

Table 3.3 Characteristics of Ti_2AlC powder.....94

Table 4.1 Comparison of Cycling performance of various anode material 120

Chapter 01

INTRODUCTION

1.1 Background

Global energy consumption has risen rapidly due to the consequence of rising industrialization, technological advancement, and excessive economic expansion in emergent countries. As a result, nonrenewable resources of energy such as natural gas, coal, and oil have degraded at an unsustainable rate. At the same time, the use of this energy emits poisonous gases and pollutes water supplies, posing a threat to human existence while also increasing environmental concerns. Thus, developing fresh, renewable energy sources is vital to mitigating the challenges of energy scarcity and environmental degradation. However, there are significant issues with renewable energy sources because they cannot provide a constant and uninterrupted energy supply [1–3]. For instance, solar panels could be unproductive in overcast conditions, wind turbines are likely to be useless in serene conditions, and renewable energy sources could generate extra power, causing the entire system to be overloaded at times. To count these intermittencies and maintain an optimal equilibrium of energy production and consumption, energy storage systems (ESSs) are considered the most feasible and effective option, with immense promise for optimizing energy management and controlling energy spillage. ESSs are primarily intended to gather energy from multiple sources, convert it, and store it as needed for a variety of applications. The deployment of ESSs commenced almost in the nineteenth century, and they have advanced far enough since then to attain the point where they are currently. ESSs can be categorized according to the type of energy that is preserved, their applications, storage duration, storage efficiency, and so on. The bulk of energy storage methods include flywheel, thermochemical, magnetic,

magneto electric, compressed air, pumped, compressed air, chemical, and hydrogen energy storage, as well as electrochemical and battery energy storage. Of all the energy storage devices available, batteries grab much attention as they are utilized to power practically all electronic devices in a number of applications, including mobile phones, electronic devices, automobiles, consumer health, industrial, and military equipment. A variety of batteries are available, such as lead-acid batteries, nickel-cadmium batteries, nickel-metal-hydride batteries, etc.. However, LIB is more widely accepted since it has a greater specific energy, higher density of energy, superior energy efficiency, better cycle life, and calendar life. Although LIBs have acquired wide adoption and deployment in diverse applications, they still demand further research, advancements, and developments. Since its introduction by Sony in 1991 graphite has served as the primary anode material. The rationale for this is that graphite has various benefits, including low cost, relative abundance, non-toxic properties, and structural stability. However, graphite's theoretical capacity is modest, limiting its use for high-power applications. It has also been discovered that delithiation/lithiation over the cycle process causes a volume change in the material, causing stress on the electrode and compromising cycling stability. Furthermore, the graphite electrode might interact with the electrolyte at low working voltages, causing lithium deposition. This condition not only degrades battery performance but also offers a significant safety risk. To mitigate these issues many novel materials are being investigated for their ability to store lithium reversibly to meet the demands of upcoming large-scale applications like stationary energy storage and fully electric and hybrid vehicles [4–6].

1.2 Electrochemical Energy Storage

Electrochemical energy storage devices utilize electrochemistry to remake chemical energy into electrical energy. These energy storage technologies encompass batteries, supercapacitors, and fuel cells. These energy storage devices offer several advantages compared to other ESS systems such as high energy density (energy

stored per unit volume), scalability, fast charging and discharging (rapid energy delivery), high efficiency and environment friendly [7]. All things considered, the efficiency of electric vehicles, the dependability of electrical grids, and the broad acceptance of renewable energy sources are all made possible by electrochemical energy storage. Fig. 1.1 shows the comparative performance graph of various electrochemical energy storage devices.

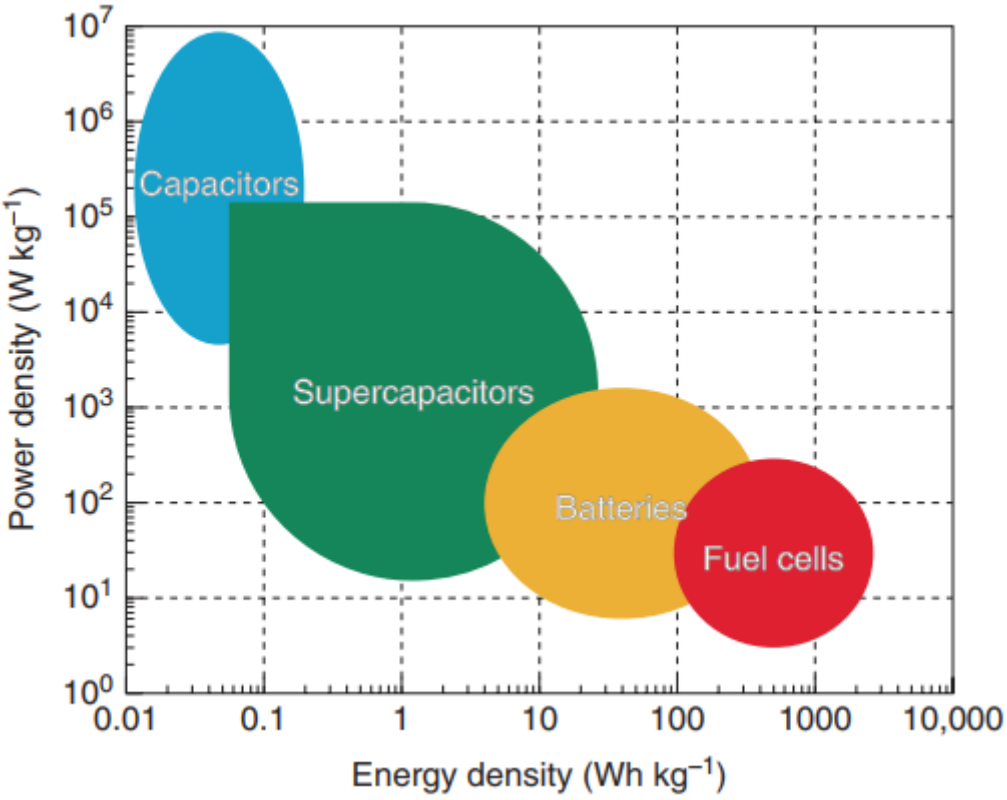

Figure 1.1 Comparative performance graph of various energy storage devices[8].

1.2.1 Capacitor

An electrostatic field is used by a capacitor during charging to store electrical energy. It consists of two metal plates that are positioned closely to one another and are divided by a non-conductive dielectric layer. One metal plate is charged with electricity during the operation when a voltage source is placed across it, while the other plate is charged with the opposite sign. The dimensions of a capacitor and the

distance between its conducting plates define its energy capacity. Capacitors are limited in their ability to handle strong currents because of their extremely low energy density. Their specific energy values are minimal (0.05–5 Wh/kg), despite their great life cycle (50,000 cycles) and specific power (1,000,000 W/kg) [9].

1.2.2 Supercapacitor

Supercapacitors are an intermediary between batteries and traditional electrolytic capacitors. These are electrochemically charged capacitors. Although the supercapacitors' energy storage process differs from that of capacitors, the fundamental equations governing capacitors remain the same. Supercapacitors are called "super" because their capacitance is the order of farad (F), which is higher than that of dielectric capacitors (μF) and electrolytic capacitors (mF). The supercapacitors differ from conventional capacitors in that they feature a very large area between the electrode and the dielectric, with a nanometer-thick dielectric. The structure of a Supercapacitor consists of electrodes and current collectors made of aluminum Instead of using dielectric materials. The distribution of ions close to the surface of the two electrodes stores energy, which is the cornerstone of the SC's operational philosophy. The electrical double layer (EDL) is a space charge zone formed by the two interfaces, as shown in Fig. 1.2. A Supercapacitor is hence electrostatic and does not undergo an electrochemical reaction. The principal advantages of supercapacitors (SCs) include low energy and high power density, fast charging and discharging, energy flow termination upon full charge, low resistance (ESR), extended lifespan response, and long shelf life. The three categories of ESs, such as electrostatic double-layer supercapacitors, pseudo capacitors, and asymmetric supercapacitors [10,11].

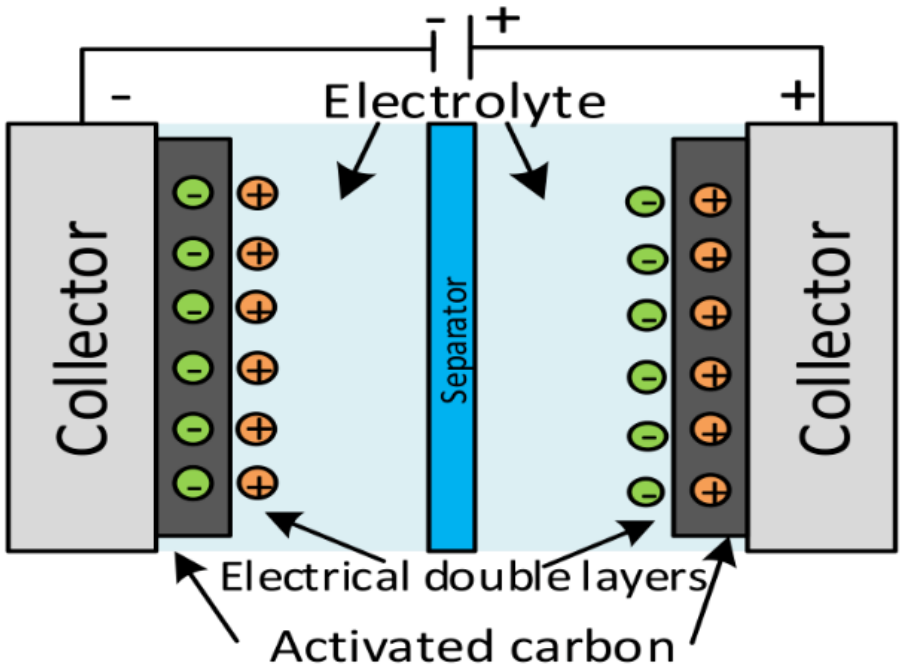

Figure 1.2 Illustration of supercapacitor[12].

1.2.3 Fuel cell

A chemical process is used by a fuel cell to convert a fuel's chemical energy into electrical energy. The most typical fuel for this chemical reaction is hydrogen, which acts as an electrolyte. The reaction requires external sources of fuel (anode side) and oxidant (cathode side), typically oxygen as shown in Fig. 1.3. Fuel cells are among the most promising energy storage technologies due to their potential specific energy of 16,470 Wh/kg for hydrogen and oxygen. Various types of fuel cells are available, such as the over 50% efficient molten carbonate fuel cell (MCFC), the over 50% efficient solid oxide fuel cell (SOFC), the 40–50% efficient alkaline fuel cell (AFC), and the 35–45% efficient proton exchange membrane fuel cell (PEMFC). High energy density, high energy conversion efficiency (without Carnot cycle restrictions), modular design, non-polluting, cheap maintenance, safety, and silence are some of the benefits of HFC. HFC has some drawbacks, including as expensive catalyst and electrolyte costs, low power density, impurity intolerance, and short lifespan [13].

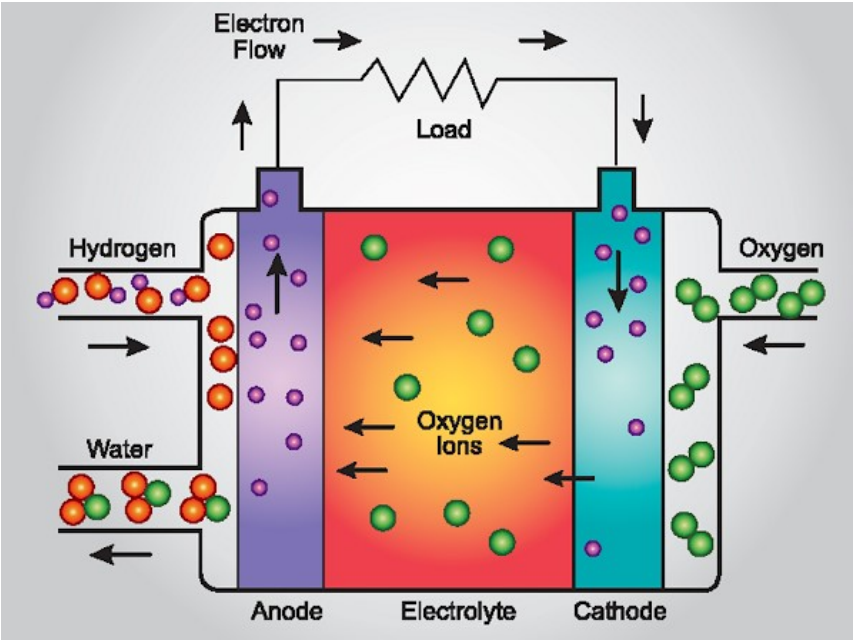

Figure 1.3 Illustration of fuel cell working [13]..

1.2.4 Battery

The batteries are makeup from stacked cells that convert chemical energy to electrical energy and vice versa. The cells of the batteries are electrically connected in series and parallel to supply the desired voltage and current levels. Batteries are classified according to how much power and energy they can hold. The energy and power capacities are fixed throughout the battery design process for the majority of battery types. Other crucial features of a battery include its life cycle, efficiency, operational temperature, level of discharge (level of discharge refers to the degree to which a battery is discharged; in general, batteries are not completely discharged), self-discharge (self-discharge indicates the rate at which a battery discharges), and energy density. As can be observed from fig. 1.1, batteries have established market positions due to their intermediate power and energy properties, which set them apart from supercapacitors and fuel cells. Several batteries are available till now some of them are well matured and some are considered as emerging technologies [4,13].

a) Lead acid battery

A sponge-like lead negative electrode and a lead dioxide positive electrode make up the lead-acid battery. These electrodes are placed in the sulfuric acid electrolyte and are separated by a microporous substance. Although lead-acid batteries are very inexpensive, they demand a lot of room and upkeep. Additionally, their lifespan is shortened and rapidly diminishes if the battery is depleted to less than 30%. As a result, energy density is decreased, which raises capital expenses. In distributed power, renewable energy, and uninterruptible power supply (UPS) systems, they are frequently implemented. A 40 MWh system in Chino, California, is the biggest one that has been erected [6,13].

b) Metal-Air Battery

Aluminum and zinc, two widely accessible metals with high energy density that rescue electrons when oxidized, serve as the anodes in these batteries. Cathodes are typically made of a porous carbon matrix or a metal mesh coated with the proper catalysts. Commonly, the electrolytes are high-quality hydroxide (OH–) ion conductors, like potassium hydroxide (KOH). A solid polymer membrane that has been saturated with KOH or a liquid version could be used as the electrolyte. The smallest and cheapest batteries on the market are metal-air batteries. Additionally, they are environment friendly. The primary drawback, though, is how hard and ineffective it is to electrically recharge these batteries. Rechargeable metal-air batteries have an efficiency of roughly 50% and a limited lifespan of a few hundred cycles; they are currently in the development stage [13].

c) Sodium sulfide battery

The positive and negative electrodes of sodium sulfide battery are made of molten sulfur and sodium, respectively, and are isolated by a solid beta alumina ceramic electrolyte. Just ions of sodium are permitted to proceed through the electrolyte and interact with the sulfur to generate sodium polysulfides. During discharging, the

battery's external circuit conducts electron flow while sodium ions move through the electrolyte, creating roughly 2 V. For this process to occur, the battery is maintained at roughly 300 °C. With a power capability greater than six times their continuous rating, NaS battery cells exhibit a high efficiency of approximately 89%. Because of this feature, the NaS battery can be utilized cost-effectively in applications combining peak shaving with power quality [13].

d) Nickel-cadmium (Ni-Cd) batteries

One of the most developed and commonly utilized technologies is that of Ni-Cd batteries, which were created in 1899 by Swedish inventor Waldemar Jungner. Industrial Ni-Cd batteries were produced at Jungner's firm in Sweden in 1906. The United States of America began producing these batteries in 1946. The active ingredients in the "pocket type" batteries that were manufactured at the time were nickel and cadmium. In the middle of the 1900s, sintered plate Ni-Cd batteries became more and more popular since they were much smaller than pocket batteries and could handle higher current flows. Nickel powder is infused at temperatures that are beneath the melting point while large pressure is applied to create the plates. Approximately 80% of the pore volume in the very porous plates is produced by this approach. The Ni-Cd battery has spongy nickel oxyhydroxide as the positive electrode, metallic cadmium as the negative electrode, and potassium hydroxide as the electrolyte. A nylon divider keeps the two electrodes apart, preventing direct charge transfer. In the discharge cycle, nickel oxyhydroxide at the positive plate combines with water to form nickel hydroxide, while cadmium at the negative plate reacts to produce cadmium hydroxide. They are commonly used in electrical power applications, as Ni-Cd batteries have a higher life cycle than LA batteries [13].

e) Solid-state batteries (SSBs).

"Solid-state battery" refers to a battery that employs a solid electrolyte rather than a liquid one. Liquid electrolyte batteries and all-solid-state batteries share similar cell

chemistry. Among all-solid-state batteries, the main component is a solid electrolyte, which can be composed of glass, ceramic, polymer, or a combination of these. The discovery of solid electrolytes dates back to the 19th century, but solid-state battery technologies have seen a resurgence in attention due to the advancement of electric cars in the latter half of the 20th and the first part of the 21st. Several well-known manufacturers, including Ford, General Motors, Hyundai, Toyota, and Volkswagen, have already made significant financial investments in SSB tech firms, expecting complete commercial deployment by the first half of the twenty-first century. Solid-state batteries (SSBs) are among the greatest choices for next-generation batteries because of their solid electrolytes' greater power density, thermal stability, and energy density. In addition to addressing safety problems, SSBs can facilitate operation in harsh settings, such as those with temperatures between -50 and 200 ◦C or higher, where organic electrolytes break down because of freezing, boiling, or decomposing [13].

f) Paper batteries

Paper batteries are extremely thin and flexible, mostly composed of carbon nanotubes and paper/cellulose. The only differences between them and conventional batteries are that they don't corrode and only need a minimal amount of housing and casing. They adapt or accommodate themselves into small openings or areas with ease, reducing the total size and weight of the system. They also offer a high degree of flexibility because they can be twisted, bent, or wound any object without needing to follow certain set-up standards. A specifically made carbon nanotube ink is applied to a piece of paper that has been treated with an ionic solution. To function as an anode, a small layer of lithium is layered on the other side of the paper. There are two aluminum rods connected on either side that transport the electricity between the electrodes [13].

g) Lithium-ion batteries

Since 1960, LIBs have been used in a variety of consumer and mobile applications, most notably electric and plug-in cars. Its development has been mostly driven by transportation and mobile applications thus far. In LIB, lithium metal oxide is the cathode, while graphitic carbon is the anode. Organic carbonates are dissolved in lithium salts to form the electrolyte. Compared to other conventional batteries, they exhibit a typical specific power of 150–315 W/kg; nevertheless, their specific energy and life cycle are higher, ranging from 75–200 Wh/kg to 10,000 cycles. Their high cost is attributed to the restricted availability of aluminum resources, despite their excellent efficiency (85–98%) and low self-discharge (0.1–0.3% Energy/day). The improved qualities of the battery's materials, notably the cathode materials that offer high energy density, are directly linked to the lowered energy losses in the battery and the resulting good efficiency outcomes. Recycling these units to be done carefully because some of the old electrolytes are poisonous and lithium is caustic (may catch fire). In comparison to other advanced batteries, Li-ion batteries have the following primary advantages: (a) High energy density (300–400 kWh/m3, 130 kWh/ton); (b) Outstanding efficiency (around 100%). (c) Extensive cycle life (3,000 cycles at 80% discharge depth) [14].

1.3 Working of LIB

A cell of the battery is generally made of

-An anode, sometimes referred to as a negative electrode, is where an oxidation reaction occurs and provides electrons to the load to power it up.

- A cathode, or positive electrode, that is exposed to electrons during an electrochemical resulting in reduction.

- Electrolyte, which transfers ions between the anode and cathode during reactions by acting as a medium.

- An insulator that serving as a protective shield between the cathode and anode to stop short circuits.

Lithium ions move from the cathode (LiCoO2, LiMnO4, and LiFePO4) towards the anode while the charging process is occurring (Figure 4a). A longer path around the external circuit is also taken by electrons as they move from the positive to the negative electrode. The cathode, which is where these electrons and ions mix, is what causes the lithium to deposit. A fully charged battery will not experience any more lithium deposition from ion flow.

Ions travel through the electrolyte backward from the anode to the cathode, which is what causes the battery to discharge. Although it is passing through an external circuit and powering the attached device, the electron flow continues in the same direction. When the battery is running low, lithium deposition appears at the cathode during ions and electrons mixing. When no more ions are able to flow towards the cathode, the battery will be completely drained and will need to be recharged. Fig. 1.4 shows working of LIB.

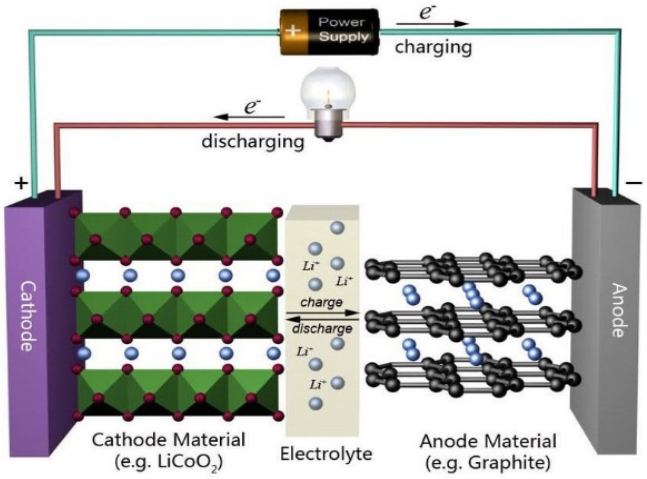

Figure 1.4 Working of LIB.[15].

1.4 Motivation and objectives

Currently, graphite is primarily used in commercial lithium-ion battery anodes. Graphite and other carbon-based materials are preferred in view of their high chemical diffusion coefficient for Li+, high attainable operation potential, superior electrical conductivity, and least volume shifts during Li+ intercalation and de-intercalation. However, the low theoretical capacity of 372 $mAhg^{-1}$, which is insufficient to power long-range EVs, HEVs, and other portable devices, is one of the major limitations of using graphite as an anode material in LIBs [16]. Several high-performance materials have been researched as LIB electrode materials for the near future in order to replace graphite as the anode. Based on how anode interacts with lithium, anode materials for LIB can be categorized into three groups: intercalation, conversion, and alloying [17]. Despite having a long cycle life and a solid structure, most of intercalation materials have a limited capacity [18]. Conversion-based material has high theoretical capacity as compared to graphite. The range of theoretical capacity of conversion-based anode materials ranges from the modest range of 350 $mAhg^{-1}$ for Cu_2S to the elevated range of 1800 $mAhg^{-1}$ for MnP_4 [19].For example, oxides of iron show a very high theoretical capacity of 1007 $mAhg^{-1}$ for Fe_2O_3 and 924 $mAhg^{-1}$ for Fe_3O_4 [20]. MoO_3 also has a high theoretical capacity of 1117 $mAhg^{-1}$ [21]. However, conversion-based materials show voltage hysteresis, Low coulombic efficiency, and very significant volume fluctuations occur during lithiation and delithiation leading to cycle fading [2]. For lithium-ion batteries, alloy-based anodes show promise because of their strong energy capabilities and security aspects. Several alloy anodes showed notable reversible capacity (500–700 mAhg−1) and better coulombic efficiency (80–90%) with an extended cycle lifespan (up to 300 cycles) for example SnO and SnO_2 have a theoretical capacity of 875 and 783 $mAhg^{-1}$ respectively [22]. However, they suffer from a significant initial capacity loss, limited cycle life, and extreme volume change of almost 300% during charge and discharge.

In 2011, selectively removing the "A" elements from their corresponding three-dimensional (3D) MAX phases has resulted in the preparation of a novel class of exfoliated transition metal carbides and carbonitrides known as "MXene". Which have unique lamellar structure. They also have high projected elastic moduli, hydrophilicity, large surface area, short diffusion, and are effective electrical conductors. The electrochemical incorporation of Li ions in between the MXene sheets makes MXene an intriguing material for hybrid electrochemical capacitors and Li-ion battery anodes. Among all MXenes Ti_2CT_x is the lightest MXene that can be used as an anode of LIBs because this type of MXene is an excellent electronic conductor and can tolerate change of volume to a certain degree during cycling which helps to mitigate stress on material and longer the lifespan of batteries. Ti_2C MXene exhibited a stable capacity as an anode of LIBs for more than 100 cycles [23,24].

In this thesis, Ti_2CT_x MXene is considered the anode of high-performance LIBs. Here Ti_2CT_x MXene was synthesized from its precursor, and thereafter systematically explored the electrochemical characteristics of this material as anode of LIBs. Research objectives include the following terms:

- Synthesis of Ti_2C MXene and characterization of as-synthesized MXene by using scanning electron microscope (SEM), X-ray diffraction (XRD), and Energy-dispersive X-ray spectroscopy (EDX).
- Imposing prepared material as the anode of LIBs and investigation of charge-discharge capacity, cyclic life, energy density, specific capacity, calendar life, and internal resistance of assembled LIBs.

1.5 Thesis Outline

This thesis paper titled “Synthesis and Electrochemical Cycling of Nanostructured Ti_2C MXene as Anode Material for Lithium ion Batteries” consists of background studies, fabrication procedures, structural characterization of synthesized materials,

and electrochemical performance investigation when used as an anode material for LIB. The whole thesis is organized in the following ways:

Chapter-01: Introduction

This chapter includes the essence of energy storage systems for utilizing renewable energy as a primary source of energy, types of electrical energy storage systems with their comparative Benefits as well as disadvantages, lithium-ion batteries as promising energy storage technology.

Chapter-02: Literature Review

This chapter represents general overview of MXene surface property and structure with critical analysis. In addition, relevant studies on various synthesis technique of MXene as well as elaborate description of outcomes of various MXene materials as anode of high-performance lithium ion battery.

Chapter-03: Materials and Methodology

This chapter offers comprehensive explanations of the experimental processes, including material synthesis, characterization techniques, electrode preparation, analysis of the electrochemical performance, and descriptions of the equipment and materials used in the experiment.

Chapter-04: Result and Discussion

This chapter includes X-ray diffraction (XRD) patterns, SEM images, and Energy Dispersive Spectroscopy (EDX) spectra analysis and critical reasoning of as prepared Ti_2C MXene nanostructured anode. Additionally, galvanostatic charge discharge cycle, cyclic voltammogram and EIS also analyzed in this section.

Chapter-05: Conclusion and Future Work

This Chapter includes findings and limitations of the work and future recommendation.

Chapter 02

LITERATURE REVIEW

2.1 Background

After extensive investigation and usage, consumers are acquainted with lithium-ion batteries. It is now frequently utilized in electrical appliances and electric automobiles [25,26]. A potential market for electric urban automobiles has developed recently, with producers of mobile devices engaging in a competitive series. Advancements in high-performance lithium-ion batteries, such as high Specific Capacity, energy density, substantial open circuit voltage, and least self-discharge are being prioritized [27–29]. MXenes have future for numerous kinds of energy storage applications due to their improved electrical conductivity, outstanding mechanical strength, and immense surface area. MXene has the chemical formula $M_{n+1}X_nT_x$, where M is a transition metal (i.e., Sc, Ti, V, Zr, Nb, Mo, etc.), X is C or N, and T denotes surface terminal groups (i.e. -O, -OH, and -F). The performance of MXenes in capacitive energy storage is quite encouraging. $Ti_3C_2T_x$, for example, has demonstrated excellent volumetric and gravimetric capacitance as well as outstanding cyclability [30]. In the aqueous H_2SO_4 electrolyte, MXene displays pseudocapacitance due to the reversible surface redox reaction of hydrogen binding. The electric double-layer (EDL) capacitance of MXene is predominant in aqueous salt or ionic liquid electrolytes [31]. When two transition metals are coupled in the MXene structure, a special property of MXenes is triggered into action. In addition to the expected solid solutions, such as $(Ti,Nb)CT_x$, transition metals can also form ordered forms in a single 2D MXene flake. These ordered structures can be created by the assembly of atomic sandwiches of transition metal planes (for n ≥2), like $Mo_2TiC_2T_x$, or by in-plane (n = 1) ordered structures, like $(Mo_{2/3}Y_{1/3})_2CT_x$. A large

number of potential compositions have been anticipated from computational investigations of MXenes and their predecessors. Endless number of nonstoichiometric MXenes synthesis is possible with the creation of solid solutions on M and/or X sites, and it also presents an alluring chance of optimizing characteristics by combining other transition metals or synthesizing carbonitrides. There is continuing research to generate 2D borides and so provide the system with another X component [32,33].

Recently, an electrochemical fluoride-free production technique utilizing dilute hydrochloric acid was disclosed for Ti_2CT_x MXene production [34]. Huang et al. created novel MAX phases and fluorine-free MXenes using molten $ZnCl_2$ salt [35]. By enabling people who are interested in MXenes, however, do not wish to operate in laboratories with any chemicals that include or produce hydrofluoric acid (HF), this method has the potential to considerably expand experimental study on MXenes. A successful use of V_2CT_x MXene as a positive elctrode material for sodium-ion storage has already been developed [36]. It is noted that porous MXene-based paper electrodes with large volumetric capacities and reliable cycling performance are promising for sodium-based energy storage systems when the size is considerable [37]. p-$Ti_3C_2T_x$/CNT electrodes demonstrated significantly superior Li-ion storage performance than non-porous $Ti_3C_2T_x$/CNT films [38]. $Ti_3C_2T_x$, the first MXene to be identified, has been the subject of more than 70% of all MXene study. However, how thoroughly this MXene has been investigated, plenty of researchers now simply refer to it as $Ti_3C_2T_x$ when referring to MXene, which can be deceptive because MXenes can have a broad scope of structural variations and chemical formulations. At least 100 stoichiometric MXene compositions and an unlimited number of solid solutions not only provide uncommon combinations of characteristics, but also the opportunity to customize such traits by altering the ratios of the M or X components. Therefore, considering the numerous possible compositions of MXenes, and its encouraging experimental findings in energy

storage and reliable cycling, it is worth to investigate different compositions of MXenes as anode Material of LIBs.

It is noteworthy to emphasize that MXenes have outstanding qualities that make them potential materials for energy storage devices in the future. These properties include excellent electronic conductivity, low working voltage, quick Li+ diffusion, and an immense theoretical Li storage capacity. However, mostly of these characteristics are from theoretical or computational studies. Hence, it is necessary to experimentally study more extensively how these materials would behave in energy storage devices. Here, various experimental studies of MXene materials as anode of LIBs have comprehensively reported and future research trends are also stated.

2.2 Structural Framework of MXene

It has all started since the report of 'Al' extraction from the MAX phase Ti_3AlC_2, in which a 2-D material Ti_3C_2 was formed having Hydroxyl (OH) and/or Fluoride(F) as surface groups [39]. Since then, tremendous numbers of research have been performed with MXene structures and the numbers of articles for MXene are increasing exponentially. The MAX phase has the general formula of $M_{n+1}AX_n$ in which 'M' and 'A' symbolizes transition metals of d-block and elements primarily from p-block, respectively. The 'X' in the formula represents N or C atoms or both [40]. The mother MAX phase typically undergoes etching to eliminate the 'A' layer of atoms and after sonication the MXene structure is obtained. The overall procedure of synthesizing MXene from MAX phase has been expounded upon in another section within this paper.

A MXene structure can consist of multiple layers of the constituent atoms. When the number of layers in a MXene is less than 5, we can call it a few-layer MXene [41]. A single layer of M_2X MXene structure has M-X-M layers of atoms that means the X atom layer is positioned between two M atom layers. These layers of M and X atoms will create M_6X octahedrons as seen in Fig. 2.1. In addition, the structure is

hexagonal shaped having an ABABAB stacking sequence. These AB type stacking can be observed for $Ti_3C_2T_x$ [42], $Ti_3C_2Cl_x$ [35] where the terminations contributes to form octahedrons. It is noted that, for AB stacking, triangular prisms can be obtained between the layers rather than octahedrons. Etching the MAX phase with HF, some $Ti_3C_2T_x$ structure can have the type of stacking sequence MENDELEY CITATION PLACEHOLDER 42. However, studies exhibited that there can be a mixing of these two types of stacking sequences as well [43]. Furthermore, M_3X_2 and M_4X_3 structures sometimes prefer to have an ABCABC stacking sequence [44].

A surface of MXene layers will have functional groups referred to as surface [45]terminating groups. Mixed terminating groups such as -OH, -Cl, =O, -F can be generally seen to cover the surfaces of MXenes [46]. These functional groups are the result of the etching process done to synthesize MXene structures. Experimentally, these terminating groups can randomly be distributed over the surface of MXene. For instance, the as prepared sample of $Ti_3C_2T_x$ has the highest -F terminating group on its surface whereas the fraction of –O terminations is around 0.3. However, aging of the sample may double the fraction of –O terminating groups in expense of -F terminating groups [47].

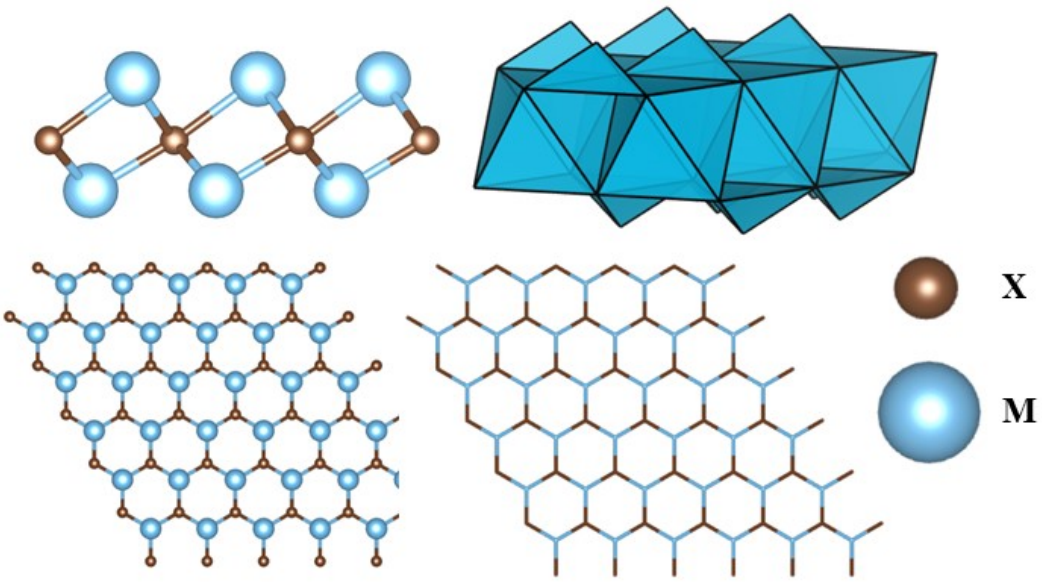

Figure 2.1 A typical M_2X MXene structure without termination.

It is noted that -O and/or -OH termination groups are the most stable ones since -F termination group can easily be substitute with -OH groups while storing in water [48]. MXenes terminated fully with oxygen is thermodynamically more stable than partially terminated structures [49]. However, -OH groups can be transformed to -O groups when the sample is treated with high temperatures [48]. Which sites the terminating groups are attached is another important factor for considering stability. For instance, structures of $Ti_2C(OH)_2$ and $Ti_3C_2(OH)_2$ is more stable when the -OH groups holds the position of hollow sites having three carbon atoms as neighbors [50]. Sometimes inserting a transition element into the MXene structure can prevent to form the unstable M-X bond. In this way the Mo-C bonds in $Mo_3C_2T_x$ and $Mo_4C_3T_x$ is suppressed by adding Ti into the structure makes it more stable [51,52].

However, modification of these functional groups is important to explore remarkable properties of MXenes [36,53]. The O/OH terminating groups can aid the transportation of charges [54]. Methoxy terminated MXenes can be used for esterification process as catalysts [55]. Transmittance can become high when a structure has -F or -OH terminating groups [56]. In addition, the weak bonds between the MX layers can lead to intercalation and thereby expanding the MXene structure's layer spacing (along c axis) [57]. Intercalation with different metallic ions promotes usage of MXene into metal-ion energy storage systems [58]. Capacitors with superior capacitance can be constructed using these cation intercalated MXenes, the properties of which are equivalent to activated graphene [7] . However, K^+ ion intercalation reported a tremendous increase in capacitance with a value of 517 Fg^{-1} in $Ti_3C_2T_x$ after removing the terminating groups with calcination [59]. Furthermore, not only cations, but also organic molecules can be intercalated into MXenes. For instance, a previous report showed the improvement in the lattice index of Ti_3C_2 by the intercalation of dimethyl-sulfoxide (DMSO), organic hydrazine and urea independently [57]. A elevated volumetric capacitance of 1873 F cm^{-3} was found when Ti_3C_2 MXene is intercalated with organic N,N dimethylacetamide [60].

2.3 Synthesis of MXene

MAX is a bulk crystal used in the synthesis of MXenes which is itself two dimensional inorganic substances. It is noted that 2D layered materials produced from the MAX or non-MAX phase would exist before discovery. Unlike most 2D ceramics, MXenes, which are molecular sheets made from the carbides and nitrides of transition metals such as titanium, have exceptional conductivity and great volumetric capacitance by nature. However, more than 100 MXene compounds have been reported and several others have undergone computational investigations from the discovery of first MXene ($Ti_3C_2T_x$). In addition, MXenes may potentially consist of millions of different combinations of carbon, nitrogen, and transition metals such as molybdenum or titanium. It is noted that MXenes are produced by selectively eliminating aluminum from stacked MAX phases. The carbide layers are exfoliated into two sheets of MXene that are only a couple of atoms thick. MXenes can accommodate other ions and molecules between their layers by a procedure called intercalation, which is occasionally required to make use of the material's special features. Inserting lithium ions between the sheets of MXene could transform them into effective materials for LIBs and capacitors. HF etchant, which was first hazardous, has been supplanted with safer electrochemical etching as etching techniques have evolved over time [61]. In this case, using different etchants frequently leads to variations in surface terminations, which could further modify the chemical, electrical, and structural characteristics that are closely linked to energy storage devices' functionality. The three most common etching techniques are discussed briefly in this study.

2.3.1 Wet Chemical Etching

Ti_3AlC_2 MAX ceramic served as the precursor for the first MXene, $Ti_3C_2T_X$, which was produced using HF solution as an etchant as shown in Fig. 2.2.

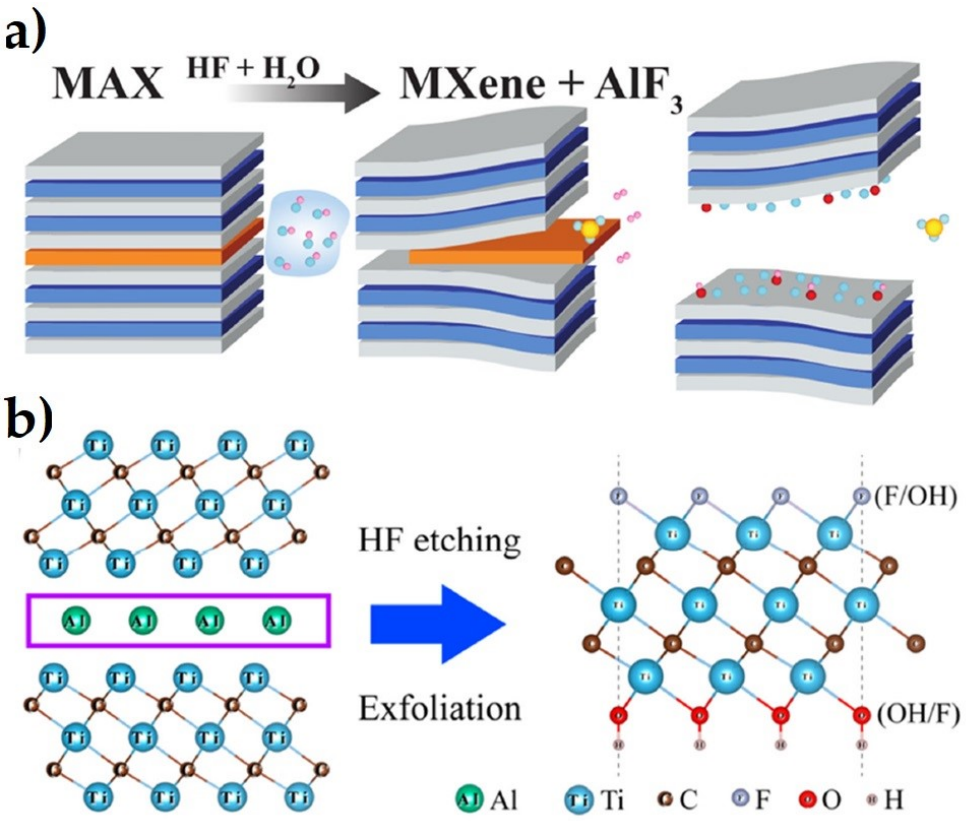

Figure 2.2 (a) Schematic diagram of the synthesis of MXene by HF etching (Adapted from [62,63]) and (b) The synthesis and structure diagram of $Ti_3C_2T_*$ MXene (Adapted from [64])

Nb_2CT_X, Ti_3CNT_X, and V_2CT_X were among the other numerous MXenes that were produced using this method. The suggested etching procedure and related mechanism for Al-based MAX might be written as the following equations [65]:

$$M_{n+1}AlX_n + 3HF \rightarrow M_{n+1}X_n + AlF_3 + 1.5H_2 \quad (2.1)$$

$$M_{n+1}X_n + 2H_2O \rightarrow M_{n+1}X_n(OH)_2 + H_2 \quad (2.2)$$

$$M_{n+1}Xn + 2HF \rightarrow M_{n+1}X_nF_2 + H_2 \quad (2.3)$$

The considerably fragile metallic M-A bonds than M-X (covalent or ionic bonds) broke first, as illustrated in Equation (1), and F ions subsequently joined with the Al ions to create AlF_3, with the generation and release of H_2 [66]. The Al layer was gradually removed from MAX, and the hexagonal lattice was transferred to MXene. Due to its high activity at this point and inability to be stable in either water or acid, MXene would spontaneously react with H_2O and HF, limiting surface energy by producing -F, =O, and -OH surface terminations.

2.3.2 Molten Salt Etching

In the past few years, molten salts etching have expanded into a novel technique that is primarily targeting nitride MXenes as shown in Fig. 2.3(a). Ti_4AlN_3 MAX was first combined with the etchant (a combination of NaF, KF, and LiF), sintered at 550°C for 30 minutes with flowing Ar, and then the reaction byproducts were eliminated using a 4 M H_2SO_4 solution for 1 hour [67]. However, the resulting few-layered $Ti_4N_3T_X$ MXene had more surface flaws than its HF-etched competitors in terms of crystallinity. This process is far more complex than the wet chemistry. However, it is occasionally necessary due to the high temperature, complex fluoride salts, inert environment, and poisonous acid solution that are needed.

A comprehensive approach was suggested to create MXenes with halides at the end using Zn-based MAX as precursors and merely $ZnCl_2$ salts as the etchant [35]. After being heated at 550°C for 5 h in an environment containing solely Ar atmosphere, a group of MXenes, including $Ti_3C_2Cl_2$ and Ti_2CCl_2, were created for the first time. The following equations illustrate the associated process that was elucidated in the replacement reaction between MAX ceramics and the late-transition metal halides [65]:

$$Ti_3ZnC_2 + ZnCl_2 \rightarrow Ti_3C_2Cl_2 + 2Zn^{2+} \quad (2.4)$$

$$Ti_3ZnC_2 + Zn^{2+} \rightarrow Ti_3C_2 + 2Zn^{2+} \quad (2.5)$$

$$Ti_3C_2 + 2Cl^- \rightarrow Ti_3C_2Cl_2 + 2e^- \quad (2.6)$$

$$2Zn^{2+} + 2e^- = 2Zn \quad (2.7)$$

It is noted that despite the significant advancement, the aforementioned inherent limitation is likely to render the molten salts etching approach less practical than the wet chemical etching for the time being.

2.3.3 Electrochemical Etching

In order to etch the Ti_3AlC_2 MAX and produce the $Ti_3C_2T_x$ MXene with - OH and =O terminations, Feng et al. [68] used a binary electrolyte, which is 1 M NH_4Cl + 0.2 M TMAOH. Studies had demonstrated a clear relationship between the concentration of hydroxide and the etching duration and type of product (amorphous carbon or MXene). Approximately 10 h was needed when the value was 0.2 since the reaction efficiency was great. In addition, calculations using the density-functional theory showed that the etching process took place when Ti_3AlC_2 served as the anode and was positively charged. The following conclusions on hypothetical equations were made in light of the experimental findings [65]:

$$Ti_3AlC_2 + 3e^- + 3Cl^- = Ti_3C_2 + AlCl_3 \quad (2.8)$$

$$Ti_3C_2 + 2OH^- - 2e^- \rightarrow Ti_3C_2(OH)_2 \quad (2.9)$$

$$Ti_3C_2 + 2H_2O \rightarrow Ti_3C_2(OH)_2 + H_2 \quad (2.10)$$

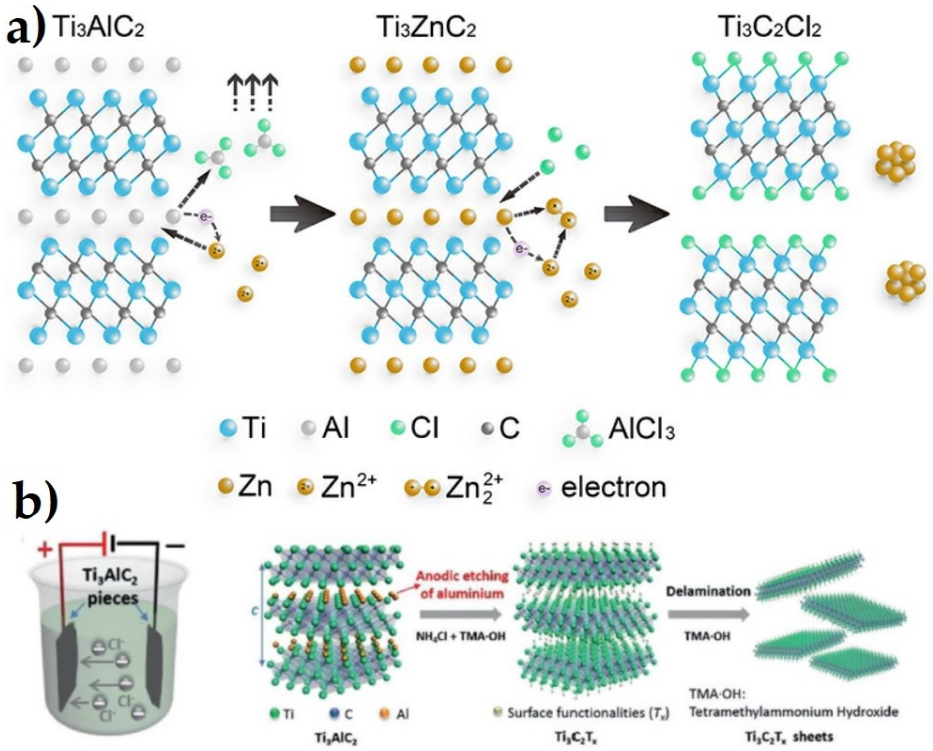

Figure 2.3 Schematic of the etching and delamination process (Adapted from [35]) (a) Molten salts etching. (b)Electrochemical etching (Adapted from [68]).

2.4 MXenes in LIBs

It is necessary to transform and store the energy harvested from nature such as derived from solar and wind sources into electrochemical energy [69]. The most extensively studied electrochemical energy storage technologies are batteries and super capacitors. To address the growing need for both consumer electronics and electric transportation systems, enormous research efforts are being focused on developing new-generation battery-based electrochemical energy storage technologies [70]. However, its affordable price, high stability, and remarkable electronic conductivity, graphite is the most frequently utilized anode material for LIBs, which are the primary power source in small portable devices, electric automobiles, and hybrid electric automobiles. However, the specific capacity of the graphite anode is limited to 372 $mAhg^{-1}$ caused by the lithium-ion intercalation process [71]. A great deal of nanostructures as well as composites, based on carbon materials, transition metal oxides/hydroxides, and conducting polymers, have been studied with a focus on three key parameters: conductivity, surface area and pore structure to enhance the electrochemical performance of battery electrodes [72,73]. Limited specific capacitance, low electrical conductivity, structural deterioration, slowly occurring redox reactions, and restricted ion/electron transport are still among of these materials' primary disadvantages.

MXenes have a wide interlayer spacing, great thermal stability, fast ion and molecule diffusion, an easily adjustable structure, a hydrophilic nature, a high surface area, and large interlayer spacing unlike the other 2D materials [74]. MXene monolayers are anticipated to be metallic because of their enhanced electron density at the Fermi level (E_F). The anticipated greater $N(E_F)$ for MXenes has not been demonstrated to result in higher resistivities than the comparable MAX phases in experiments. The energy locations of the O 2p (~6 eV) and F 2p (~9 eV) bands from the Fermi level of Ti_2CT_x and $Ti_3C_2T_x$ are both affected by adsorption sites and bond lengths to the termination species [75]. Because of their superior capability for adsorption and

reversible intercalation of several metal cations, including Li+ ions at the edges and interlayer gaps of MXenes, 2D MXene materials reflect the features of metal-like conductivity and hydrophilic behavior. In addition, MXenes are outstanding applicants for energy conversion and storage medium due to their outstanding qualities, which include superior electrical conductivity, faster ion and molecule diffusion, low working voltage, and a substantial theoretical storage capacity. These parameters keen attention of researchers to investigate the performance of several MXene materials as anode of LIBs as shown in Fig. 2.4.

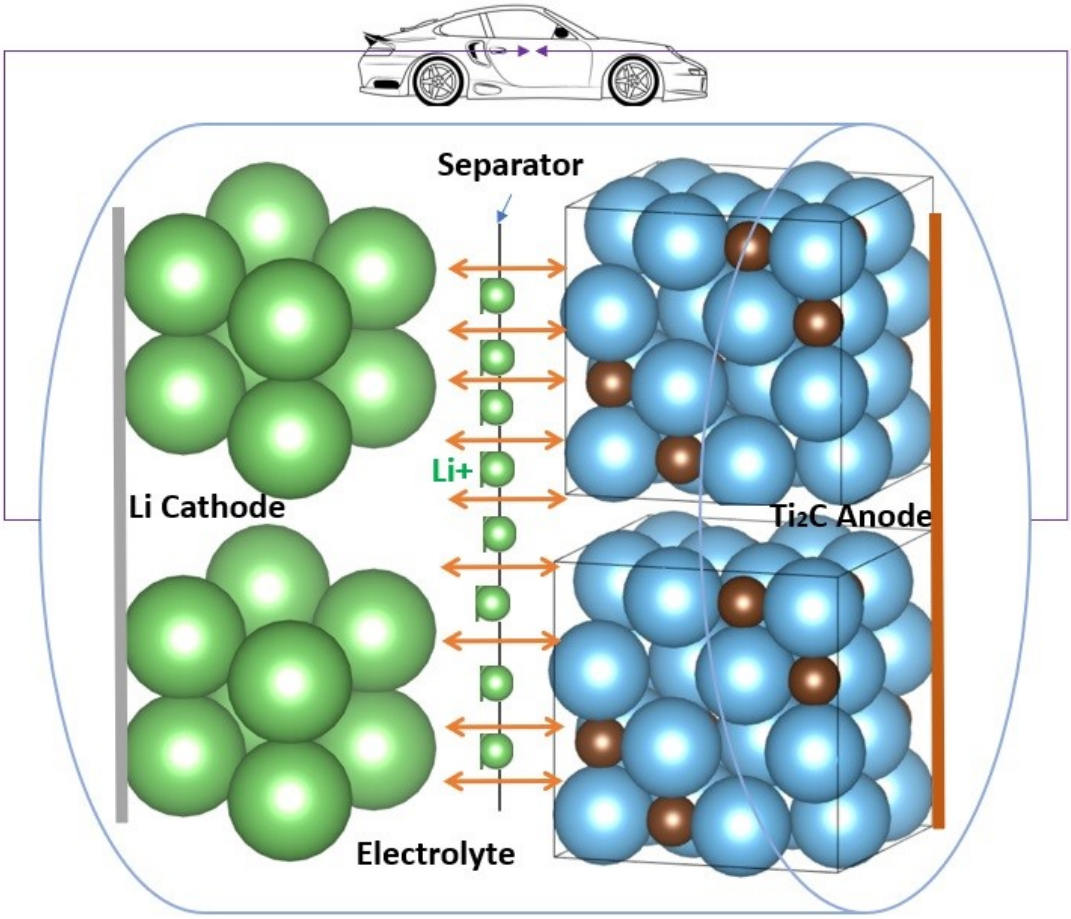

Figure 2.4 Schematic representation of MXene as anode of LIB.

2.4.1 Mono Transition Metal MXene as Anode of LIBs

Mono transition metal MXene is one in which the M layer in $M_{n+1}X_nT_x$ formula composed of only single type of transition metal (i.e. Ti, V, Sc, Zr, Nb, Mo, etc.) such as Ti_3C_2, V_2C, Ti_2C, Mo_2CT_x etc. These types of MXene materials possessed superior

ionic and electric conductivity, larger specific surface area, and excellent cation intercalation ability and demonstrated outstanding potential as anode of LIB. Naguib et al. [23] Prepared 2 D layered exfoliated Ti_2C MXene which was created by etching of Al from Ti_2AlC. In comparison to untreated Ti_2AlC, the newly produced Ti_2C showed a significant (~10-fold) increase in surface area as shown in Fig. 2.5. In addition, it exhibited a specific capacity of 225 $mAhg^{-1}$, which was significantly greater (almost 5 times) than that of the Ti_2AlC precursor. After 120 cycles at a 3C rate and 200 cycles at a 10C rate, consistent cycling capacities of 80 $mAhg^{-1}$ and 70 $mAhg^{-1}$ were respectively observed. The greater surface area, an open structure, and weaker bonding between MX layers in the Ti_2C structure were thought to be the causes of the rise in specific capacity. Additionally, the Li^+ ions can be accommodated in the interlayer voids between the exfoliated Ti_2C sheets.

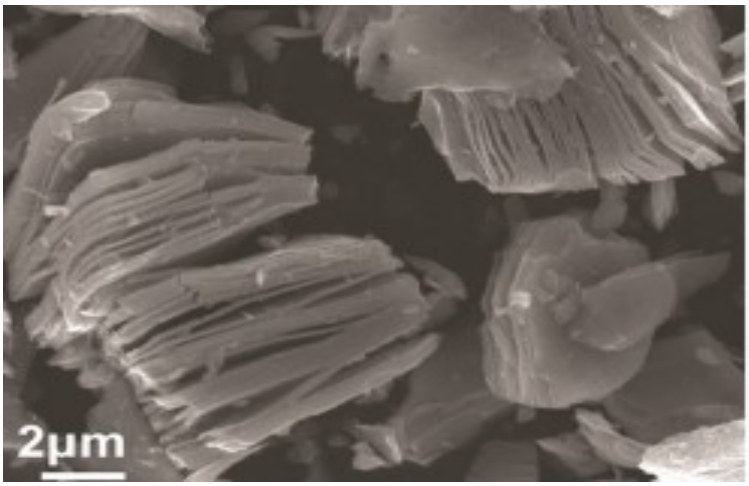

Figure 2.5 SEM image of Ti_2C MXene [23].

Sun et al. [76] reported Ti_3C_2 MXene by the exfoliation of Ti_3AlC_2 with 49% HF solution at a temperature of 60^0C for 24 h, afterward intercalated the exfoliated powder with dimethyl sulfoxide as shown in Fig. 2.6. An increase in lamellar thickness from 30 nm to 100 nm was observed due to the intercalation of exfoliated powder. Owing to the large d-spacing, the intercalated Ti_3C_2 MXene showed superior discharge capacity of 264.5 and 118.7 $mAhg^{-1}$ in the first and 75^{Th} cycle respectively compared to the capacities of 107.2 $mAhg^{-1}$ and 89.7 $mAhg^{-1}$ for

exfoliated Ti_3C_2 at a rate of 1C . The distinction in the performance between ex-Ti_3C_2 and In-Ti_3C_2 was due to the enlarged d-spacing for Li^+ storage resulted from intercalation of exfoliated Ti_3C_2 by DMSO. However, etching with HF resulted in the -F terminal groups on the surface which had a negative impact on conductivity and reduced the materials potential for energy storage and conversion.

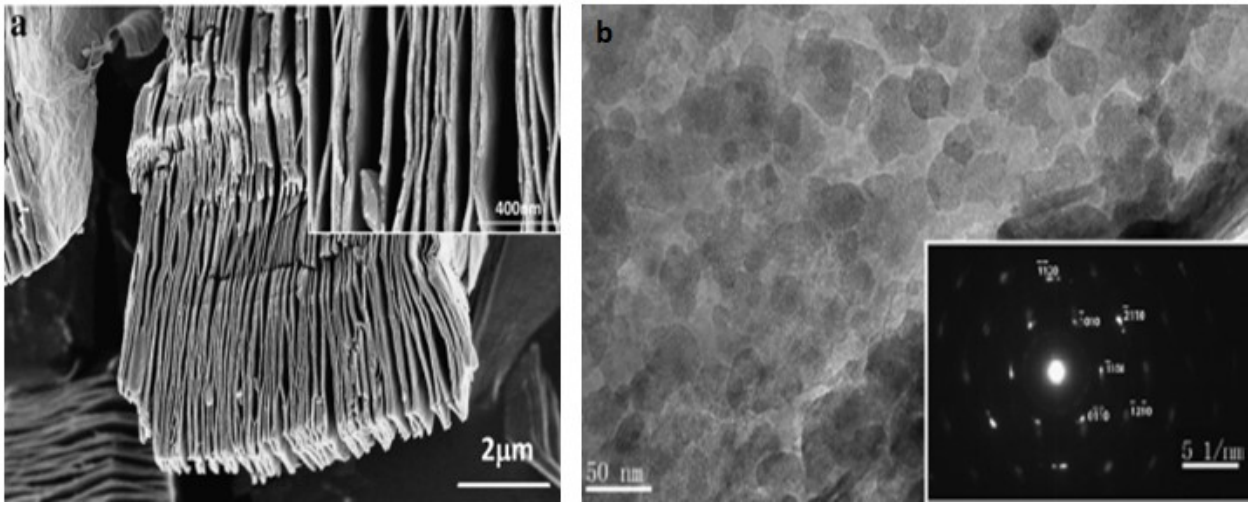

Figure 2.6 a) SEM and b) TEM image of Ti_3C_2 MXene [76].

Zhang et al. [77] synthesized the $Ti_3C_2T_x$ MXene by using HCl +LiF etchant, instead of HF solution. Etching and intercalation process were accomplished in a single step and a defect free and flexible $Ti_3C_2T_x$ MXene paper was obtained by HCl+LiF compared to HF etchant. As prepared Ti_3C_2 MXene was further delaminated by alcohol and the delaminated MXene exhibited excellent cycling performance with specific capacities of 226.3, 137.9, and 102 $mAhg^{-1}$, corresponding to the current densities of 100, 300 and 1000 mAg^{-1}, respectively, after 100 cycles.

A fluorine free $Ti_3C_2T_x$ MXene was synthesized by alkali treatment (NaOH) in which the surface was dominated with O and OH terminal groups [78]. As prepared fluorine free $Ti_3C_2T_x$ delivered higher capacity and superior performance in comparison to fluorine containing $Ti_3C_2T_x$ etched using HF. At a current density of 0.5 Ag^{-1}, the alkali etched $Ti_3C_2T_x$ (mass loading: 1.24 mg cm^{-2}) exhibited a capacity of 106.6 $mAhg^{-1}$ after 250 cycles which was approximately double the capacity of

hydrofluoric acid-etched $Ti_3C_2T_x$ (mass loading: 1.06 mg cm^{-2}) due to its bigger c-lattice parameter and functional groups without fluorine termination. Chen et al. [79] synthesized partially etched Ti_3C_2 MXene as anode of LIB. The precursor Ti_3AlC_2 was etched for 5 min, 0.5 h, 1h, 2h, 4h and 20 h by using 40wt% HF. Reported performance showed that, among all the samples, the MXene obtained after 0.5 h etching (denoted as 0.5 h-pe $Ti_3C_2T_x$) provided optimized performance than that of others. The 0.5 h-pe $Ti_3C_2T_x$ MXene with 10wt% conductive additives provided excellent volumetric capacity of 331.6 mAhcm^{-3} and a superior reversible capacity of 160 $mAhg^{-1}$ after 100 cycles at 1C. In addition, 99% capacity retention was reported after 1000 cycles at same current density. The distinction of performance among the samples may be attributed to the inception of Li-Al alloy between the planes of Ti_3C_2 which was contributed at least in part to raise the capacity of 0.5 h-pe $Ti_3C_2T_x$ MXene.

Zhao et al. [80] fabricated 3D porous $Ti_3C_2T_x$ MXene foam via sulfur template method. As developed porous MXene foam provided massive additional sites for Li^+ storage as well as channels for electron and ion transfer as shown in Fig. 2.7. This porous MXene provided an initial capacity of 455.5 $mAhg^{-1}$, with an initial coulombic efficiency of 65.5% and a capacity of 314.9 $mAhg^{-1}$ after 300 cycles, at 50 mAg^{-1}. Moreover, at various current densities of 1, 2, 10 and 15 Ag^{-1} the supplied capacities were 215.6, 187.4, 133.3 and 112.5 $mAhg^{-1}$, respectively.

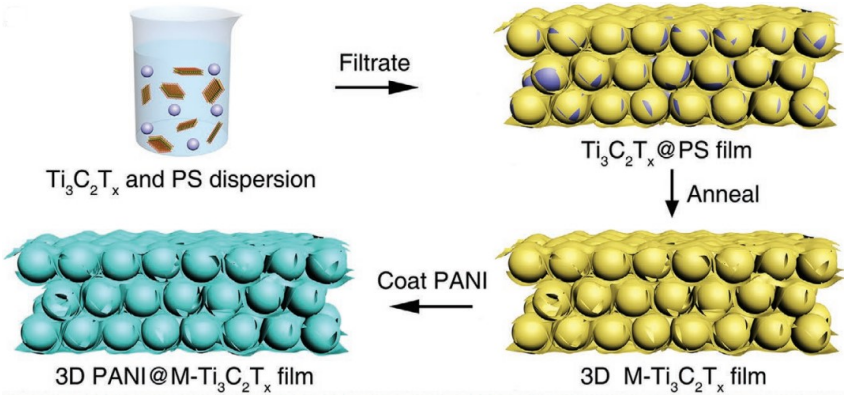

Figure 2.7 Schematic of 3D macroporous PANI@M-Ti3C2Tx frame-works using PS spheres as templates (Adapted from [81]).

Kong et al. [82] reported the electrochemical performance of $Ti_3C_2T_x$ MXene obtained by vacuum calcination at various temperatures of 400, 700 and 1000^0 C. The observed initial coulombic efficiencies of these MXene were 57 and 62% for $Ti_3C_2T_x$-400, $Ti_3C_2T_x$-700 respectively, which was much higher compared to 45% of Ti_3C_2 MXene. The enhancement in performance after calcination may be attributed to the change of the surface chemistry and formation of anatyse TiO_2 on the MXene surface. Moreover, after 100 cycles, at 1 C, the supplied capacities of $Ti_3C_2T_x$, $Ti_3C_2T_x$-400, $Ti_3C_2T_x$-700 and $Ti_3C_2T_x$-1000 electrode were 87.4, 126.4, 147.4 and 79.5 $mAhg^{-1}$, respectively. The lower capacity of $Ti_3C_2T_x$-1000 electrode was thought to be resulted from structural compactness which limited the number of ions that could intercalate.

Meng et al. [83] synthesized scrolled type Ti_3C_2 MXene by cold quenching in liquid nitrogen and compared the performance of Ti_3C_2 scroll with Ti_3C_2 sheet as anode of LIB for different current densities from 100 to 5000 mAg^{-1}. The scroll type MXene exhibited excellent reversible capacities of 226 $mAhg^{-1}$ (1^{st} cycle), 155 $mAhg^{-1}$ (22^{th} cycle), 136 $mAhg^{-1}$ (32^{th} cycle), 113 $mAhg^{-1}$ (42^{th} cycle) and 89 $mAhg^{-1}$ (62cycle) whereas, Ti_3C_2 MXene sheets achieved lower reversible capacities of 199 (1^{st} cycle), 96 (22^{th} cycle), 68 (32^{th} cycle), 51 (42^{th} cycle), 30 $mAhg^{-1}$ (62^{th} cycle) corresponding to the current densities of 100, 500, 1000, 2000 and 5000 mAg^{-1} respectively. The enhance electrochemical performance was reported due to more contact of electrolyte, greater inter layer spacing and shorter diffusion path for Li^+ in the scroll structure. Furthermore, the $Ti_3C_2T_x$ scrolls showed outstanding long-term cycling performance by retaining 81.6% of its initial capacity which was much better than the capacity retention of 63.3% of $Ti_3C_2T_x$ sheets after 500 cycles at 400 mAg^{-1}.

Zhang et al. [84] synthesized pillared SnS/$Ti_3C_2T_x$ composites embellished with in situ formed TiO_2 nanoparticles via solvothermal reaction and annealing treatment as shown in Fig. 2.8. The SnS/$Ti_3C_2T_x$ composite exhibited high capacity of discharge 866 $mAhg^{-1}$ at 500 mAg^{-1} current rate with 99% columbic efficiency which was better

compared to those of commercialized SnS and individual Ti_3C_2. The enhance electrochemical performance was credited with the pillar effect of $Ti_3C_2T_x$ MXenes.

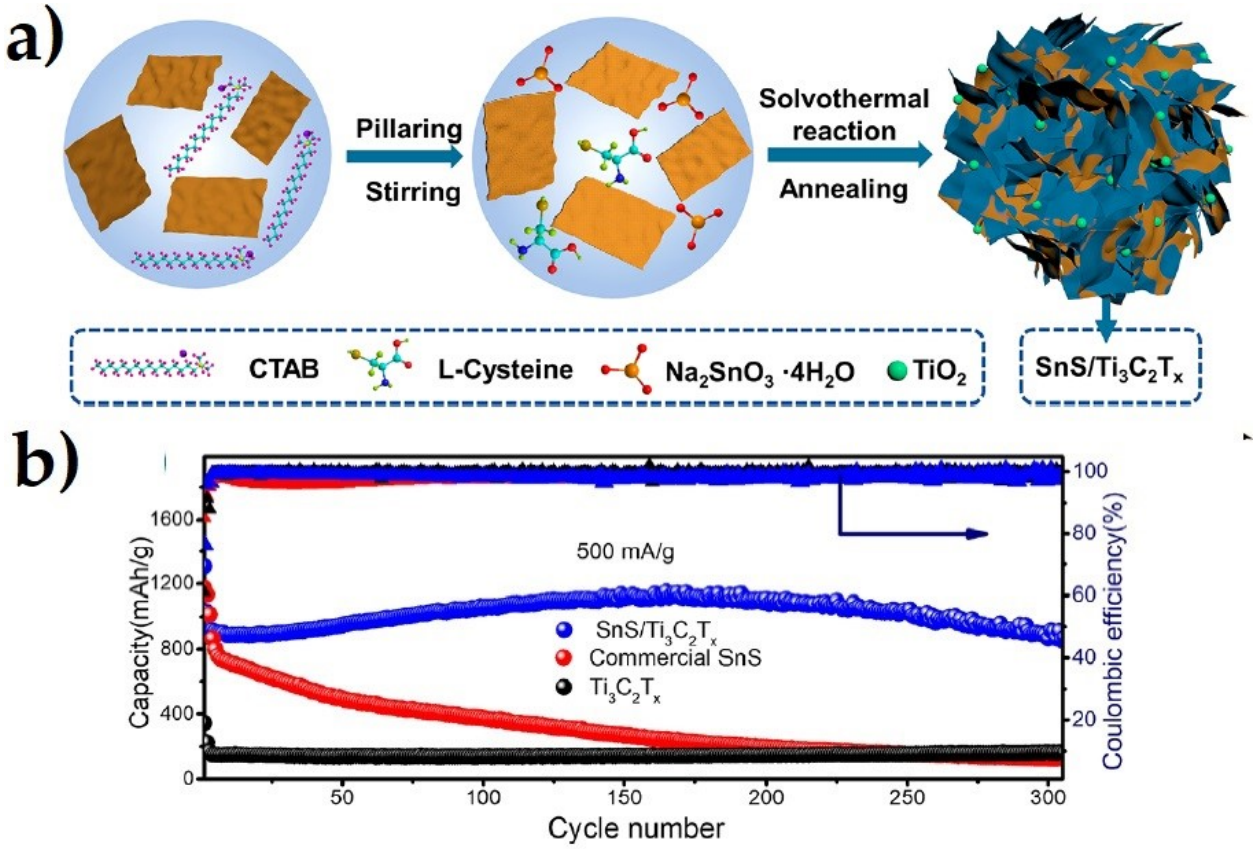

Figure 2.8 (a) Schematic illustration of the preparation process of SnS/Ti3C2Tx MXene and (b) Cycling performance of SnS/Ti3C2Tx , pure Ti3C2Tx and commercial SnS at a current rate of 500 mAg^{-1}. (Adapted from [84])

Recently Dai et al. synthesized self-supported and vertically aligned two dimensional (2D) heterostructures (V-MXene/V_2O_5) of rigid $Ti_3C_2T_X$ MXene and pliable vanadium pentoxide via an ice crystallization-induced strategy as anode of LIBs [85]. This thick V-MXene/V_2O_5 exhibited 472 and 300 mAh g^{-1} at a current rate of 0.2 Ag^{-1}, rate performance with 380 and 222 $mAhg^{-1}$ retained at 5 Ag^{-1}, respectively, after 800 charge/discharge cycles. The enhance electrochemical performances was reported due to the vertical channels facilitated fast electron/ion transport within the entire electrode while the 3D MXene scaffold provided mechanical strength during Li+ insertion/deinsertion. Wang et al. synthesized Fe_3O_4@Ti_3C_2 MXene hybrid via a simple ultrasonication of Ti_3C_2 MXene and Fe_3O_4

nanoparticles and used as anode of LIBs [86]. The one of the compositions of Fe_3O_4@Ti_3C_2 hybrid exhibited high reversible capacities of 747.4 $mAhg^{-1}$ at 1C after 1000 charge/discharge cycles. In addition, this anode material exhibited remarkable volumetric capacity up to 2038 $mAhcm^{-3}$ at 1C due to the high convenient density of the electrode of the prepared hybrid. Tao et al. fabricated mesoporous polydopamine (OMPDA)/$Ti_3C_2T_x$ via in situ polymerization of dopamine on the surface of $Ti3C_2T_x$ via employing the PS-b-PEO block polymer as a soft template as shown in Fig. 2.9. This electrode exhibited average 1000 $mAhg^{-1}$ of discharge capacity with 92 % columbic efficiency at 50 mAg^{-1} current rate after 200 cycles. The enhance electrochemical performance was attributed due the mesopores enhanced the overall capacity and reversibility of the reactions with Li^+ [87].

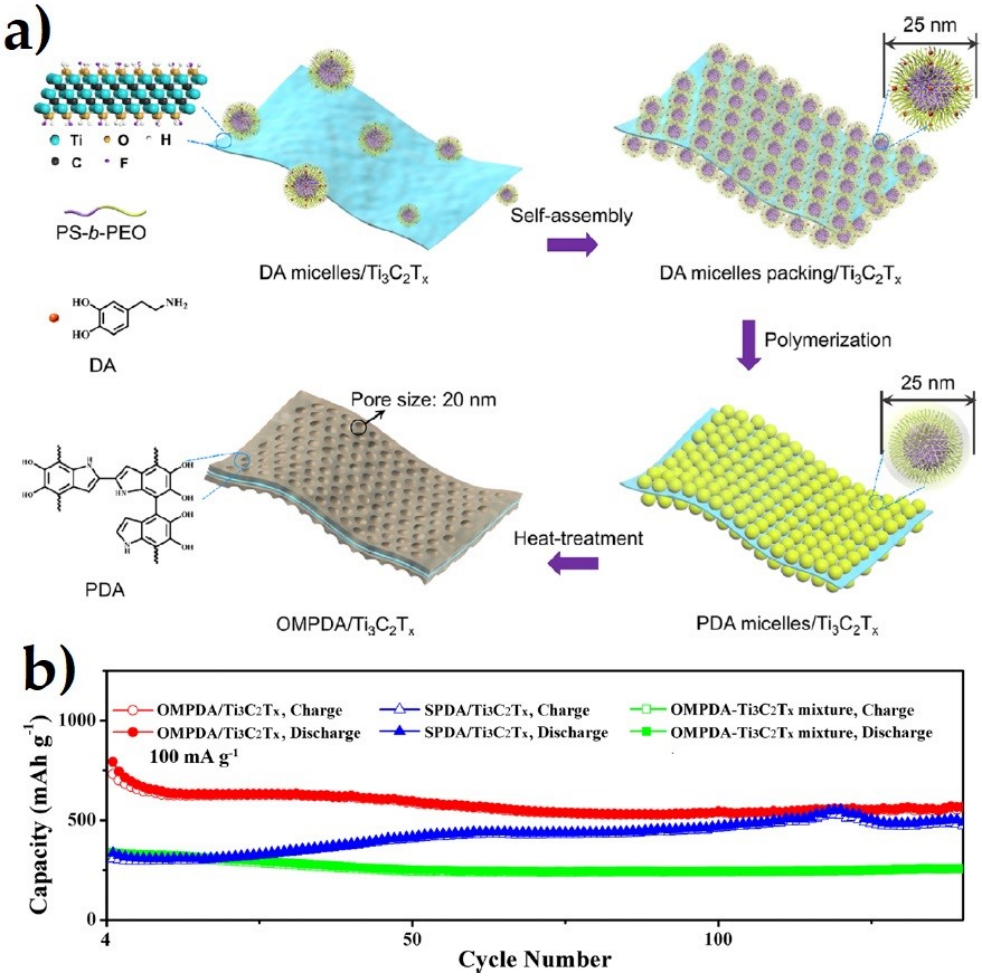

Figure 2.9 (a) Schematic drawing depicting the preparation steps of OMPDA/$Ti_3C_2T_x$ composite and(b) Cycling stability of OMPDA/$Ti_3C_2T_x$ anode.(Adapted from [87]).

Huan et al. [88] reported the Electrostatic Self-assembly of 0D-2D SnO_2 Quantum Dots/$Ti_3C_2T_x$ MXene hybrids as anode for LIBs. This electrode exhibited superior lithium storage properties with high capacity of 887.4 mAh g^{-1} at 50 mA g^{-1} current rate and a stable cycle performance of 659.8 mAh g^{-1} at 100 mA g^{-1} after 100 cycles with a capacity retention of 91%. It is noted that the enhance electrochemical performances was attributed due to the effective routes for rapid transport of electrons and Li^+ by $Ti_3C_2T_x$ MXene. In addition, this MXene materials buffered the volume change of SnO_2 during Li insertion/deinsertion by confining SnO_2 QDs between the nanosheets.

Liu et al. [89] explored the performance of V_2C MXene as anode of LIB. Synthesis process was done by immersing the precursor V_2AlC in a mixture of NaF and HCl for 72h. As prepared MXene delivered an initial discharge and charge capacity of 467 $mAhg^{-1}$ and 291 $mAhg^{-1}$ with a columbic efficiency of 62.3% and retained a reversible capacity of 260 $mAhg^{-1}$ after 20 cycles, at a current density of 370 mAg^{-1}. In addition, at increasing current densities of 50, 100, 200, 500 and 1000 mAg^{-1}, the observed specific capacities for this MXene electrode were 250, 216, 189, 157 and 137 $mAhg^{-1}$, respectively. Zhao et al. [90] came up with 2D Nb_4C_3 MXene which had greater interlayer space for ion accommodation. This MXene as anode of LIB showed outstanding initial discharge and charge capacities of 546 $mAhg^{-1}$ and 333 $mAhg^{-1}$ respectively at a current density of 100 mAg^{-1}. Formation of the SEI layer or the irreversible reduction of the active surface groups such as hydroxyl or fluorine was the reason of the capacity loss in the first cycle. Even after 100 cycles it delivered a reversible capacity of 380 $mAhg^{-1}$ at the same current density. Furthermore, this MXene electrode exhibited excellent rate performances with the capacities of 346, 320, 278, 238, 196, 131, and 88 $mAhg^{-1}$ at the rates of 0.1, 0.2, 0.5, 1, 2, 5 and 10 Ag^{-1} respectively and a discharge capacity of 365 $mAhg^{-1}$ when the current density returned to 0.1 Ag^{-1}.

Zhou et al. [91] reported the effect of ball milling on the electrochemical performance of V_4C_3 MXene as anode of high performance of LIB. The ball milled V_4C_3 MXene supplied superior discharge and charge capacities of 600.8 and 376.2 $mAhg^{-1}$ in the first cycle and a high reversible capacity of 225 $mAhg^{-1}$ after 300 charge/discharge cycles which were much higher in comparison to the capacities of 164.1 and 81.2 $mAhg^{-1}$ in the first cycle and 123.5 $mAhg^{-1}$ after 300 cycles for non-ball milled V_4C_3 MXene, at a current density of 0.1 Ag^{-1}. The distinction in the performance was attributed to the effect of ball milling of MXene powder which ensured enlarged specific surface area and interlayer spacing that not only provided more active space for Li-ion intercalation but also reduced the diffusion barrier for ion and electron transport. Dong et al. [92] synthesized Nb_2CT_x MXene by immersing the Nb_2AlC precursor in lewis acid molten salt at a temperature of 750^0C for 5 h. The surface termination of as prepared Nb_2CT_x MXene dominated with oxygen which was beneficial for Li-ion storage. This type of MXene delivered a maximum lithium storage capacity of 330 $mAhg^{-1}$ at a current density of 50 mAg^{-1}. Moreover, at high rates of 50 C and 100 C the observed capacities for this MXene were 113 and 80 $mAhg^{-1}$ respectively. Fig. 2.10 shows the SEM image of Nb_2C MXene and Nb_2AlC.

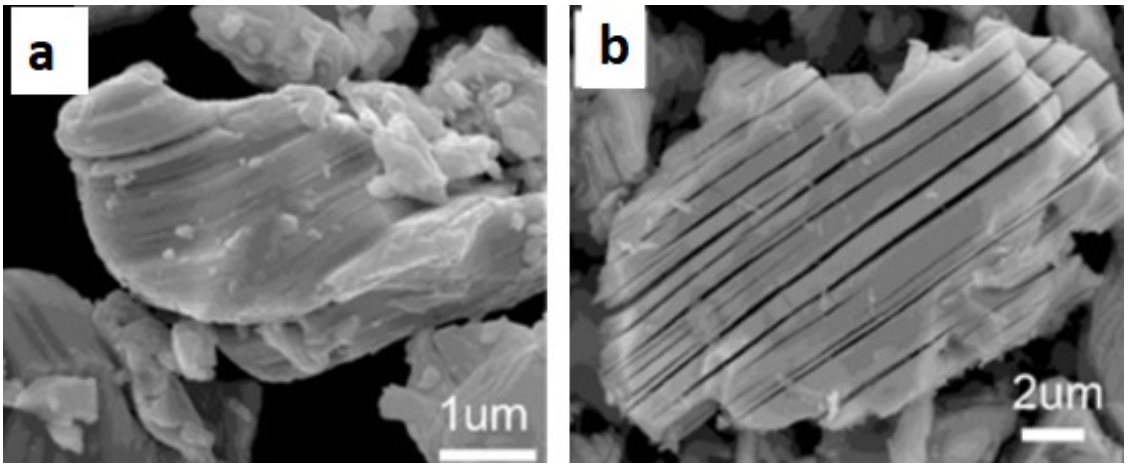

Figure 2.10 (a) SEM of Nb_2AlC and (b) SEM of Nb_2C [92].

A one-step synthesis method was employed for the preparation of a few-layered Nb_2CT_x MXene which exhibited enhanced electrochemical performance compared to

multi-layered Nb_2CT_x MXene as anode of LIB [93]. The few layered Nb_2CT_x MXene electrode showed outstanding discharge and charge capacities of 746 and 524 $mAhg^{-1}$ respectively, corresponding to 70.2% columbic efficiency in the first cycle and a capacity of 485 $mAhg^{-1}$ during the second cycle at a current density of 50 mAg^{-1}. After 100 charge-discharge cycles, this few layered MXene delivered a reversible capacity of 354 $mAhg^{-1}$ which was much higher in comparison to 165 $mAhg^{-1}$ of multilayered Nb_2C MXene, at the same current density. The superior result of few-layered Nb_2C MXene anode could be attributed to the presence of a lower content of F-termination on the surface and having a 2.7 times larger specific surface area compared to multilayered MXene, which offered more active area and active sites for Li-ion storage. Furthermore, the few layered electrode displayed excellent rate performance with specific capacities of 478, 304, 264, and 211 $mAhg^{-1}$ at the current densities of 0.05, 0.25, 0.5, and 1.0 Ag^{-1}, respectively. Luo et al. [94] oxidized the partially etched V_2CT_x MXene in presence of H_2O_2 by using a hydrothermal reaction. As an anode of LIB, the oxidized V_2CT_X MXene delivered a higher specific capacity of 318 $mAhg^{-1}$ after 100 cycles than V_2CT_x MXene, which was 223 $mAhg^{-1}$ at 100 mAg^{-1}. In addition, better rate performance was observed for oxidized V_2CT_x MXene with capacities of 318, 241, and 124 $mAhg^{-1}$ corresponding to the current densities of 50, 200, and 1000 mAg^{-1} respectively. The enhancement in performance after oxidation may be attributed to the change of surface stats (presence of abundant O-terminated groups) and the formation of VO_2 on the interface and surface, which functioned as a bridge to connect Li+ and oxidized V_2CT_x and resulted in more diffusion channels.

Guo et al. [95] employed the hydrothermal method to synthesize Mo_2CT_x MXene by etching Ga from Mo_2Ga_2C precursor. The etching process was carried out with five types of etching solutions of LiF+HCl, NaF+HCl, KF+HCl, NH_4F+HCl and HF. The Mo_2CT_x-K MXene (obtained by etching with KF+HCl) with residual K on the surface delivered higher performance compared to the other cleaned surface samples of

Mo_2CT_x-Li, Mo_2CT_x-Na, Mo_2CT_x-N, and Mo_2CT_x-H as shown in figure 4. At a current density of 50 mAg^{-1}, the Mo_2CT_x-K MXene exhibited superior initial discharge and charge capacity of 1069.6 $mAhg^{-1}$ and 893.6 $mAhg^{-1}$ respectively, with an initial coulombic efficiency of 83.5% and supplied a stable capacity of 151.7 $mAhg^{-1}$ after 100 cycles at a current density of 100 mAg^{-1}. The superior performance of Mo_2CT_x-K MXene compared to the other samples was attributed to the existence of residual K on the surface which bonded with O of Mo_2CT_x and pillared the 2 D sheet. This pillared effect provided enough pathways for Li diffusion and space for Li-ion in 2 D Mo_2CT_x sheet. Further, the Mo_2CT_x-K MXene was delaminated by using tetrabutyl-ammonium hydroxide (TBAOH). The delaminated Mo_2CT_x-K MXene with enlarged interlayer spacing and larger active surface delivered a 7.3 times higher capacity of 239 $mAhg^{-1}$ than 32.7 $mAhg^{-1}$ of Mo_2CT_x-K MXene, at a current density of 800 mAg^{-1} as shown in Fig. 2.11.

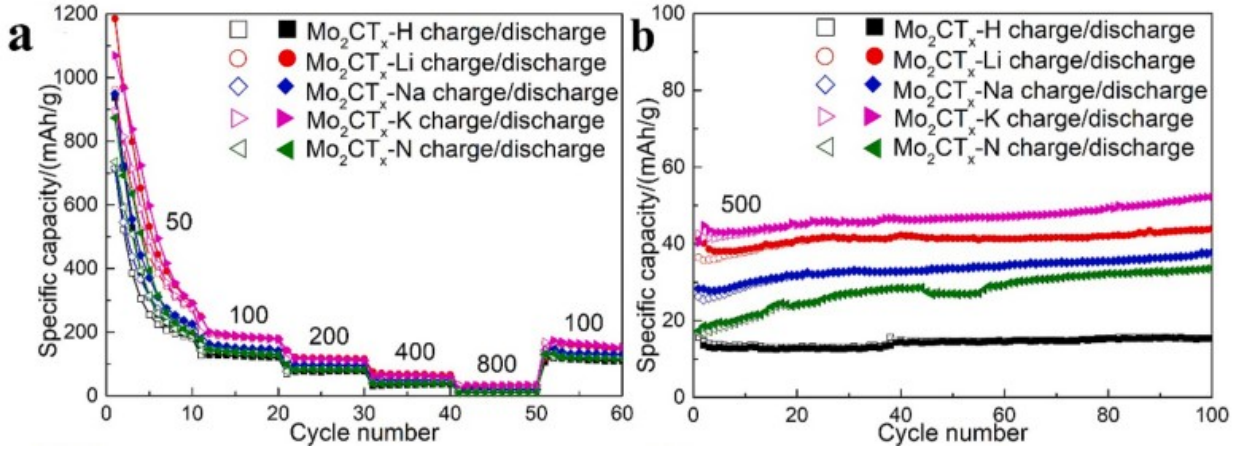

Figure 2.11 (a) Charge-discharge cycle performance curves of different samples at different current densities, (b) Cycle stability curves of different samples at current density of 500 mA/g. [95].

Zhou et al. [96] reported the electrochemical performance of delaminated d-$Hf_3C_2T_x$ MXene as anode of LIB and showed that, the d-$Hf_3C_2T_x$ MXene delivered first discharge capacity of 145 $mAhg^{-1}$, with a coulombic efficiency of 59% and a capacity of 146 $mAhg^{-1}$ after 200 cycles, at a current density of 200 mAg^{-1}. Du et al. [97] Synthesized a freeze dried Ti_3CNT_x MXene as anode of LIB. As prepared Ti_3CNT_x

MXene supplied an excellent initial discharge capacity of ~590 $mAhg^{-1}$ with an initial coulombic efficiency of 42%, and a stable reversible capacity of 343 mAhg-^{1} after 200 cycles, at a current density of 0.05 Ag^{-1}. Moreover, at varied current densities of 0.05, 0.5, 1 and 2 Ag^{-1} the delivered capacities of this MXene were 215, 174, 142 and 107 $mAhg^{-1}$ respectively.

Ti_3C_2 and Nb_2C MXene were fabricated as anode of LIB by cold pressing the MXene powders at a pressure of 1 GPa without use of any binder [98]. As fabricated Ti_3C_2 and Nb_2C MXene maintained a capacitiy of 97 and 128 $mAhg^{-1}$ after 50 cycles, at a current density of 30 mAg^{-1}. Naguib et al. [99] compared the electrochemical performance of Nb_2CT_x and V_2CT_x MXene, obtained via etching of their respective precursor with 50 wt% HF solution. As anode of LIB, The Nb_2CT_x and V_2CT_x MXenes exhibited excellent discharge capacities of 422 and 380 $mAhg^{-1}$ in the first cycle, at 1 C and maintained a reversible capacity of 110 and 125 $mAhg^{-1}$ after 150 cycles, at 10 C. A UV-induced selective etching method was employed to Synthesize fluorine free mesoporous Mo_2C MXene as anode of LIB [100]. As prepared Mo_2C MXene exhibited excellent rate performance with the capacities of 130, 136, 117, 101, 58, 45, 33 and 19 $mAhg^{-1}$ at the current densities of 5, 10, 20, 50, 500, 1000, 2000 and 5000 mAg^{-1} respectively.

To sum up the Mono Transition Metal MXene as Anode of LIBs, Table 2-1 shows the long cycle performance of various 2D mono transition metal MXene as anode of LIB. It shows that, the performance of similar types of MXene is varied with etching solution, etching time and temperature. The reason of this change may be ascribed by the different composition and formation of different terminal groups on the surface of MXene.

Table 2.1 Summery of cyclic performance of mono transition metal MXene as anode of Lithium Ion Batteries.

Anode material	Etchant	Etching time (h)	Discharge capacity ($mAhg^{-1}$) & Current rate (Ag^{-1})	Number of cycle	Ref.
Ti_2C	10 wt% HF at RT	10	70 at 10 C	200	[23]
Ti_3C_2	49 wt% HF at 60^0C	24	118.7 at 1 C	75	[76]
Ti_3C_2	HCl+LiF at 35^0C	24	47.9 at 3 Ag^{-1}	100	[101]
Ti_3C_2	NaOH		104.8 at 0.5 Ag^{-1}	500	[78]
Partially etched Ti_3C_2	40 wt% HF at RT	0.5	160 at 1 C	100	[79]
Porous Ti_3C_2	HCl+LiF at 35^0C	24	220 at 1 Ag^{-1}	3500	[80]
$Ti_3C_2T_x$-400	40 wt% HF at 60^0C	48	126.4 at 1 C	100	[82]
$Ti_3C_2T_x$-700	40 wt% HF at 60^0C	48	147.4 at 1 C	100	[82]
Scroll Ti_3C_2	HCl+LiF at 40^0C	24	~112 at 0.4 Ag^{-1}	500	[83]
V_2C	HCl+NaF at 90^0C	72	243 at 0.5 Ag^{-1}	500	[89]
Nb_4C_3	49 wt% HF at RT	140	320 at 1 Ag^{-1}	750	[90]
V_4C_3	40 wt% HF at 55^0C	96	125 at 1 Ag^{-1}	300	[91]
Nb_2CT_x	Lewis acid at 750^0C	5	150 at 1 Ag^{-1}	500	[92]
Nb_2C	40 wt% HF at	90	225 at 1 Ag^{-1}	800	[93]

Anode material	Etchant	Etching time (h)	Discharge capacity ($mAhg^{-1}$) & Current rate (Ag^{-1})	Number of cycle	Ref.
	60^0C				
partially etched V_2CT_x	40 wt% HF at RT	7 days	125 at 1 Ag^{-1}	1000	[94]
d-Mo_2CT_x	HCl+KF at 180^0C	24	118.8 at 2 Ag^{-1}	100	[95]
d-$Hf_3C_2T_x$	35 wt% HF at RT	60	146 at 0.2 Ag^{-1}	200	[96]
Ti_3CNT_x	HCl+LiF at 30^0C	12	300 at 0.5 Ag^{-1}	1000	[97]
Mo_2C	H_3PO_4	3-5	90 at 0.01 Ag^{-1}	140	[100]

2.4.2 Double Transition Metal MXene (DTM) as anode of LIBs

The double transition metal MXene is comprised of two distinct transition metals denoted as M′ and M′′. Based on the structure, double-transition MXene is divided into two categories as shown in Fig. 2.12. The first one is ordered MXene in which the two transition metals (M′ and M′′) are arranged alternatively in a 2 D structure. This material can be further classified into two groups: i) in plane ordered DTM, denoted by the formula $M'_{4/3}M''_{2/3}XT$ such as $Mo_{4/3}Y_{2/3}CT_x$ and ii) out of plane ordered DTM, which is defined by the formula of $M'_2M''X_2T_x$ or $M'_2M''_2X_3T_x$ such as $Mo_2TiC_2T_x$. The other DTM is solid-solution DTM, which is composed of two individual transition metals distributed randomly in all M layers and is denoted by the formula of $(M',M'')_{n+1}C_nT_x$ such as $(Ti,Nb)_3C_2T_x$. This diverse transition metal arrays and structures of DTM resulted in improved thermoelectric, mechanical and electrochemical properties [44] .

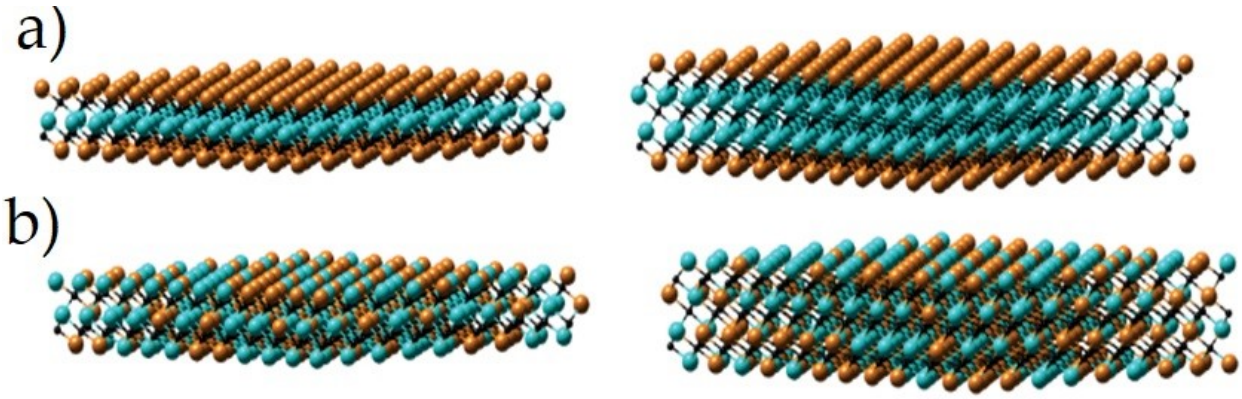

Figure 2.12 Representation of structure of (a) ordered DTM and (b) solid solution of MXene. (Two colors of molecules represent two types of transition metals) (Adapted from [44]).

Cheng et al. [102] synthesized a novel phased $VNbCT_x$ Double transition MXene by selectively etching the Al layer from its VNbAlC MAX phase. As anode of LIB, the $VNbCT_x$ MXene delivered an excellent specific capacity of 520.5 $mAhg^{-1}$, at a current density of 0.1 Ag^{-1}. The capacity was increased gradually with cycle number which may be ascribed by the rapid transfer of ions and electrons in the layered nanosheet of $VNbCT_x$ MXene as in Fig 2.13. A long term cyclic stability (1000 cycles) was also observed by this MXene even though the structure became curled from nanosheet after long cycle which may be attributed to the wrinkled layered structure which provided channels for Li+ transport. In addition, this electrode provided promising rate performance with specific capacities of 409.7, 301.7, 222.5, 133.5, 81.4, and 53.7 $mAhg^{-1}$ corresponding to the current densities of 0.2, 0.5, 1, 2, 5, and 10 Ag^{-1} respectively. This superior performance resulted from the multilayer skeleton of $VNbCT_x$ MXene, which prevented the restacking of sheets and limited the volume expansion during cycling.

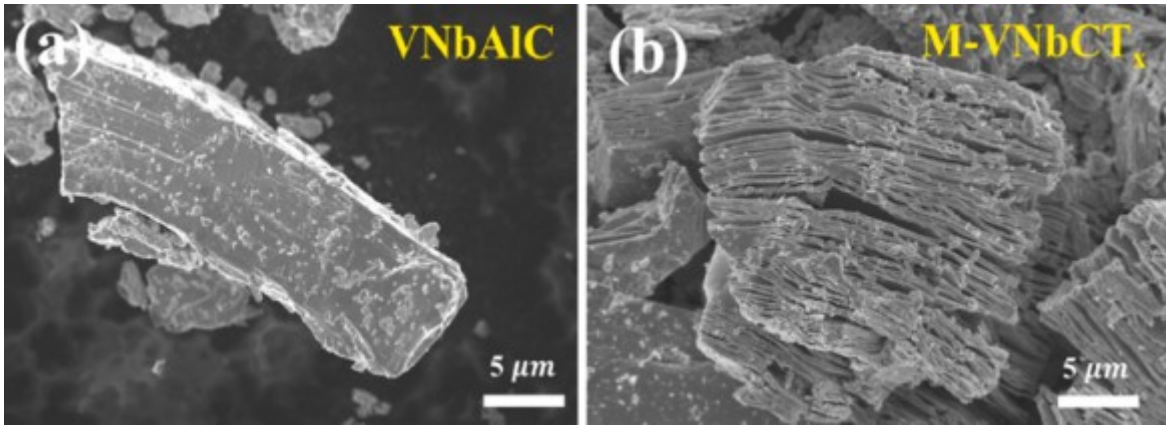

Figure 2.13 (a) SEM image of VNbAlC and (b) SEM image of multi-layer VNbCTx [102].

Liu et al. [103] successfully fabricated highly conductive $Ti_2NbC_2T_x$ double transition metal MXene which delivered higher electrochemical performances in comparison to $Ti_3C_2T_x$ MXene as anode of LIB. At a current density of 0.1 Ag^{-1}, the $Ti_2NbC_2T_x$ electrode supplied a discharge capacity of 305.7 $mAhg^{-1}$, corresponding to an efficiency of 58.65% in the first cycle whereas the delivered capacity of $Ti_3C_2T_x$ MXene was 502.2 $mAhg^{-1}$, with an efficiency of 44.2%. The higher efficiency of $Ti_2NbC_2T_x$ electrode was attributed to the lower charge transfer resistance and higher extraction/insertion rate of Li+. However, after 400 cycles, the displayed capacity of $Ti_2NbC_2T_x$ was 198 $mAhg^{-1}$ which was higher than 135 $mAhg^{-1}$ of $Ti_3C_2T_x$, under the same current density. Even at varied current densities of 0.1, 0.2, 0.5, 1.0, 2.0 and 5.0 Ag^{-1}, the $Ti_2NbC_2T_x$ MXene still showed superior rate performance of 196.2, 156.6, 141.4, 124.8, 113.6, and 90.6 $mAhg^{-1}$ compared to 135.3, 89.8, 57.6, 35.9, 18.8, and 7.8 $mAhg^{-1}$ of $Ti_3C_2T_x$ MXene. Moreover, the $Ti_2NbC_2T_x$ exhibited excellent capacity retention of 81%, after 4000 cycles, under a current density of 1 Ag^{-1}. This improved capacity may be attributed to the incorporation of Nb which enlarged the interplanar spacing as well as provided increased active sites.

A series of $(V_xTi_{1-x})_2C$ (x=0,0.3,0.5,0.7,1) MXene compound were synthesized by etching of $(V_xTi_{1-x})_2AlC$ solid solution for different time periods of 1h, 5h, 24h, 36h and 48h respectively [104]. As anode of LIB, the $(V_{0.5}Ti_{0.5})_2C$-24h MXene delivered an

initial discharge and charge capacity of 445.9 and 286.6 $mAhg^{-1}$ respectively with 64% coulombic efficiency and a capacity of 194.9 $mAhg^{-1}$ after 100 cycles at a current density 1 Ag^{-1}. Formation of SEI on the surface and irreversible reduction were thought to be reason of irreversible capacity in the initial cycles. After 500 cycles, the supplied capacities of Ti_2C-1h, $(V_{0.3}Ti_{0.7})_2C$-5h, $(V_{0.5}Ti_{0.5})_2C$-24h, $(V_{0.7}Ti_{0.3})_2C$-36h and V_2C-48h samples were 128.9, 132.5, 194.9, 155.3 and 115.6 $mAhg^{-1}$ respectively at same current density. The lower capacity of V_2C-48h and Ti_2C-1h was attributed to the restacking of MXene sheet and the superior capacity of $(V_{0.5}Ti_{0.5})_2C$-24h MXene was ascribed to the maximum synergy of Ti and V. Syamsai et al. [105] prepared a layered $Ti_xTa_{(4-x)}C_3$ bi metal MXene as anode of LIB which delivered a discharge capacity of 1411 $mAhg^{-1}$ initially at a rate of 0.05C, and retained a reversible capacity of 476 $mAhg^{-1}$, with a coulombic efficiency of ~99% after 100 cycles at 0.5 C. This outstanding performance was attributed to the formation of stable bi-metallic MXene with expanded interlayer d-spacing of 3.37 Å which allowed storage of Li+ on its surface and layers. It is noted that $(Nb_{0.8},Ti_{0.2})_4C_3T_x$ and $(Nb_{0.8},Zr_{0.2})_4C_3T_x$ MXene synthesized via altering 20% of Nb from $Nb_4C_3T_x$ MXene to improve the Li^+ storage capacity [106]. However, the result was not comparable enough. It is noted that after 20 cycles, the $(Nb_{0.8},Ti_{0.2})_4C_3T_x$ and $(Nb_{0.8},Zr_{0.2})_4C_3T_x$ MXene showed lower capacity of 158 and 132 $mAhg^{-1}$ compared to the capacity of $Nb_4C_3T_x$ MXene, which was 189 $mAhg^{-1}$. Several groups experimentally investigated DTM as anode of LIBs. Their electrochemical performances are summarized in Table 2.2.

Table 2.2 Summery of Cyclic performance of 2D DTM as anoe of LIB.

Anode material	**Etchant**	**Etching time (h)**	**Discharge capacity ($mAhg^{-1}$) & Current rate (Ag^{-1})**	**Number of cycle**	**Ref.**
VNbCTx	50 wt% HF at 40^0C	48	520.5 at 0.1 Ag^{-1}	100	[102]

$Ti_2NbC_2T_x$	48 wt% HF at 50^{0}C	24	95.2 at 1 Ag^{-1}	4000	[107]
$(V_{0.7}Ti_{0.3})_2C$	LiF+HF at 90^{0}C	5	177 at 1 Ag^{-1}	1000	[104]
$(V_{0.5}Ti_{0.5})_2C$	LiF+HF at 90^{0}C	24	204.9 at 1 Ag^{-1}	1000	[104]
$(V_{0.3}Ti_{0.7})_2C$	LiF+HF at 90^{0}C	36	184.9 at 1 Ag^{-1}	1000	[104]
$Ti_xTa_{(4-x)}C_3$	40 wt% HF at RT	72	459 at 0.5 C	200	[105]

2.4.3 Composite MXene as anode of LIBs

The mono and double transition metals MXene have good electrical conductivity and cyclic stability. However, various challenges were observed in achieving high specific capacity, high stability, and effective electron/ion transport since most 2D MXene nanosheets are vulnerable to self-staking, which reduces specific surface area and Li^+ intercalation numbers. For increasing specific surface area and facilitating ion mobility one of the strategy is to expand interlayer gaps which can be accomplished by applying different types of doping and fillers (Si, Sn, Ag, Fe, CNT, and other oxides) on the surface of MXene. Combination of MXene with other dopants and fillers defined as composite MXene such as Ti_3C_2/Si, $SiO_2/Ti_3C_2T_x$, $Fe/Ti_3C_2T_x$, etc.

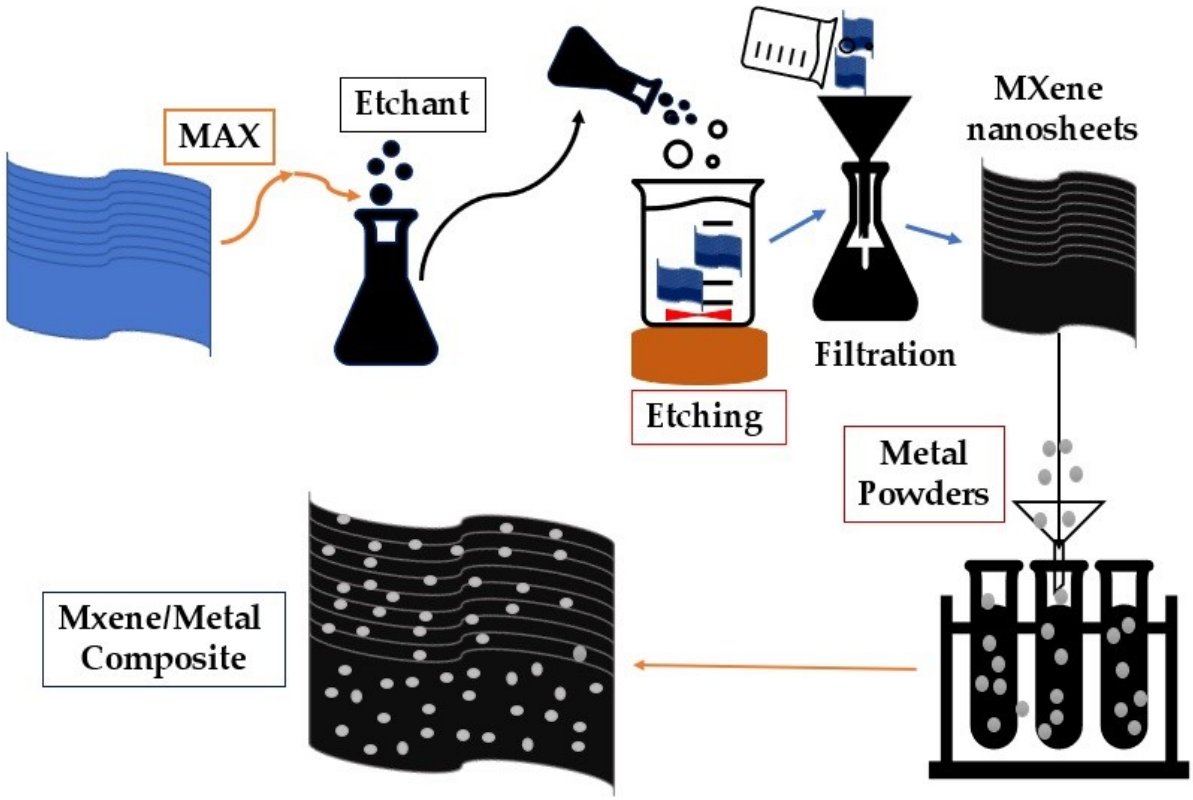

Figure 2.14 Schematic representation of synthesis process of MXene/Metal composite.

Li et al. [108] fabricated nickel hydroxide based delaminated titanium carbide ($Ni(OH)_2$/d-Ti_3C_2) composite MXene as anode of lithium ion battery. The well-wrapped $Ni(OH)_2$ tackled the restacking of d-Ti_3C_2 and enlarged the surface area for Li^+ insertion as well as shortened the Li^+ diffusion distance. As prepared composite MXene exhibited better performance than delaminated Ti_3C_2 and delivered an initial discharge and charge capacity of 615.2 $mAhg^{-1}$ and 578.7 $mAhg^{-1}$ with an efficiency of 94.06% and a reversible capacity of 732.6 $mAhg^{-1}$ after 200 cycles at a current density of 0.1 Ag^{-1}, which was 6 times superior to that of delaminated Ti_3C_2 MXene (121.3 $mAhg^{-1}$) at the same current density.

Zhang et al. [109] prepared the NiCo-LDH/Ti_3C_2 composite MXene via electrostatic interaction force between the surface of negatively charged Ti_3C_2 MXene and positively charged nickel-cobalt ions. The tightly anchored ultra-thin, bent, and wrinkled α-phase crystal of NiCo-LDH and the vertical development of LDH in the

three-dimensional conductive network of NiCo-LDH/Ti_3C_2 MXene as in Fig 2.15 resulted in a gap of 8.1 Å between the interlayers and supplied more active sites that inhibited MXene restacking and accelerated ion diffusion. As a result, the NiCo-LDH/Ti_3C_2 MXene delivered superior intial discharge and charge capacities of 1827.3 and 1266.4 $mAhg^{-1}$ respectively, at a current density of 100 mAg^{-1}. In addition, at varied current densities from 0.1 to10 Ag^{-1} the observed discharge capacities were in the range of 1076.7 to 370.6 $mAhg^{-1}$. Li et al. [110] synthesized the NiFe-LDH/$Ti_3C_2T_x$ MXene via hydrothermal method and analyzed the performance as anode of LIB. As prepared NiFe-LDH/$Ti_3C_2T_x$ MXene delivered superior initial discharge capacity of 1376.4 $mAhg^{-1}$, with an initial coulombic efficiency of 56.6% and exhibited excellent cycling stability with a capacity of 898.8 $mAhg^{-1}$, after 200 cycles, at a current density of 0.1 Ag^{-1}. In addition, this electrode supplied high rate performances with the capacities of 959.5, 651.7, 528.8, 413.8, 315.5 and 270.3 $mAhg^{-1}$ corresponding to the current densities of 0.1, 0.2, 0.5, 1, 1.5 and 2 Ag^{-1} respectively.

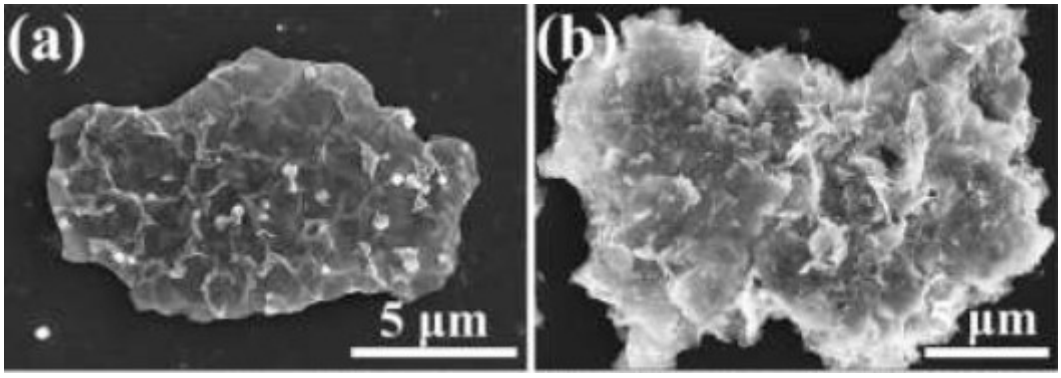

Figure 2.15 (a) SEM images of pristine Ti_3C_2 MXene. (b) SEM image of as-prepared NiCoLDH/Ti_3C_2 Nanosheets [109].

Hui et al. [111] prepared Ti_3C_2/Si composite MXene as anode of lithium ion battery. This Ti_3C_2/Si composite electrode exhibited very high first discharge/charge capacity of 3512.5/2145.1 $mAhg^{-1}$ with an initial efficiency of 61.1%, and an efficiency of 87.8% in the 2nd cycle at a current density of 100 mAg^{-1}. In addition this MXene displayed excellent cycling stability with an improved capacity of 1475 mAhg-1 after 200 cycles at same current density. The excellent performance of this MXene could be

attributed to the uniform dispersion of Si nanoparticles over the surface of Ti_3C_2 MXene sheet which ensured faster Li^+ and electron transportation channels and prevention of volume expansion of Si by Ti_3C_2 during cycling. Zhou et al. [112] fabricated Si nanospheres coated Ti_3C_2Tx composite MXene (denoted as $Si/Ti_3C_2T_x$) as anode of LIB via electrostatic self-assembly method. As assembled MXene exhibited excellent first cycle discharge and charge capacities of 3986.8 and 3025.1 $mAhg^{-1}$ respectively and delivered a reversible capacity of 2442.5 $mAhg^{-1}$, after 100 cycles, at a current density of 0.1 Ag^{-1}. In addition, a much higher reversible capacity of 1917.9 $mAhg^{-1}$ was observed compared to 46.9 $mAhg^{-1}$ of pristine Ti_3C_2 MXene after 300 cycles at a current density of 0.5 Ag^{-1}. The SEM image of Ti_3C_2 and Si/Ti_3C_2 shown in Fig. 2.16.

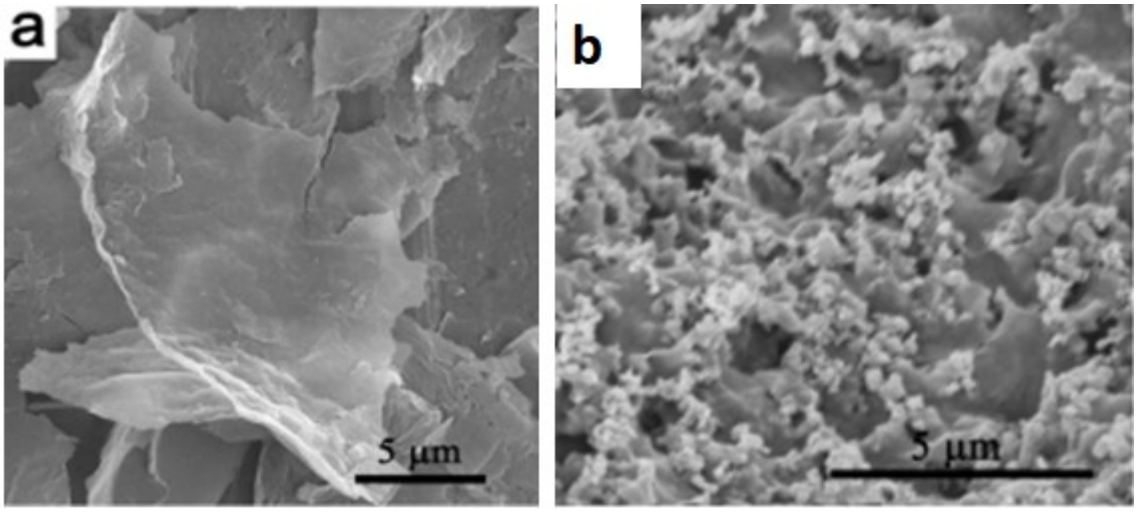

Figure 2.16 (a) SEM image of Ti_3C_2 (b) SEMimage of Si/Ti_3C_2 [112].

Tian et al. [113] revealed the electrochemical performance of flexible and binder free $Si/Ti_3C_2T_x$ composite MXene as anode of LIB. As prepared binder free anode delivered a discharge capacity of ~ 2930 $mAhg^{-1}$, with a coulombic efficiency of 71% in the first cycle and a capacity of 2118 $mAhg^{-1}$ after 100 cycles, at a current density of 200 mAg^{-1}. Moreover, at varied current densities from 1000, 2000, 3000, 4000 to 5000 mAg^{-1} the supplied discharge capacities of this MXene were 1768, 1501, 1294, 1033, and 886 $mAhg^{-1}$ respectively. Zhang et al. [114] prepared flexible porous $Si/Ti_3C_2T_x$ composite MXene by vacuum filtration and fabricated anode of LIB by this

composite MXene with various mass ratios of Si and $Ti_3C_2T_x$ MXene (1:1, 2:1, and 3:1) as shown in Fig. 2.17. Higher mass content of porous Si resulted in enhancement of electrochemical performance. However, the structure of Si/$Ti_3C_2T_x$ -3:1 was more brittle and fragmented during cell assembly, which led to capacity failure after a few cycles. Hence, the Si/$Ti_3C_2T_x$-2:1 composition provided optimum performance among all combinations with initial discharge and charge capacities of 2843.5 and 1778.4 $mAhg^{-1}$ respectively and maintained a reversible capacity of 1039.3 $mAhg^{-1}$ after 200 cycles at a current density of 500 mAg^{-1}. In addition, at current densities of 0.05, 0.5 and 5 A/g the observed capacities of Si/$Ti_3C_2T_x$-2:1 MXene were 2256.5, 1661 and 840.3 $mAhg^{-1}$ respectively, which were much higher than that of porous Si and other ratio of Si/$Ti_3C_2T_x$.

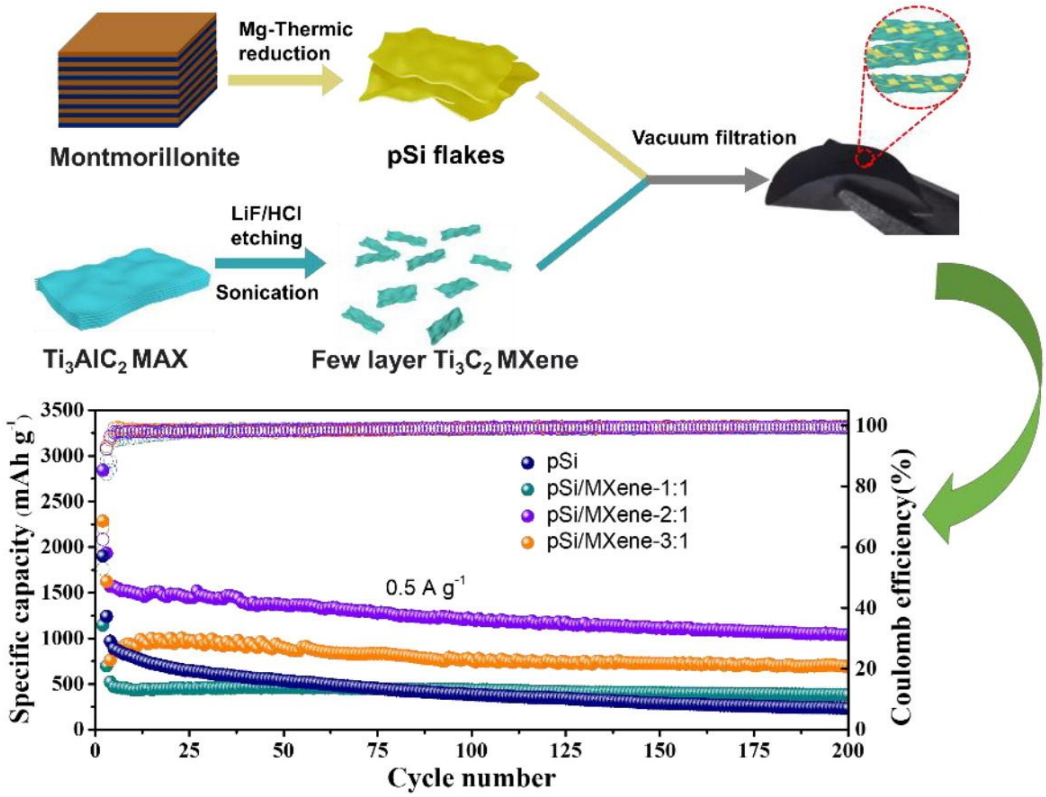

Figure 2.17 Schematic representation of synthesis and cyclic performances of different samples at 0.5 Ag^{-1}. (Adapted from [114])

Bashir et al. [115] embedded silicon nanoparticles on V_2C MXene nanosheet to create Si-V_2C nanocomposite MXene electrode for LIB. This composite electrode exhibited excellent first cycle discharge and charge capacity of 921 and 691 $mAhg^{-1}$

respectively and retained a stable capacity of 430 $mAhg^{-1}$, after 150 cycles, at a current density of 200 mAg^{-1}. In addition, the Si-V_2C electrode displayed high-rate performance with a capacity of 140 $mAhg^{-1}$ corresponding to a current density of 3 Ag^{-1}.

Maughan et al. [116] reported the electrochemical performance of Mo_2TiC_2–Si-400 MXene, obtained via amine assisted silica pillaring and calcination at 400^0 C. Pillaring method created porous Mo_2TiC_2 MXene which resulted in larger interlayer spacing up to 4.2 nm. As a result, The Mo_2TiC_2–Si-400 MXene delivered an initial discharge and charge capacities of 473 and 314 $mAhg^{-1}$, with an initial coulombic efficiency of 66% and an efficiency of 94% in the second cycle at a current density of 20 mAg^{-1}. Moreover, at the current densities of 20, 50, 200, 500, and 1000 mAg^{-1} the observed discharge capacities of this MXene were 312, 281, 229, 182 and 143 $mAhg^{-1}$, respectively. Mu et al. [117] synthesized microsphere like hybrid $SiO_2/Ti_3C_2T_x$ MXene and revealed its performance as anode of LIB at different current densities. At a current density of 200 mAg^{-1}, the delivered charge/discharge capacity of this electrode during first cycle was 820 and 1173 $mAhg^{-1}$ respectively and after 100 cycles it maintained a discharge capacity of 798 $mAhg^{-1}$ at the same current density. In addition, excellent rate performance were also observed with the capacities of 840, 739, 683, 553 and 517 $mAhg^{-1}$ at the current densities of 0.1, 0.5, 1, 2 and 3 Ag^{-1} respectively. This exceptional performance might be attributed to the development of a 3D high conductive network and the bond between MXene and SiO_2 nanoparticles which boosted the structural stability and shortened the Li-ion pathway length.

Han et al. [118] designed a self-integrated Si/$Ti_3C_2T_x$ MXene bonded with interfacial nitrogen layer (denoted as Si-N-$Ti_3C_2T_x$) as high performance anode for LIB. The interfacial nitrogen bond boosted adhesion between Si and highly conductive $Ti_3C_2T_x$ MXene which resulted in improved rate performance and cycling stability by facilitating ion and electron transport. As a result, the Si-N-

$Ti_3C_2T_x$ MXene electrode, supplied superior specific capacities of 2228, 2078, 1818, and 1469 $mAhg^{-1}$ corresponding to the current densities of 0.8, 1.6, 3.2, and 6.4 Ag^{-1} respectively and maintained excellent cyclic stability with a specific capacity of 1060 $mAhg^{-1}$, after 500 cycles, at a current density of 1.6 Ag^{-1}.

Zhang et al. [119] produced a SiO_x-coated N-doped $Ti_3C_2T_x$ MXene composite as the anode of LIB by employing melamine-assisted ball milling and annealing processes. The prepared composite MXene delivered excellent discharge and charge capacities were 1882.1 and 1141.3 $mAhg^{-1}$, respectively during first cycle at 100 $mAhg^{-1}$ and supplied a capacity of 1141.3 $mAhg^{-1}$ after 100 cycles, at a current density of 500 $mAhg^{-1}$. Moreover, at different current densities of 0.5, 1, 3, and 5 Ag^{-1} the delivered discharge capacities of this electrode were 1179.7, 1068.1, 708.9, and 596.4 $mAhg^{-1}$ respectively, in parallel. Choudhury et al. [120] reported the electrochemical performance of doped Si/Graphite/V_2C MXene composite as anode of LIB in a potential range of 0.01-3.0 V. The unique structure of doped Si/G/V_2C MXene electrode served to withstand the volume surge of Si and doping the MXene produced more number of electrons and ion transport pathways which resulted in much higher performance with the capacity of 3682 $mAhg^{-1}$ compared to the capacity of 2833 $mAhg^{-1}$ for the undoped one, at a rate of 1 C. In addition, the doped Si/G/V_2C exhibited a high reversible capacity of 2439 $mAhg^{-1}$ at a high rate of 10 C and the capacity was restored to 3491 $mAhg^{-1}$ when the current rate returned to 1 C.

Zhao et al. [121] modified the surface of Ti_3C_2 MXene sheet by the atomic dispersion of Fe and analyzed the electrochemical performance of Fe-Ti_3C_2 MXene as anode of lithium ion battery. As prepared Fe-$Ti_3C_2T_x$ electrode exhibited superior rate performance with the capacities of 564.9, 400, 260.2, 183.7 and 109.8 $mAhg^{-1}$ compared to the capacities of 77, 68.8, 53, 40.8 and 23.9 $mAhg^{-1}$ of Ti_3C_2 electrode at the current densities of 50, 100, 200, 300 and 500 mAg^{-1} respectively, under -10^0 C. The superior performance of composite anode could be attributed to the formation of weaker Fe-O bond with O atoms of surface functional group in the Fe-

$Ti_3C_2T_x$ sheets. This weaker bond produced unsaturated O atoms which promoted Li+ adsorption and improved the capacity. Huang et al. [122] intercalated Fe ion into the interlayer of pillared few layered Ti_3C_2 MXene. The few layered Ti_3C_2 MXene prevented large scale volume change of Fe nanocomplex during lithiation and delithiation process and expanded interlayer provided more lithium ion storage space. As a result, the Fe-f- Ti_3C_2 MXene supplied excellent initial discharge and charge capacity of 795 and 470 $mAhg^{-1}$, with an initial efficiency of 59.11% at a current density of 50 mAg^{-1}. Moreover, after 150 cycles, the composite MXene maintained a capacity of 535 $mAhg^{-1}$ which was much higher in comparison to 142 $mAhg^{-1}$ of f- Ti_3C_2 at the current density of 500 mAg^{-1}.

Wan et al. [123] successfully fabricated bimetal (Fe-Ti) oxide/carbon/$Ti_3C_2T_x$ MXene electrode for high performance LIB. As prepared composite electrode displayed superior initial discharge and charge capacities of 1462.2 and 1117.9 $mAhg^{-1}$ respectively, corresponding to an efficiency of 77.52% and in addition it delivered a discharge capacity of 757 $mAhg^{-1}$, after 800 cycles, at a current density of 3 Ag^{-1}. This outstanding lithium storage ability of this composite was due to the remarkable conductivity of carbon and MXene and the high capacity of bimetal (Fe-Ti) oxide as well as the distinctive 2D layered structure that allowed multiple open channels for quick electrolyte access, with internal void space that mitigated the enormous volumetric expansion during cycling.

Zhang et al. [124] synthesized the N-Ti_3C_2/Fe_2O_3 nanocomposite MXene by dispersion of iron oxide on crumpled nitrogen doped MXene sheet and compared its performance with $Ti_3C_2T_x/Fe_2O_3$ and N–Ti_3C_2 as anode of LIB. Among all these, the N–Ti_3C_2/Fe_2O_3 electrode delivered the best performance with a high reversible capacity of 688 $mAhg^{-1}$ after 100 cycles, at a current density of 1 Ag^{-1}. However, following the same cycles, the $Ti_3C_2T_x/Fe_2O_3$ composites and N-Ti_3C_2 only exhibited discharge capacities of 438 $mAhg^{-1}$ and 140 $mAhg^{-1}$, respectively. Furthermore, the N–Ti_3C_2/Fe_2O_3 electrode showed excellent rate performance with the capacities of

1065, 993, 806, 672, 477and 304 $mAhg^{-1}$ at the current densities of 0.1, 0.2, 0.5, 1, 2 and 4 Ag^{-1} respectively. The high performance of N-Ti_3C_2/Fe_2O_3 nanocomposite was attributed to the N doping on the MXene sheet that boosted its overall electronic conductivity and crumpled structure which leads to larger specific surface area. In addition, the N–Ti_3C_2 nanosheets and Fe_2O_3 nano particles functioned as mutual spacers in the composite to successfully stop the nanoparticles from aggregating and the MXene nanosheets from stacking. He et al. [125] investigated the electrochemical performance of β-FeOOH nanorods intercalated β-FeOOH/$Ti_3C_2T_x$ composite MXene as anode of LIB. This sandwich like β-FeOOH/$Ti_3C_2T_x$ MXene as in Fig. 2.18 provided high discharge capacity of 1630 $mAhg^{-1}$ during first cycle and retained a capacity of 938 $mAhg^{-1}$ at the end of 100 cycles, at a current density of 200 mAg^{-1}. In addition, this MXene displayed good rate performance with a capacity of 791 $mAhg^{-1}$, at 1 Ag^{-1}.

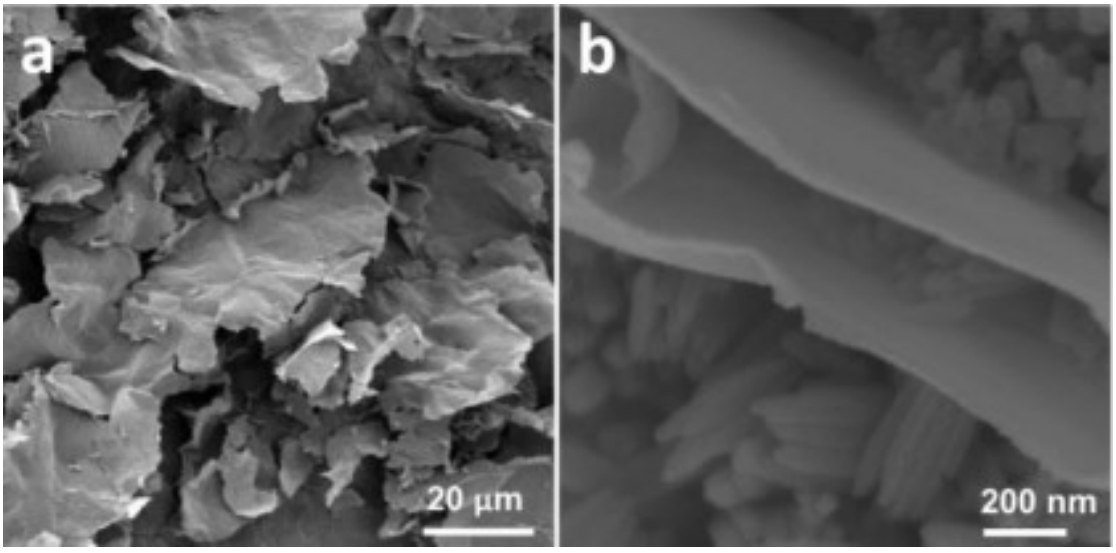

Figure 2.18 SEM images of (a) the prepared Ti_3C_2 and (b) FeOOH/Ti_3C_2 composite (adapted from [125]**)**.

Nam et al. [126] incorporated functionalize titanium carbide nanorods on the surface of $Ti_3C_2T_x$ MXene nanosheet and revealed its performance as anode of LIB. As prepared FTCN-Ti_3C_2 MXene displayed excellent discharge capacities of 1171 $mAhg^{-1}$, 1077 $mAhg^{-1}$ and 1034 $mAhg^{-1}$ in the first, 2nd cycle, and 250th cycles respectively,

at a rate of 0.1 C. Moreover, at varied rates of 0.1, 0.3, 0.5, 1, and 3 C, the supplied capacities were 1133, 1023, 962, 843, and 692 $mAhg^{-1}$ respectively. Lv et al. [127] produced a Ti_3C_2 MXene-based carbon doped TiO_2/Fe_2O_3 composite designated as C-TiO_2/Fe_2O_3-Ti_3C_2 and analyzed the performance of this MXene as anode of LIB as shown in Fig. 2.19. The C-TiO_2/Fe_2O_3-Ti_3C_2 composite anode delivered a better initial discharge capacity of 538 $mAhg^{-1}$, at a current density of 0.1 Ag^{-1}. Moreover, at varied current densities of 0.2, 0.5, 1, 2, and 5 Ag^{-1}, the supplied discharge capacities for this electrode were 386, 320.5, 274.1, 218.1, and 152.6 $mAhg^{-1}$ respectively. This remarkable electrochemical performance was attributed to the combined influence of carbon doping, layered TiO_2 structures, and hybridization of Fe_2O_3, all of which greatly accelerated the transfer of charges.

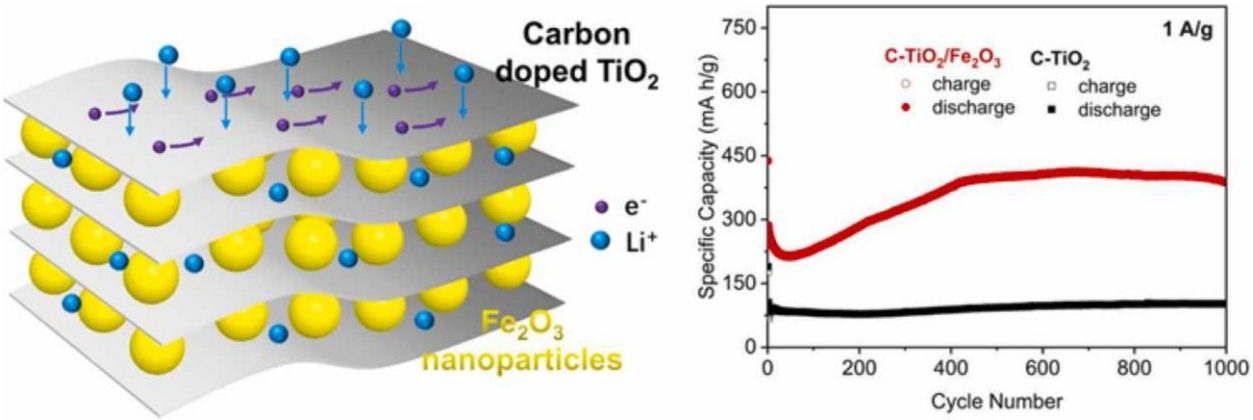

Figure 2.19 Schematic representation of C-TiO_2/Fe_2O_3-Ti_3C_2 MXene with cyclic performance curves at 1 Ag^{-1}. (Adapted from[127])

Wu et al. [128] explored the electrochemical performance of Sn nanoconfined $Ti_3C_2T_x$ composite MXene as anode of LIB. In Sn-$Ti_3C_2T_x$ MXene, the Sn nanoparticles enclosed between the spaces of $Ti_3C_2T_x$ MXene and acted as pillar and helped to increase interlayer space and restricted the sheet stacking as well as revealed additional sites for Li-ion storage whereas Ti_3C_2 limited the volume expansion of Sn nanoparticles during cycling. Hence, this MXene electrode exhibited good initial discharge and charge capacity of 445 and 374.7 $mAhg^{-1}$, respectively, at a current

density of 200 Ag^{-1} and maintained a capacity of 186.9 $mAhg^{-1}$, after 180 cycles, corresponding to a current density of 100 mAg^{-1}.

Luo et al. [129] prepared PVP-Sn(IV)@Ti_3C_2 nanocomposites MXene by successful anchoring of Sn^{4+} on the alkalized Ti_3C_2 MXene via electrostatic interaction. The presence of PVP assisted in reduction of particles size and stopped the material from clumping together during the chemical reaction. In addition, strong chemical adsorption between Sn^{4+} and negatively charged alkalized Ti_3C_2 MXene surface with -OH and -F resulted in superior electrochemical performance of PVP-Sn(IV)@Ti_3C_2 nanocomposites MXene than graphite and pristine Ti_3C_2 MXene. During testing in the range of 0.01 to 3V, the displayed first cycle discharge and charge capacities of this composite were 1487 and 851 $mAhg^{-1}$ respectively and observed a capacity of 635 $mAhg^{-1}$ after 50 cycles at a current density of 0.1 Ag^{-1}. Ahmed et al. [130] reported uniformly coated Ti_3C_2 MXene sheet by various thickness of SnO_2 nanoparticles with the help of ALD reactor at two different temperatures of 150^0 and 200^0C. The coating thicknesses of SnO_2 were varied from 5 to 50 nm. The SnO_2/Ti_3C_2 (ALD@200) MXene with 50 nm coating thickness supplied superior initial discharge and charge capacities of 1463 and 1041 $mAhg^{-1}$ compared to the capacities of 1024 and 583 $mAhg^{-1}$ of 10 nm coated SnO_2/Ti_3C_2 (ALD@200) MXene, at the current density of 100 mAg^{-1}. However, the capacity of 50 nm coated MXene faded drastically due to the inability of MXene sheet to allow for the shift in volume of large amount of SnO_2 nano particles and showed the capacities of 239 (ALD@150) and 451 $mAhg^{-1}$ (ALD@200) after 50 cycles with nearly 50% capacity retention, at 500 mAg^{-1}. Furthermore, to overcome the capacity fading problem the surface of MXene were coated by HfO_2 by using ALD to form dual oxide on the surface which guided to improved cyclic stability with the capacity of 843 $mAhg^{-1}$, after 50 cycles, at 500 mAg^{-1} current rate.

Liu et al. [131] intercalated the SnO_2 nanoparticles over the surface of V_2CT_x MXene and reported the performance of V_2CT_x-SnO_2 MXene as anode of LIB for different

ratio of V_2CT_x and SnO_2 . At a current density of 50 mAg^{-1}, The five samples of V_2C such as 1:0.5 V_2CT_x-SnO_2, 1:1 V_2CT_x-SnO_2, 1:2 V_2CT_x-SnO_2 and SnO_2 were delivered the initial discharge/ charge capacities of 845/554, 1739.9/1022.03, ~2410.8/~1525.85, ~2449.4/~853.69 and 2728/`1123 $mAhg^{-1}$ respectively, corresponding to the coulombic efficiencies of 65.5%,~58.7%, ~63.3%, ~34.8% and `41.2% respectively. After 10 cycles, the discharge capacities were reached to 410, 799.7, 1226.8, 806.2 and 956.5 $mAhg^{-1}$ respectively. Furthermore, after 200 cycles, when the current density reached to 1 Ag^{-1}, the specific discharge capacities of five samples were obtained as 143.89, 329, 768, 413.4 and 0.9 $mAhg^{-1}$ respectively. Fan et al. [132] anchored the nanoparticles of Sn_4P_3 over the surface of $Ti_3C_2T_x$ MXene to produce Sn_4P_3-$Ti_3C_2T_x$ composite MXene anode for high performance LIB. The prepared Sn_4P_3-$Ti_3C_2T_x$ anode showed superior performance than that of conventional anode with the initial discharge and charge capacities of 1138 and 936 $mAhg^{-1}$ respectively, at a current density of 0.1 Ag^{-1}. Moreover, at different current densities of 0.1, 0.5, 1, 5 Ag^{-1} the observed discharge capacities of this electrode were 963, 744, 703 and 582 $mAhg^{-1}$ respectively. The high electrochemical and structural stabilities were obtained due to the sandwich structure and potential internal links in the resultant Sn_4P_3-$Ti_3C_2T_x$ hybrid.

Li et al. [133] produced a Ti_3C_2 composite MXene decorated by SnS_2/Sn_3S_4 hybrid through solvothermal and calcination process. As fabricated MXene delivered excellent first cycle discharge and charge capacity of 1348 $mAhg^{-1}$ and 707.16 $mAhg^{-1}$ respectively, corresponding to a coulombic efficiency of 37.2%, and retained a specific capacity of 426.3 $mAhg^{-1}$ after 100 cycles at a current density of 100 mAg^{-1}. In addition, at increasing current densities of 200, 500, 1000 and 5000 mAg^{-1} the observed capacities for this MXene were 540.4, 479.4, 423.9, 216.5 $mAhg^{-1}$ respectively. The SnS_2/Sn_3S_4 nano particles with large surface area in the composite acted as a spacer to lessen the propensity of layer stacking and improved the contact between electrolyte and electrode that resulted in enhancement of Li-ion storage capacity of this MXene.

Zhu et al. [134] synthesized SnO_2-Ti_2C-C composite anode by homogeneous coating of graphite with SnO_2-Ti_2C nanoparticles. The SnO_2-Ti_2C-C anode provided excellent and long term cycling stability as SnO_2 possessed many active sites and created shorter channels for charge transfer and graphite limited the volume expansion during cycling. Therefore, this anode exhibited superior initial charge and discharge capacities of 1741.1 and 2167.3 $mAhg^{-1}$, with a coulombic efficiency of 80.3%. For second and third cycle the efficiency were reached to 95.1 % and 98.1% respectively. At different current densities of 0.2, 0.5, 1, 2 and 3 Ag^{-1} the supplied specific capacities were 1231.32, 998.76, 812.54, 617.63 and 525.36 $mAhg^{-1}$ respectively. When the current density was 0.2 Ag^{-1}, the SnO_2-Ti_2C-C anode retained a specific capacity of 1036.87 $mAhg^{-1}$ after 200 cycles. Zuo et al. [135] fabricated a nanostructured Sn/SnO_x-$Ti_3C_2T_x$ composite MXene electrode by insertion of Sn/SnO_x nanoparticles on the surface $Ti_3C_2T_x$ nanosheet through electrostatic attraction and liquid phase reduction. As prepared electrode provided a specific capacity of 1169.4 and 1981.3 $mAhg^{-1}$ during first charge and discharge cycle by retaining a coulombic efficiency of 59%, whereas 1473.9 and 481 $mAhg^{-1}$ discharge capacity was observed in case of pure Sn/SnO_x and $Ti_3C_2T_x$,corresponding to the efficiency of 36.4% and 35.3% respectively. This superior performance of Sn/SnO_x-$Ti_3C_2T_x$ was attributed to the prevention of volume expansion and agglomeration of nanoparticles by $Ti_3C_2T_x$ and pillaring of Sn/SnO_x which tackled sheet stacking and enhanced the Li^+ storage by broadened the interlayer spacing.

Tariq et al. [136] synthesized Ti_3C_2/TiO_2 composite MXene by Entrusting TiO_2 over the 2 and 5 wt% Ti_3C_2 MXene solution. As an anode of lithium ion battery, The 5 wt% Ti_3C_2/TiO_2 and 2 wt% Ti_3C_2/TiO_2 MXene exhibited initial discharge capacity of around 200 $mAhg^{-1}$ and 183 $mAhg^{-1}$ respectively and supplied a discharge capacity of 180 $mAhg^{-1}$ and 165 $mAhg^{-1}$ respectively, after 100 cycles, at 0.1 C. The better result of 5 wt% Ti_3C_2/TiO_2 MXene was because of a wider surface area of 77.78 m^2/g compared to the 55.68 and 16.25 m^2/g of 2 wt% Ti_3C_2/TiO_2 MXene and pristine

MXene respectively. Moreover in 5 wt% Ti_3C_2/TiO_2 MXene the TiO_2 fully cover the surface and effectively tackled the layer stacking, whereas in case of 2 wt% Ti_3C_2/TiO_2 the TiO_2 agglomerates due to its insufficient area. Jia et al. [137] emanated $Ti_3C_2T_x$ MXene from Ti_3AlC_2 by using 46 wt% HF as etchant and decorated its surface by TiO_2 nanoparticles to create Ti_3C_2/TiO_2 composite MXene. As anode of LIB, the supplied discharge capacities of this composite MXene for first three cycles were 552, 301, and 298 $mAhg^{-1}$ respectively at a scan rate of $0.1mVs^{-1}$. The capacity decay was due to the structural damage of anode and formation of SEI film on the electrode. At increasing current densities of 0.1, 0.2 0.5 and 1 Ag^{-1} the observed capacities for the MXene were 296, 275, 221, and 188 $mAhg^{-1}$, respectively. In addition, after 100 cycles, this MXene displayed an excellent capacity of 275 $mAhg^{-1}$, at 0.2 Ag^{-1}. Ahmed et al. [138] generated TiO_2 nano crystals over the surface of Ti_2CT_x MXene sheet by oxidation in H_2O_2 solution at room temperature. As synthesized TiO_2/Ti_2C hybrid MXene displayed superior performance as anode of LIB. At the current densities of 100, 500 and 1000 Ag^{-1}, the supplied discharge capacities of this electrode were 1015, 826 and 681 $mAhg^{-1}$ respectively in the first cycle and in the 2^{nd} cycle the discharge capacities were 507, 429 and 384 $mAhg^{-1}$ respectively, moreover, after 50 cycles, the delivered discharge capacities were 389, 337 and 297 $mAhg^{-1}$ respectively. Zhang et al. [139] revealed the performance of few layered MoS_2 wrapped $Ti_3C_2T_x$ MXene decorated with TiO_2 nanaparticles (denoted as Ti_3C_2/TiO_2@f-MoS_2) as anode of LIB. The multilayered Ti_3C_2 with TiO_2 nanoparticles effectively improved the stability by providing abundant interspace for electron transport, preventing the aggregation of f-MoS_2 and offered sufficient space. In contrast, the f-MoS_2 with larger interlayer facilitated lithium-ion diffusion and restrained the restacking of multilayer Ti_3C_2. As a result, the Ti_3C_2/TiO_2@f-MoS_2 MXene delivered excellent first cycle discharge and charge capacities of 910.7 and 685.2 $mAhg^{-1}$, with a high coulombic efficiency of 75.2% and a capacity of 490.7 $mAhg^{-1}$ after 100 cycles, at a current density of 100

mAg^{-1}. In addition, at increasing current densities from 0.1 to 5 Ag^{-1} the supplied capacities were varied from 613.1 to 40.3 $mAhg^{-1}$.

He et al. [140] modified the surface of $Ti_3C_2T_x$ MXene by LaF_3 and compared its performance with pristine $Ti_3C_2T_x$ MXene as anode of LIB. It was observed that, the $Ti_3C_2T_x$-LaF_3 electrode supplied higher performance with initial discharge and charge capacity of 340 and 223 $mAhg^{-1}$ respectively in comparison to the discharge and charge capacities of 238 and 131 $mAhg^{-1}$ for pristine $Ti_3C_2T_x$ under a current density of 50 $mAhg^{-1}$. Moreover, at a current density of 1000 mAg^{-1}, the $Ti_3C_2T_x$-LaF_3 showed a higher reversible capacity of 89.2 $mAhg^{-1}$ compared to 76.9 $mAhg^{-1}$ of $Ti_3C_2T_x$ after 50 cycles. Capacity and rate ability of the composite MXene was improved by the formation of LaF_3 on the surface of $Ti_3C_2T_x$ MXene which lowered the resistance and impedance and enhanced the Li-ion diffusion rate.

Yuan et al. [141] synthesized sulfar decorated Ti_3C_2 MXene as anode of LIB. Due to the incorporation of S, the pore sizes were enlarged from 10 to 22.4 nm and as well as the surface area were increased to 91.7 from 64.1 m^2/g. The S decorated Ti_3C_2 MXene provided an initial discharge capacity of 305 $mAhg^{-1}$ and after 100, 200 and 400 cycles, the capacities remained at 167.8, 170.2 and 166.3 $mAhg^{-1}$ with high coulombic efficiencies of 99.76%, 99.92% and 100% under a current density of 0.5 Ag^{-1}. In addition, the rate performance at varied current densities of 0.5, 1, 1.5, 2, and 2.5 Ag^{-1}, the S–$Ti_3C_2T_x$ MXene delivered much higher discharge capacities of 220.2, 138.5, 126.9, 121, 117.5 $mAhg^{-1}$ compared to 210.4, 74.7, 60.2, 50.6, 46 $mAhg^{-1}$ for $Ti_3C_2T_x$ electrode, respectively. Zhang et al. [142] recently explored the effect of PVDF and CMC binder on the performance of the S-$Ti_3C_2T_x$ MXene electrode as shown in Fig. 2.20. Test was carried out for the S-$Ti_3C_2T_x$ MXene electrode (mass ratio of 1:7) with CMC and PVDF binder. The electrode with CMC and PVDF binder had an initial discharge capacity of 1226.8 and 858.8 $mAhg^{-1}$, at a current density of 50 mAg^{-1}. As the current density increased to 1000 mAg^{-1}, the displayed initial capacities were 372.9 and 117.8 $mAhg^{-1}$, subsequently, after 2550 cycles, the

maintained capacities were 858.9 and 424.1 $mAhg^{-1}$ respectively, for CMC and PVDF binder electrodes. Higher adhesion force, better diffusivity of lithium ions, and lowered charge transfer resistance were considered to be the causes of the CMC binder's superior performance over the PVDF binder.

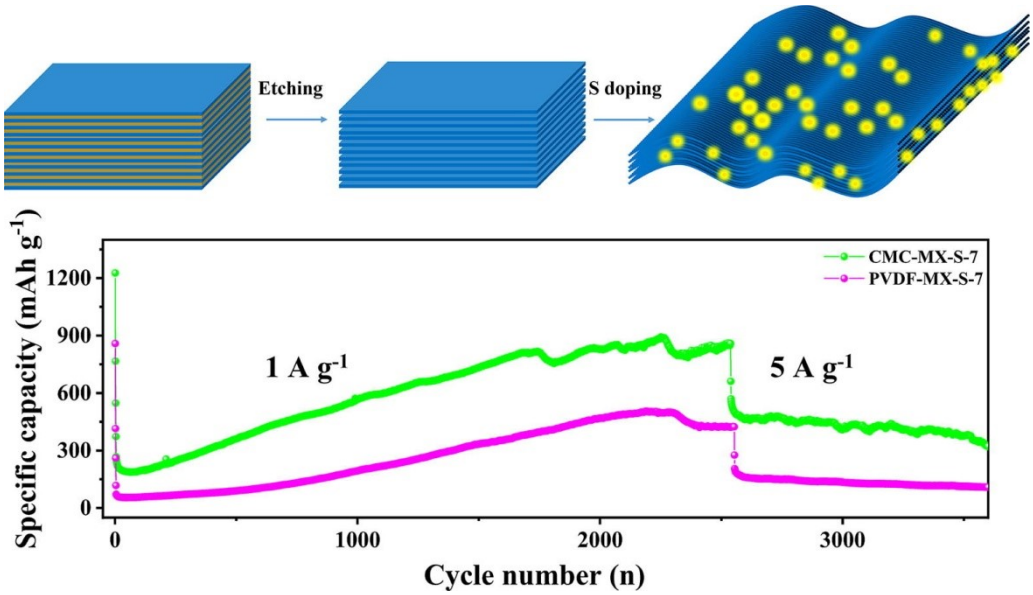

Figure 2.20 Cyclic performance curves for S-$Ti_3C_2T_x$ MXene with CMC and PVDF binder (Adapted from [142])

Zou et al. [143] revealed that the electrochemical performance of Ti_3C_2 MXene was well improved with the insertion of Ag nanoparticles over the surface of the MXene sheet. As prepared Ti_3C_2/Ag MXene displayed superior discharge capacities of 550 and 330 $mAhg^{-1}$ in the first and second cycle respectively, at a rate of 1C. On the contrary, the delivered capacities of Ti_3C_2 MXene were 420 and 250 $mAhg^{-1}$ corresponding to the same cycle. In addition, at different current rates of 5, 10, 20, and 50 Ag^{-1} the observed capacities for Ti_3C_2/Ag MXene were 131.5, 100.7, 86.6, and 47.4 $mAhg^{-1}$, respectively. More remarkably, a capacity of 150 $mAhg^{-1}$ was retained even after 5000 cycles, at a rate of 50 C. Wang et al. [144] constructed Ag nanoparticles decorated 3D honeycomb-like hollow $Ti_3C_2T_x$ composite MXene structure as the anode of LIB to boost up the Li^+ storage performance compared to 2D Ti_3C_2 MXene alone as in Fig. 2.21. Ag nanoparticles were uniformly grafted into the 3D hollow multiporous Ti_3C_2 MXene framework, which prevented Ti_3C_2 MXene

flakes from building up or accumulating in layers. The fabricated 3D $Ti_3C_2T_x$/Ag composite MXene anode provided a high initial capacity of 611.3 $mAhg^{-1}$, corresponding to an efficiency of 57.9% at a current density of 100 mAg^{-1}. Moreover, at gradually increasing current densities of 0.1, 0.5, 1, 2, 3, and 4 Ag^{-1}, the delivered reversible capacities were 680.5, 495.9, 399.9, 349.2, 311.4, and 226.7 $mAhg^{-1}$, respectively.

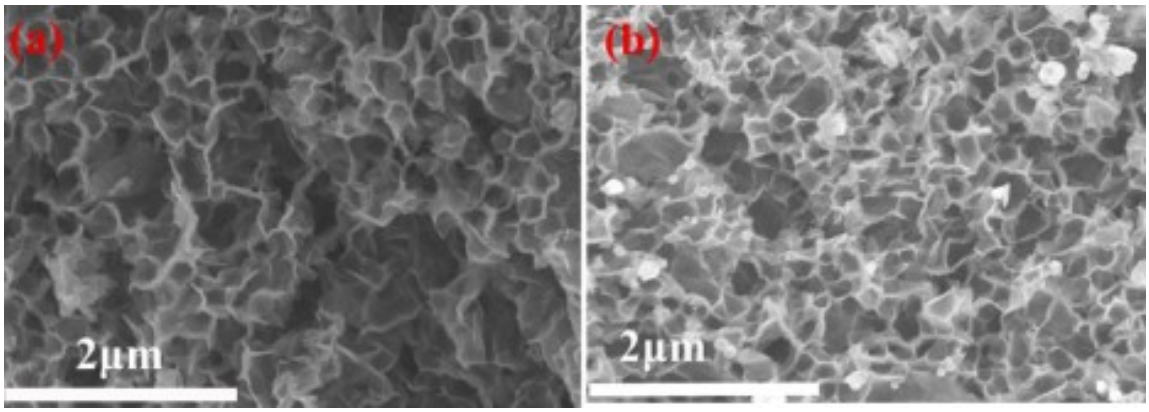

Figure 2.21 (a) SEM image of 3D Ti_3C_2; (b) SEM image of 3D Ti_3C_2/Ag [144].

Huang et al. [145] tested the electrochemical performance of Li_3VO_4/Ti_3C_2 composite MXene as anode of LIB. Li_3VO_4/Ti_3C_2 composite MXene was produced by uniform insertion of Li_3VO_4 onto a multilayer $Ti_3C_2T_x$ MXene by using sol-gel method. This type of anode material provided superior rate performance with the capacities of 420, 311, 272, 165 and 117 $mAhg^{-1}$ corresponding to the rates of 0.1, 0.5, 1, 5 and 10 C, respectively. In addition this composite MXene exhibited much higher cyclic stability of 146 $mAhg^{-1}$ compared to 40 $mAhg^{-1}$ and 71 $mAhg^{-1}$ of LVO and graphite respectively, after 1000 cycles, at 5C.

Liu et al. [146] introduced nitrogen onto the surface of the MXene nanosheet by hydrothermal reaction of Nb_2CT_x MXene with urea. As prepared, N-Nb_2CT_x MXene provided more than two times enlarged surface area of 120 m^2g^{-1} compared to the 55m^2g^{-1} of Nb_2CT_x. As anode of LIB, the N-Nb_2CT_x MXene delivered a first cycle capacity of 380 $mAhg^{-1}$ with a coulombic efficiency of 98% and retained a reversible capacity of 360 $mAhg^{-1}$ after 100 cycles at a current density of 0.2C. Moreover, after

1500 cycles, the N doped MXene maintained a capacity of 288 $mAhg^{-1}$, which was much higher than that of 124 $mAhg^{-1}$ for pristine Nb_2C, at 0.5 C. Zhong et al. [147] homogeneously anchored MgH_2 nanoparticles on the surface of Ti_3C_2 MXene sheets by bottom up self-assembly strategy and analyzed the performances of as-prepared composite MXene as anode of LIB with different weight ratio of MgH_2 and Ti_3C_2. The reported initial capacities of four types of MgH_2/Ti_3C_2 electrode where the content of MgH_2 varied as 20, 40, 60 and 80% were 629.5, 792.2, 1051.2, 830.4 $mAhg^{-1}$ respectively, at a current density of 100 mAg^{-1}. The performances were enriched gradually with MgH_2 content. However, when MgH_2 content exceeded 60% the performance started to diminish as these particles were accumulated on the surface of MXene. Hence, the MgH_2-60/Ti_3C_2 provided optimum electrochemical performances among all electrodes and maintained a capacity of 389.3 $mAhg^{-1}$ after 100 cycles, at same current density. The improved capacity, cyclability and rate performance were resulted due to the unique two dimensional nanoarchitectures that accelerated the transfer of electrons and lithium ions, inhibited the pulverization of active materials and more crucially the F-Mg bounding between MgH_2 and Ti_3C_2 which prevented the shedding of MgH_2 nanoparticles into the electrolyte during cycling.

Liu et al. [148] fabricated GeO_x/Ti_3C_2 composite MXene anode with two different combinations of binder and solvent. First one was PVDF binder with NMP solvent based anode named as GeO_x/Ti_3C_2/PVDF(NMP) and the other one was Li-PAA binder with DI-water solvent based named as GeO_x/Ti_3C_2/Li-PAA(DI-water). Between these two, the GeO_x/Ti_3C_2/Li-PAA(DI-water) electrode displayed better electrochemical stability with a capacity of 1026 $mAhg^{-1}$ after 50 cycles, at a current density of 200 mAg^{-1}. On the contrary, the GeO_x/Ti_3C_2/PVDF(NMP) retained a capacity of 826 $mAhg^{-1}$ after same cycles and same current density. Melchoir et al. [149] investigated the performance of Ti_2CT_x/electrolytic manganese dioxide (EMD) composite MXene with different weight ratios of Ti_2CT_x: EMD (i.e Ti_2CT_x:EMD =

20:80; 50:50; 80:20) as anode of lithium ion battery. The inclusion of EMD with the MXene matrix leading to the opening of interlayer gaps and facilitating improved Li-ion accessibility. However, over a particular ratio of EMD content inhibited the properties. Hence, among all compositions the electrode with MX:EMD=80:20 ratio exhibited reduced charge transfer resistance and surface film and delivered superior performance with the capacities of 570 $mAhg^{-1}$ in the first cycle, 272 $mAhg^{-1}$ in the 2nd cycle and 460 $mAhg^{-1}$ after 200 cycles at the current densities of 100 mAg^{-1}. In addition, at the current density of 1000 mAg^{-1}, a much higher capacity of 160 $mAhg^{-1}$ was observed compared to 90 $mAhg^{-1}$ of Ti_2CT_x: EMD (20:80) and 86 $mAhg^{-1}$ of 50:50 ratio, after 1000 cycles with nearly 100% capacity retention.

Zhang et al. [150] synthesized the heterostructured $Bi_2MoO_6/Ti_3C_2T_x$ MXene by combining positively charged Bi_2MoO_6 nanoplates with negatively charged $Ti_3C_2T_x$ MXene sheets. As prepared $Bi_2MoO_6/Ti_3C_2T_x$-30% (Bi_2MoO_6:$Ti_3C_2T_x$ =70:30) composite MXene exhibited excellent initial discharge and charge capacities of 844.2 and 615.5 $mAhg^{-1}$, respectively, with an efficiency of 72.9% at 100 mAg^{-1}. Though the initial coulombic efficiency of $Bi_2MoO_6/Ti_3C_2T_x$ -30% was lower than those of $Bi_2MoO_6/Ti_3C_2T_x$ -10% (76.6%) and Bi_2MoO_6 (82.6%), However, the supplied capacity after 200 cycles for $Bi_2MoO_6/Ti_3C_2T_x$ -30% (692 $mAhg^{-1}$) was much higher than that of $Bi_2MoO_6/Ti_3C_2T_x$ -50% (617.5 $mAhg^{-1}$), $Bi_2MoO_6/Ti_3C_2T_x$ -10% (497.6 $mAhg^{-1}$), and Bi_2MoO_6 (416.1 $mAhg^{-1}$) at the same current density.

Abdah et al. [151] investigated the performance of activated carbon (AC) integrated $Ti_3C_2T_x$ hybrid electrode as anode of LIB. This composite electrode displayed excellent initial discharge capacity of 1194.2 $mAhg^{-1}$ and offered a reversible capacity of 841.8 $mAhg^{-1}$ with capacity retention of 70.5%, after 80 cycles, at a current density of 0.2 Ag^{-1}. The superior performance of AC-$Ti_3C_2T_x$ electrode could be attributed to the presence of few layered unique morphology of Ti_3C_2 MXene which provided abundant active sites for Li+ intercalation, enhanced transportation and diffusion rate of ion and electron and inclusion of AC which acted as an interlayer spacer

between the layers of MXene and provided large numbers of ion/electron transfer channels. Liu et al. [152] successfully assembled VO_2-NTs/Ti_3C_2 MXene as anode of LIB. This VO_2-nanotubes linked Ti_3C_2 MXene electrode exhibited superior initial discharge and charge capacities of 2132 and 1164 $mAhg^{-1}$ respectively, with an initial coulombic efficiency of 54%, at 0.1 Ag^{-1}. However coulombic efficiency was increased to 95% in the next cycle. Moreover, excellent rate capability was also observed with a specific capacity of 703 $mAhg^{-1}$, under a current density of 10 Ag^{-1}. This may be attributed to the combination of 1D VO2-NTs nanostructures with 2D Ti3C2 nanosheets that created several multidimensional channels for the transfer of ions and electrons and provided large number of reaction sites for electrochemical processes.

Ma el al. [153] generated niobium doped TiO_2 arrays on the surface of double transition $TiNbCT_x$ MXene (denoted as TiNbC@NTO) and explored the effect of oxidation temperature on the electrochemical performance of this composite as anode of LIB. The oxidation process was carried out for three different temperatures of 300, 500 and 700^0 C and observed performance showed that, at 0.1 Ag^{-1}, the supplied charging capacity after 100 cycles, for TiNbC@NTO-300, TiNbC@NTO-500 and TiNbC@NTO-700 electrodes were 278.4, 295 and 303.1 $mAhg^{-1}$ respectively. However, during long cycle performance test, the TiNbC@NTO-500 electrode exhibited higher stability than the other electrodes with a capacity of 261 $mAhg^{-1}$, after 500 cycles, at a current density of 1 Ag^{-1}. The ideal synergistic impact between MXene layer and Nb doped TiO_2 were thought to be contributor of this cycling stability.

Xu et al. [154] constructed $VNbO_5$ metallic oxide over the surface of $VNbCT_x$ MXene via partial oxidation at 500^0C (denoted as VNbC@VNO-500). Partial oxidations strengthen the bond between $VNbO_5$ and $VNbCT_x$ MXene and effectively improved the electrochemical performance. As anode of LIB, the prepared VNbC@VNO-500 MXene provided excellent cyclic stability with a specific capacity of 400.3 $mAhg^{-1}$

after 100 cycles under a current density of 0.1 Ag^{-1} as shown in Fig. 2.22. In addition, this electrode material displayed promising rate performance with specific capacities of 327.3, 306.6, 270.7, 222.4, 181.7, 141.2 $mAhg^{-1}$ at the current densities of 0.1, 0.2, 0.5, 1.0, 2.0, and 5.0 Ag^{-1}, respectively.

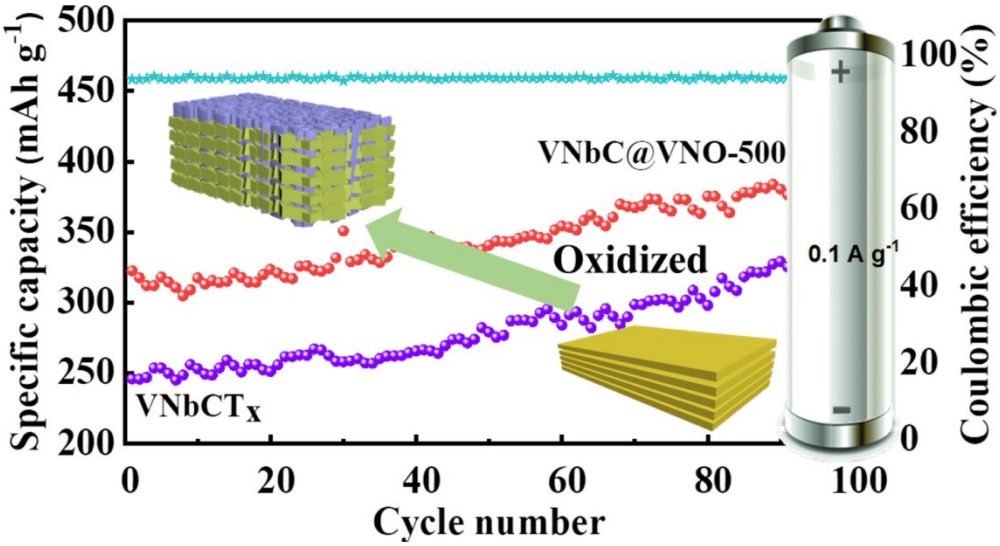

Figure 2.22 Cyclic stability curves of VNbC@VNO-500 and $VNbCT_x$ MXene at 0.1 Ag^{-1}. (Adapted from [154]).

Luo et al. [155] fabricated sandwich like structured $Na_2Ti_3O_7$ / Ti_3C_2 composite MXene as anode of LIB. This composite electrode displayed high discharge and charge capacities of 405 $mAhg^{-1}$ and 337 $mAhg^{-1}$ in the first cycle and retained a specific capacity of 263 $mAhg^{-1}$, after 100 cycles, at a current density of 0.1 Ag^{-1}. Moreover, at various current rates of 0.1, 0.2, 0.4, 0.6, 0.8, 1, and 2 Ag^{-1}, the observed capacities for the electrode were reported as 361.7, 288.7, 240.4, 223.6, 209.4, 207.7, and 177.8 $mAhg^{-1}$, respectively.

Gong et al. [156] reported the performance of $TiNb_2O_7/Ti_3C_2$ composite MXene as anode of LIB. In $TiNb_2O_7/Ti_3C_2$ structure, the $TiNb_2O_7$ nanoparticles connected with MXene nanoflakes and created a 3D conductive network which facilitates the transfer of ion/electron. In addition, this composite MXene offered 4 times higher conductivity than that of $TiNb_2O_7$. As a consequence, the $TiNb_2O_7/Ti_3C_2$ MXene exhibited improved discharge/charge capacities of 388.4/349 $mAhg^{-1}$ during first

cycle, at a current density of 0.1 C. In addition, at gradually varied rates of 0.1, 0.5, 1, 2, 5, 10, and 20C, the supplied capacities of this electrode were 346.4, 302.4, 284.2, 262.2, 262.2, 198, and 166 $mAhg^{-1}$, respectively. Qi et al. [157] fabricated chlorophyll (zinc methyl 3-devinyl-3-hydroxymethyl-pyropheophorbide (Chl)) intercalated Chl@Nb_2C composite MXene and compared the performance of three different samples of 1 %(wt/wt) Chl@Nb_2C (mass ratio of Chl: Nb_2C=1:100), 2 %(wt/wt) Chl@Nb_2C and Nb_2C as the anode materials of LIB. It was observed that,, the 1 %(wt/wt) Chl@Nb_2C MXene delivered a higher specific capacity of 384 $mAhg^{-1}$ compared to the other two samples of 363 $mAhg^{-1}$ (2 %(wt/wt) Chl@Nb_2C) and 295 $mAhg^{-1}$ (Nb_2C) respectively, at a current density of 100 mAg^{-1}. In addition, at increasing current densities from 0.1 to 1 Ag^{-1}, the observed specific capacities were varied from 247 to 126 $mAhg^{-1}$, 215 to 116 and 201 to 102 $mAhg^{-1}$ for 1 %(wt/wt) Chl@Nb_2C, 2 %(wt/wt) Chl@Nb_2C and Nb_2C respectively.

Tian el al. [158] reported the electrochemical performance of Ti_3C_2/CoS_2 composite MXene as anode of LIB. This composite MXene electrode provided superior specific capacity of 405.8 $mAhg^{-1}$, after 100 cycles, at a current density of 0.1 Ag^{-1} and supplied excellent rate performances with the capacities of 436.9, 387.2, 312.5, 264.8, 209.5, 179.8, and 133.1 $mAhg^{-1}$ corresponding to the rates of 0.1, 0.2, 0.5, 1, 2, 3, and 5 Ag^{-1}, respectively and when the current density switched back to 0.1 Ag^{-1}, the displayed capacity was still 390.8 $mAhg^{-1}$. In addition, 100% capacity retention was observed after 1000 cycles, at a current density of 1 Ag^{-1}. This improved performance was attributed to the formation of the Ti-O-Co bond at MXene interface which enhanced the redox kinetics by promoting ionic diffusivity and electric conductivity. Shen et al. [159] synthesized the MoS_2/Ti_3C_2 composite MXene via solid state sintering method and revealed that, the MoS_2/Ti_3C_2-10 (mass ratio of Ammonium tetrathiomolybdate was 10) electrode delivered better electrochemical performance than the Ti_3C_2, MoS_2 and MoS_2/Ti_3C_2-5 electrodes. The observed discharge/charge capacities of these four electrodes were 178/95.4, 1012.7/843.6, 268.6/141.2 and

386.4/296.1 $mAhg^{-1}$ in the first cycle, at 50 mAg^{-1} and a discharge capacity of 63, 3.6, 76.2 and 131.6 $mAhg^{-1}$ for Ti_3C_2, MoS_2, MoS_2/Ti_3C_2-5 and MoS_2/Ti_3C_2-10 respectively after 200 cycles at a current density of 1000 mAg^{-1}.

Chen et al. [160] produced $MoS_2/Mo_2TiC_2T_x$ composite MXene as anode of LIB. The prepared composite MXene supplied superior initial discharge and charge capacities of 646 and 554 $mAhg^{-1}$ which were 2.4 and 4.1 times higher than pure $Mo_2TiC_2T_x$ MXene (268 and 134 $mAhg^{-1}$ respectively), at a current density of 100 mAg^{-1}. Compared to the restacked pure $Mo_2TiC_2T_x$, the $MoS_2/Mo_2TiC_2T_x$ had an open structure, which minimized the ion diffusion resistance and confirmed the enhancement in capacity. Moreover, at gradually increased current densities of 100, 200, 500, 1000, 2000 and 5000 mAg^{-1} the obtained capacities for this composite electrode were 523, 484, 407, 315, 182 and 90 $mAhg^{-1}$ respectively. Kamat et al. [161] employed selenium enriched and over oxidized Mo_3Se_4 anchored $Ti_3C_2T_x$ composite MXene as anode of LIB. The Mo_3Se_4-$Ti_3C_2T_x$ MXene electrode provided excellent initial discharge capacity of 1930.32 mAhg-^{1} at a cycling rate 0.1 C and for further cycles at the same rate, high stable discharge capacities of 1250.76, 1107.25 and 1067.94 $mAhg^{-1}$ were obtained with a coulombic efficiency of more than 100%. At multiple operating rates of 0.2C, 0.4C, 0.6C and 1C, the observed charge capacities were to be 939.31, 876.72, 857.63, and 809.54 $mAhg^{-1}$ with discharge capacities of 978.24, 904.2, 883.97 and 822.52 $mAhg^{-1}$ respectively. Bai et al. [162] reported the electrochemical performance of thin carbon coated and MoS_2 anchored V_4C_3 MXene (denoted as V_4C_3 /MoS_2/C) as anode of LIB. The thin carbon coating stabilized the connection between V_4C_3 MXene and MoS_2 nonosheets which effectively increased the specific area and shortened the ion diffusion distance. As a result, the V_4C_3 /MoS_2/C electrode provided significantly improved capacity of 622.6 $mAhg^{-1}$ compared to the capacities of 259.6, 30 and 106.9 for MoS_2/C, V_4C_3 and V_4C_3 /MoS_2/C respectively, after 450 cycles at a current density of 1 Ag^{-1}. In addition, high reversible capacities of 827.0, 778.6, 730.7, 674.0, 620.8, 532.6 and 500 $mAhg^{-1}$ were

observed for V_4C_3 /MoS_2/C electrode at the rates of 0.1, 0.2, 0.5, 1, 2, 5 and 10 Ag^{-1} respectively.

Wei et al. [163] explored the performance of 3°C GaInSnZn (calculated mass percent of Ga, In, Sn, and Zn was 69.87%, 15.52%, 13.46%, and 1.15%, respectively) liquid metal incorporated $Ti_3C_2T_x$ MXene as flexible anode of LIB. Liquid metal was confined within the MXene matrix which possessed good wettability and excellent electrical conductivity resulted in improvement of battery energy density. This liquid metal MXene electrode delivered excellent discharge capacities of 638.79, 535.89, and 531.61 $mAhg^{-1}$, in the first three cycles respectively, at 20 mAg^{-1}. Moreover, at various rates of 50, 100, 200, 500, and 1000 mAg^{-1}, the supplied capacities were 507.42, 483.33, 480.22, 452.30, and 404.47 $mAhg^{-1}$ respectively. Zhang et al. [164] depicted the electrochemical performance of carbon coated 3D tremella like $Ti_3C_2T_x$ (denoted as T-$Ti_3C_2T_x$@C) MXene structure as anode of LIB. This T-$Ti_3C_2T_x$@C MXene electrode exhibited superior initial charge capacity of 580.9 $mAhg^{-1}$, with an initial coulombic efficiency of 56.9% and retained a high discharge capacity of 499.4 $mAhg^{-1}$ after 200 cycles, at 0.2 C. At various rates of 0.2, 1, 5, 10, 20 and 50 C the delivered capacities were 478, 329.5, 237.9, 194.7, 142.2 and 102.2 $mAhg^{-1}$ respectively.

Wang et al. [165] reported that, the interlayer distance of V_2C MXene were expanded from 0.735 nm to 0.952 nm due to inclusion of Co nanoparticles which created a strong V-O-Co bonding. The surface area was also increased from 11.6 to 27.3 m^2g^{-1}. As a result, the cobalt intercalated V_2C@Co MXene delivered superior electrochemical performance with initial discharge and charge capacity of 1117.3 and 1006.5 $mAhg^{-1}$ compared to the discharge/charge capacities of 686.7/620.7 $mAhg^{-1}$ for pristine V_2C electrode, at 0.1 Ag^{-1}. In addition, this composite electrode displayed excellent rate performance with a capacity of 199.9 $mAhg^{-1}$, at a current density of 20 Ag^{-1}. Li et al. [166] synthesized the CoO/$Ti_3C_2T_x$ composite MXene as anode of LIB. This CoO coated Ti_3C_2 MXene with 10 times larger surface area than Ti_3C_2 MXene

provided superior initial discharge and charge capacity of 1389 and 850 $mAhg^{-1}$ compared to 415 $mAhg^{-1}$ of pristine Ti_3C_2 MXene, at a current density of 100 mAg^{-1}. This small size of CoO provided an easy-to-access pathway for electrolyte diffusion and Li+ intercalation by widening the layer gap of Ti_3C_2. Moreover, the Ti_3C_2 prevented the electrode material from crumbling or breaking by acting as a mechanical buffer against the large volume shift. The combined effect of CoO and Ti_3C_2 resulted in improved capacity of CoO/Ti_3C_2 composite compared to pristine Ti_3C_2.

Zhao et al. [167] incorporated the Co_3O_4 nanoparticles with high conductive Ti_3C_2 MXene nanosheet at various ratios of Co_3O_4 and Ti_3C_2. The higher content of Co_3O_4 nanoparticles resulted in lowering the conductivity as well as increasing the probability of agglomeration of nanoparticles on MXene sheet and lower content of Co_3O_4 nanoparitcles leading to restacking of MXene sheet. Hence Co_3O_4/Ti_3C_2 (1:1 ratio) MXene exhibited optimum performance with initial discharge /charge capacities of 2082 and 1326 $mAhg^{-1}$ respectively and maintained a reversible capacity of 1005 $mAhg^{-1}$ after 300 cycles, corresponding to a current density of 1C. However, Co_3O_4/Ti_3C_2 (1:2, 2:1 and 4:1) MXene delivered 678, ~800 and ~600 mAhg-^{1} reversible capacities after 300 cycles at same current density of 1C. Oh and seung. [168] produced nitrogen-doped graphitic C-coated Co_3O_4 nanocrystals on $Ti_3C_2T_x$ MXene nanosheet (termed as Co_3O_4@NGC/MX) as anode for LIB. The Co_3O_4@NGC/MX electrode delivered an initial discharge capacity of 1086 $mAhg^{-1}$, with an initial Coulombic efficiency of 67.6%, and an outstanding cyclic stability with a discharge capacity of 830 $mAhg^{-1}$ after 500 cycles at 1 Ag^{-1}.In addition, this electrode provided superior rate performance with a discharge capacity of 327 $mAhg^{-1}$, at a current density of 50 mAg^{-1}.

Zhang et al. [169] constructed Cu_2O/Ti_2C composite MXene as high performance anode of LIB. The hollow Cu_2O nanoparticles on the surface of conductive Ti_2C MXene created 3D conductive network which resulted in superior electrochemical

performance with the discharge capacities of 790 $mAhg^{-1}$ and 369 $mAhg^{-1}$ corresponding to the coulombic efficiencies of 46% and 102% in the first and 2nd cycle, at a current density of 10 mAg^{-1}. In addition, this MXene provided high rate performances with the capacities of 369, 260, 203 and 145 $mAhg^{-1}$ at the current densities of 10, 100, 500 and 1000 $mAhg^{-1}$ respectively.

Lin et al. [170] generated carbon Nanofiber bridge on the surface of Ti_3C_2 MXene sheet (denoted as Ti_3C_2/CNF) as shown in Fig. 2.23. With the aid of CNF, conductive bridges were created between the top and lower Ti_3C_2 flakes which provided efficient channels for quick electron transport between the flakes and reduced contact resistance between the Ti_3C_2 particles. As anode of LIB, This Ti_3C_2/CNF MXene delivered superior initial discharge and charge capacities of 848 $mAhg^{-1}$ and 407 $mAhg^{-1}$, respectively and a discharge capacity of 320 $mAhg^{-1}$ after 295 cycles, at a rate of 1 C. In addition, at gradually varied rates of 1, 3.5, 8.5 and 30 C, the displayed capacities of this MXene were 320, 180, 145 and 106 $mAhg^{-1}$ respectively. Mashtalir et al. [171] showed that, incorporating carbon nanotubes (CNTs) into the MXene structure raised the specific capacities and rate performances by enhancing ion accessibility to the MXene layers. As anode of LIB, the CNT incorporated Nb_2C MXene electrode supplied excellent initial discharge capacities of 1060, 780, 270 and 160 $mAhg^{-1}$, at the rates of 0.1, 0.5, 10 and 20 C respectively. Furthermore, a capacity of 370 $mAhg^{-1}$ was observed, after 100 cycles, at a rate of 2.5 C. Halim et al. [172] investigated the electrochemical performance of d-Mo_2C/CNT MXene as anode of LIB and showed that, the d-Mo_2C/CNT MXene electrode supplied superior initial discharge capacity of 821 $mAhg^{-1}$ with an initial coulombic efficiency of 76% at a current density of 10 mAg^{-1} and excellent rate capability with a capacity of 250 $mAhg^{-1}$ after 1000 cycles at 5 Ag^{-1}.

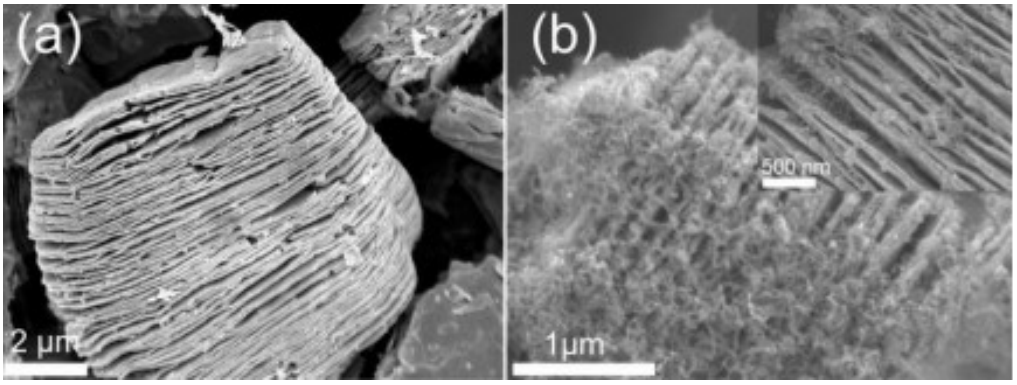

Figure 2.23 (a) SEM images of as-etched $Ti_3C_2T_x$ particles and (b) the Ti_3C_2-CNF [170].

Ren et al. [38] fabricated p-$Ti_3C_2T_x$/CNT MXene by addition of carbon nanotubes with porous $Ti_3C_2T_x$. The combination of CNT and pores of MXene resulted in the enhancement of capacity. As anode of LIB, the p-$Ti_3C_2T_x$/CNT MXene supplied a discharge capacity of 790 $mAhg^{-1}$ in the first cycle and a capacity of ~500 $mAhg^{-1}$, after 100 cycles at a rate of 0.5 C. Moreover, at various rates of 0.1, 10 and 60 C the delivered capacities were 650, 230 and 110 $mAhg^{-1}$ respectively. Cheng et al. [173] investigated the performance of vanadium incorporated $Ti_3C_2T_x$ MXene as anode of LIB. It was observed that, the $V_{0.2}$-$Ti_3C_2T_x$ electrode delivered promising specific capacities of 251.3, 212.0, 183.7, 157.0, and 118.3 $mAhg^{-1}$ in comparison to 180.1, 158.0, 139.3, 128.0, 115.8, and 97.0 $mAhg^{-1}$ of pristine $Ti_3C_2T_x$ MXene at the rate of 0.1, 0.5, 1, 2, and 5 C, respectively.

It is noted that MXenes are attractive choice as anodes for LIBs. However, the performance of MXene-based composite anodes for lithium-ion batteries (LIBs) has been extensively researched in the literature, despite their high capacity anode materials exhibiting cyclability difficulties, such as substantial volumetric contractions and expansions during electrochemical cycling. It is imminent that the wide diversity of composite MXenes offer considerable possibilities for future anode of LIBs which is listed in Table 2.3.

Table 2.3 Summery of cyclic performance of composite MXene as anode of LIBs.

Anode material	**Synthesis Process & (Etchant)**	**Discharge capacity ($mAhg^{-1}$) & Current rate (Ag^{-1})**	**Number of cycle**	**Ref.**
$Ni(OH)_2$/d-Ti_3C_2	Hydrothermal (HCl+LiF)	372 at 1 Ag^{-1}	1000	[108]
NiCo-LDH/Ti_3C_2	Hydrothermal (HCl+LiF)	562 at 5 Ag^{-1}	800	[109]
NiFe-LDH/$Ti_3C_2T_x$	Hydrothermal (HCl+LiF)	726.1 at 1 Ag^{-1}	400	[110]
Ti_3C_2/Si	Orthosilicate hydrolysis & Low temp. reduction (HF)	973 at 1 Ag^{-1}	800	[111]
Si/Ti_3C_2	Electrostatic self-assembly (HCl+LiF)	1654.8 at 1 Ag^{-1}	300	[112]
Si/$Ti_3C_2T_x$	Vacuum filtration (HCl+LiF)	1672 at 1 Ag^{-1}	200	[113]
Porous Si/$Ti_3C_2T_x$-2:1	Vacuum filtration (HCl+LiF)	555.5 at 5 Ag^{-1}	500	[114]
Si-V_2C	Ultrasonic mixing (NaF+HCl)	430 at 3 Ag^{-1}	150	[115]
Mo_2TiC_2–Si-400	Pillaring and calcination (HCl+LiF)	108 at 1 Ag^{-1}	500	[174]
SiO_2/$Ti_3C_2T_x$	Stober method Spray drying (40 wt% HF)	635 at 1 Ag^{-1}	200	[117]
Si-N-$Ti_3C_2T_x$	Heat treatment (40 wt% HF)	760 at 3.2 Ag^{-1}	900	[118]
SiO_x-N-$Ti_3C_2T_x$	Ball millinig &	700 at 1 Ag^{-1}	800	[175]

Anode material	**Synthesis Process & (Etchant)**	**Discharge capacity ($mAhg^{-1}$) & Current rate (Ag^{-1})**	**Number of cycle**	**Ref.**
	Annealing (40 wt% HF)			
d-Si/G/V_2C	48% HF + HCl	2003 at 1C	500	[120]
Fe-$Ti_3C_2T_x$	HCl+LiF	418.8 at 0.2 Ag^{-1}	500	[121]
Fe-Ti_3C_2	HF	310 at 5 Ag^{-1}	850	[122]
(Fe-Ti) oxide/carbon/$Ti_3C_2T_x$	Solvothermal, ultrasound hybridizing & Annealing	452.5 at 10 Ag^{-1}	1200	[123]
N-Ti_3C_2/Fe_2O_3	Thermal decomposition (HCl+LiF)	549 at 2 Ag^{-1}	400	[124]
β-FeOOH/$Ti_3C_2T_x$	(HCl+LiF)	671 at 1 Ag^{-1}	100	[125]
FTCN-Ti_3C_2	Sonochemical method (HCl+LiF)	1034 at 0.1 C	250	[126]
C-TiO_2/Fe_2O_3-Ti_3C_2	Heat treatment	387.7 at 1 Ag^{-1}	1000	[127]
Sn- $Ti_3C_2T_x$	Molten salt reaction method (Lewis acid)	226.2 at 0.2 Ag^{-1}	1000.	[128]
Sn^{4+}/Ti_3C_2	Liquid phase Immersion process (40 wt% HF)	544 at 0.5 Ag^{-1}	200	[129]
V_2CT_x-SnO_2	Ultrasound & Annealing (NH_4F+HCl)	274 at 8 Ag^{-1}	200	[131]
Sn_4P_3-$Ti_3C_2T_x$	Solvothermal phosphorization (50 wt% HF)	847 at 1 Ag^{-1}	300	[132]
SnS/Ti_3C_2Tx	Solvothermal & Annealing	866 at 0.5 Ag^{-1}	300	[84]

Anode material	**Synthesis Process & (Etchant)**	**Discharge capacity ($mAhg^{-1}$) & Current rate (Ag^{-1})**	**Number of cycle**	**Ref.**
	(HF)			
SnS_2/Sn_3S_4- $Ti_3C_2T_x$	Solvothermal & Calcination (45 wt% HF)	101.4 at 5 Ag^{-1}	500	[133]
SnO_2-Ti_2C-C	Hydrothermal	763.18 at 2 Ag^{-1}	500	[134]
Sn/SnO_x-$Ti_3C_2T_x$	Annealing (40 wt% HF)	594.2 at 0.05 Ag^{-1}	200	[135]
5 wt% Ti_3C_2/TiO_2	Hydrolysis (HCl+LiF)	180 at 0.1 C	100	[136]
Ti_3C_2/TiO_2	Hydrothermal (46 wt% HF)	186 at 1 Ag^{-1}	300	[137]
TiO_2/Ti_2C	Oxidation (10 wt% HF)	280 at 1 Ag^{-1}	1000	[138]
Ti_3C_2/TiO_2@f-MoS_2	Hydrothermal & annealing (48 wt% HF)	403 at 2 Ag^{-1}	1200	[139]
Ti_3C_2/LaF_3	Heat treatment (HCl+LiF)	89.2at 1 Ag^{-1}	50	[140]
Ti_3C_2/S		166.3 at 0.5 Ag^{-1}	400	[141]
S-$Ti_3C_2T_x$ (CMC)	Calcination & Annealing (HCl+LiF)	858.2 at 5 Ag^{-1}	3600	[142]
S-$Ti_3C_2T_x$ (PVDF)	Calcination & Annealing (HCl+LiF)	322.2 at 5 Ag^{-1}	3600	[142]
Ti_3C_2/Ag	Self-Reduction (40 wt% HF)	310 at 1 C	800	[143]
3D $Ti_3C_2T_x$/Ag	HCl+LiF	310 at 3 Ag^{-1}	2000	[144]
Li_3VO_4/Ti_3C_2	Sol Gel method	146 at 5 C	1000	[145]

Anode material	**Synthesis Process & (Etchant)**	**Discharge capacity ($mAhg^{-1}$) & Current rate (Ag^{-1})**	**Number of cycle**	**Ref.**
	(48 wt% HF)			
N-Nb_2CT_x	Hydrothermal (50 wt% HF)	238 at 5 C	100	[146]
MgH_2/Ti_3C_2-60	HCl+LiF	328 at 2 Ag^{-1}	50	[147]
GeO_x/Ti_3C_2/PVDF(NMP)	One pot method (HCl+LiF)	483 at 0.2 Ag^{-1}	100	[148]
GeO_x/Ti_3C_2/Li-PAA(DI-water).	One pot method (HCl+LiF)	950 at 0.5 Ag^{-1}	100	[148]
Ti_2C/EMD		490 at 0.1 Ag^{-1}	100	[149]
$Bi_2MoO_6/Ti_3C_2T_x$-30%	Electrostatic self-assembly (HCl+LiF)	545.1 at 1 Ag^{-1}	1000	[150]
Activated carbon-Ti_3C_2	Slurry casting method (HCl+LiF)	881.9 at 0.2 Ag^{-1}	117	[151]
VO_2-NTs/Ti_3C_2	Solvothermal Self assembley (HCl+LiF)	516 at 5 Ag^{-1}	2000	[152]
TiNbC@NTO-500	Hydrothermal (HF)	261 at 1 Ag^{-1}	500	[153]
VNbC@VNO-500	Partial oxidation (40 wt% HF)	323.9 at 1 Ag^{-1}	1000	[154]
$Na_2Ti_3O_7$ / Ti_3C_2	Alkalization & oxidation (HCl+LiF)	158 at 4 Ag^{-1}	1200	[155]
$TiNb_2O_7/Ti_3C_2$	Electrostatic self-assembly (HCl+LiF)	192.3 at 10 C	500	[156]
Ti_3C_2/CoS_2	Hydrothermal (HCl+LiF)	~165 at 1 Ag^{-1}	1000	[158]
MoS_2/Ti_3C_2	Etching	131.6 at 1 Ag^{-1}	200	[159]

Anode material	**Synthesis Process & (Etchant)**	**Discharge capacity ($mAhg^{-1}$) & Current rate (Ag^{-1})**	**Number of cycle**	**Ref.**
	& Solid state sintering (HCl+LiF)			
$MoS_2/Mo_2TiC_2T_x$	Sulfidation	509 at 0.1 Ag^{-1}	100	[160]
Mo_3Se_4-$Ti_3C_2T_x$	Hydrothermal (40 wt% HF)	1092.37 at 0.268 Ag^{-1}	378	[161]
V_4C_3 /MoS_2/C	40 wt% HF	622.6 at 1 Ag^{-1}	450	[162]
T-$Ti_3C_2T_x$@C	HCl+LiF	337.3 at 2C	600	[176]
V_2C@Co	HF	248.8 at 8 Ag^{-1}	15000	[165]
CoO/$Ti_3C_2T_x$	Hydrothermal (40 wt% HF)	324 at 0.1 Ag^{-1}	100	[166]
Co_3O_4/$Ti_3C_2T_x$	HCl+LiF	307 at 5 C	1000	[167]
Co_3O_4@NGC/Ti_3C_2		830 at 1 Ag^{-1}	500	[168]
Cu_2O/Ti_2C	Solvothermal (HCl+LiF)	143 at 1 Ag^{-1}	250	[169]
Ti_3C_2/CNF	CVD	97 at 100 C	2900	[170]
Nb_2C/CNT	CVD	430 at 2.5 C	300	[171]
d-Mo_2C/CNT	vacuum-filtration (HCl+LiF)	76 at 10 Ag^{-1}	1000	[172]
p-$Ti_3C_2T_x$/CNT	Chemical etching method (HF)	~500 at 0.5 C	100	[38]
$V_{0.1}$-$Ti_3C_2T_x$	Microwave irradiation (HF)	72.9 at 3 C	1000	[173]
$V_{0.2}$-$Ti_3C_2T_x$	Microwave irradiation (HF)	92.4 at 3 C	1000	[173]
$V_{0.5}$-$Ti_3C_2T_x$	Microwave irradiation (HF)	98.3 at 3 C	1000	[173]

Chapter 03

MATERIALS AND METHODS

3.1 Background

As discussed in the previous chapter various methods and etchant were used to remove the Al from the precursor MAX phases. Among them, HF and the mixture of HCl and LiF were the most popular. But here NaOH was used to remove the Al from the Ti_2AlC under continuous stirring. A detailed overview of the whole process is shown on the flowchart (Fig. 3.1).

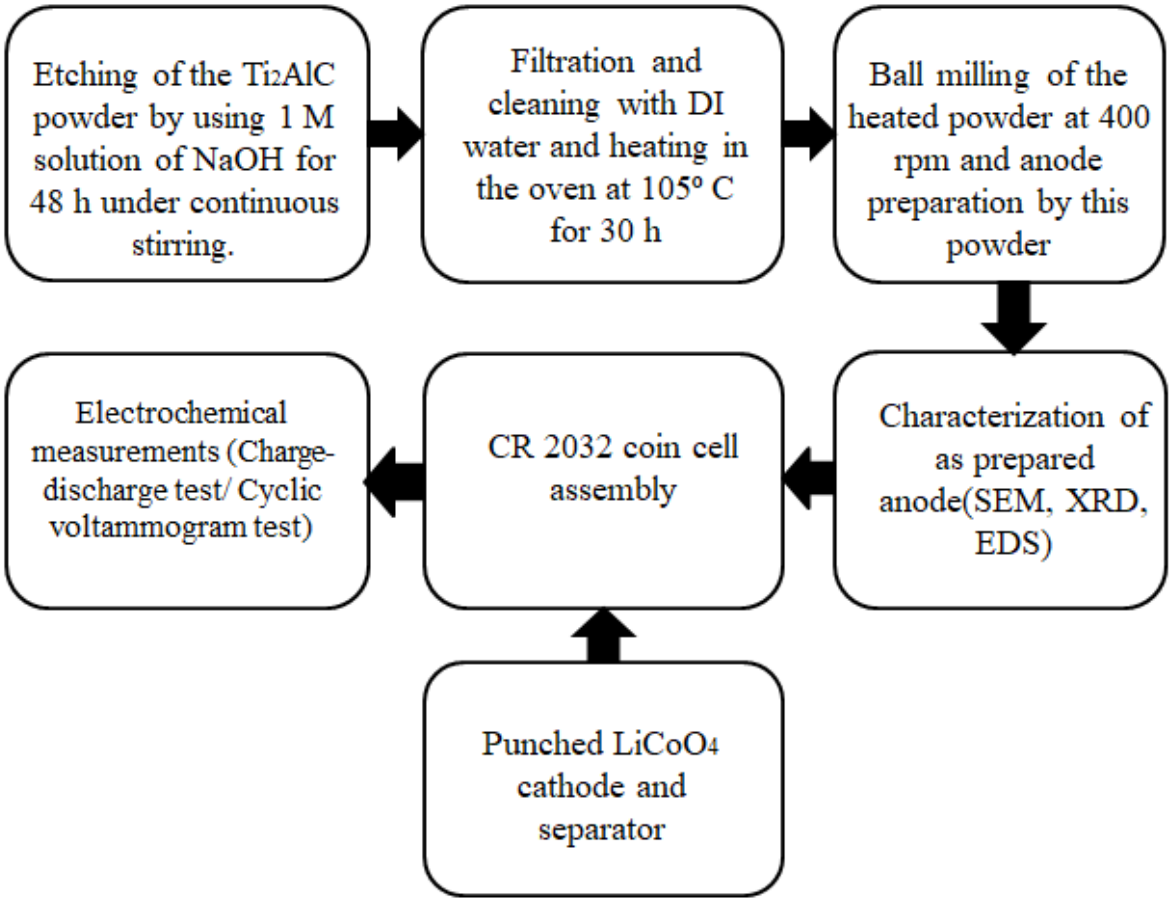

Figure 3.1 Battery fabrication and performance measurement process.

3.2 List of Equipment and Chemicals

The following Table 3.1 provides a summary of the specific details on the materials and substances that will be employed in this study:

Table 3.1 Equipment and chemicals required for the battery fabrication process

Chemical/material name	**Formula**	**Grade**	**Reason**
Lithium Cobalt Oxide	$LiCoO_2$	100%	Cathode material
Battery Electrode Separator	Battery grade PVC	100%	As separator
Ti_2AlC Powder	Ti_2AlC	99.80%	As for the fabrication of anode material
NaOH etchant	NaOH	100%	For etching
Copper foil	Cu	99.99%	As a current collector of the anode
Aluminum foil	Al	Battery Grade	As a current collector of the cathode
Li-Battery grade electrolyte	$LiPF_6$	100%	As electrolyte
Ethanol	C_2H_5OH	100%	Cleaning Agent
Acetone	$(CH_3)_2CO$	100%	Cleaning Agent
Distilled Water	H_2O	100%	Cleaning Agent
Al laminated coin cell case for LIB	For sealing purpose		
Multimeter	To measure voltage and current during charging and discharging process		
Electronic Microbalance	For measuring weight		
Electric Oven	For heating metal powder		
Coin cell case	For assembling battery		

Chemical/material name	Formula	Grade	Reason
Battery tester	For conducting an electrochemical test of the battery		
CV tester	For conducting cyclic voltammogram test of battery		
Hydraulic crimping machine	For sealing the assembled battery		
Magnetic Stirrer	For mixing NaOH		
DC power supply	For regulating DC supply voltage		
Ball Milling Machine	To minimize the size of the particle		

3.2.1 Lithium Cobalt oxide

This battery's cathode was made of lithium cobalt oxide. It was bought from Shandong Gelon Lib Co. Ltd. and coated on aluminum foil on one side. The measured dimensions were 241 mm in length, 200 mm in width, and 55 μm in thickness. From the sheet, A 15 mm diameter circular portion was punched out as indicated in Fig. 3.2 to fit into the coin cell.

Figure 3.2 Lithium cobalt oxide cathode.

3.2.2 Battery Electrode Separator

An essential part of a rechargeable battery is the battery electrode separator, sometimes referred to as a separator. It is placed between the negative and positive electrodes to avoid ions from making direct contact with one another, yet it still permits the flow of ions required for the battery to function. Maintaining electrical isolation between the positive and negative electrodes is the major job of an electrode separator in batteries. Failure to do so could result in short circuits, which pose a risk to public safety and hinder battery performance.

A porous substance with a high ionic conductivity is typically used to make battery electrode separators as shown in Fig. 3.3. To endure the rigors and strains of the battery construction process, they are frequently narrow and mechanically robust. Ceramic membranes, micro porous polymer films, and non-woven textiles are frequent materials used for separators. The characteristics of the PP/PE polypropylene film are discussed below in Table 3.2 which was utilized as a separator in this investigation and was acquired from Xiamen Acey New Energy Technology Ltd., China.

Table 3.2 Characteristics of Separator

Appearance	Ivory White
Thickness	16±2 micron
Gas permeability	350-440 sec/100ml
Porosity	38-44%
Puncturing Strength	>300
Tensile Strength	>90

Figure 3.3 Battery electrode separator.

3.2.3 Ti_2AlC Powder

Ti_2AlC Powder as shown in Fig. 3.4 used as a precursor to make Ti_2C MXene anode was purchased from Luoyang Tongrun Info Technology Co., Ltd., China. The detail specifications of the powder are discussed in Table 3.3.

Table 3.3 Characteristics of Ti_2AlC powder.

Particle Size	325 mesh	
Purity	99%	
Chemical composition result	Ti	72.6%
	Al	18.3%
	C	8.9%
	Density(g/cm^3)	4.2
	Hardness (GPa)	4.2
	Decomposition Temperature (^0C)	1000
	Melting Point (^0C)	2000
	Thermal Conductivity (W/mk)	32-37
	Electrical	3.1×10^6

	Conductivity ($\Omega^{-1}m^{-1}$)	
	Resistivity ($\mu\Omega.m$)	0.35±0.03

Figure 3.4 Ti_2AlC powder.

3.2.4 NaOH etchant

The pellets of Sodium hydroxide were mixed with distilled water to produce a 1M NaOH solution which was used as an etchant to extract the Al from the powder of Ti_2AlC. After the etching process, the obtained Ti_2C MXene surface may had –OH termination groups which provide more stability to the structure. Pure NaOH pellets as shown in Fig. 3.5 were purchased from Taj scientific store.

Figure 3.5 Sodium hydroxide pellets.

3.2.5 Precision electronic balance machine

The weight of 10g Ti_2AlC powder and 4 g of NaOH pellets (to prepare 100 ml of 1M NaOH solution) was measured precisely by using an electronic precision balance machine named SCIENTECH. Fig. 3.6 shows images of the precision electronic balance machine.

Figure 3.6 Image of electric balance

3.2.6 Lithium battery-grade electrolyte

An essential function of a lithium-ion battery's electrolyte was to facilitate ion movement between the two electrodes during charge and discharge cycles. The movement of lithium ions, which regulate the flow of current in batteries, was facilitated by it. A liquid or gel-like material consisting of dissolved lithium salts in an organic solvent commonly used as the electrolyte in lithium-ion batteries.

Lithium perchlorate ($LiClO_4$), lithium trifluorophosphate ($LiPF_6$), and lithium trifluoromethanesulfonate ($LiCF_3SO_3$) are the most frequently utilized lithium salts.

Lithium ions which were required for the electrochemical reactions in the battery were produced when these salts segregate in the solvent. Lithium hexafluro phosphate as shown in Fig. 3.7, or 1M LiPF6, was the electrolyte utilized in this work and was supplied by Xiamen TOB New Energy Technology Ltd. China.

Figure 3.7 Battery electrolyte ($LiPF_6$).

3.2.7 Ethanol

Before every chemical process, all the equipment was cleaned by using ethanol. The ethanol used in this work was 99% pure and bought from Taj Scientific Store as in Fig. 3.8 .

Figure 3.8 Image of ethanol.

3.2.8 Acetone

Acetone was used as a secondary cleaning agent to clean all lab equipment after it was cleaned by ethanol. Acetone used in this work shown in fig. and it purchased from Taj Scientific Store as shown in Fig. 3.9.

Figure 3.9 Image of acetone.

3.2.9 Distilled water

The distilled water as shown in Fig. 3.10 was used to clean Ti_2C MXene after filtration from NaOH solution and it was also used to clean all the lab equipment after the cleaning operation with ethanol and acetone.

Figure 3.10 Image of distilled water.

3.2.10 Electric Oven

A hot box-type electric oven was used in this work to remove the moisture content from the filtered Ti_2C MXene. The manufacturer of this oven is GALLENKAMP as shown in Fig. 3.11.

Figure 3.11 Image of electric oven.

3.2.11 Magnetic Stirrer

A 78-1 model magnetic stirrer was utilized to mix the solution of 1M NaOH and Ti_2AlC during the etching process. Fig. 3.12 shows the model of the magnetic stirrer used in this study.

Figure 3.12 Image of magnetic stirrer.

3.2.12 Coin cell case

In terms of size and form, LIBs come in different varieties, notably D, C, AA, AAA, AAAA, and A23, as well as 9-Volt, CR2032, LR44, CR927, CR1025, CR1216, CR1220, CR1225, and pouch cell batteries. In this specific task, we put together a coin cell battery, model number CR2032. The coin cell is composed of a spacer made of stainless steel, a cover with a plastic ring, a cup (3.2 mm in height and 20 mm in diameter), and a stainless steel spring for tight packing. As seen in Fig. 3.13, the coin cell was imported from Xiamen TOB New Energy Technology Ltd. in China.

Figure 3.13 Image of coin cell case.

3.2.13 Hydraulic crimping machine

A Hydraulic crimping machine was used to seal the CR2032 coin cell. It changed the sealing line without affecting the die. Moreover, it could be applied to disassembly procedures by replacing the original die. Fig. 3.14 depicted the hydraulic crimping machine.

Figure 3.14 Image of a hydraulic crimping machine.

3.2.14 Battery tester

A battery tester as shown in Fig. 3.15 was employed to look at the battery's electrochemical capabilities. A battery cycler assesses the battery's performance by tracking the cells' actions throughout charge and discharge cycles. Many variables, including capacity, battery efficiency, and self-discharge, can be assessed during battery cycling. The test was conducted utilizing a multichannel LANHE LAND-CT2001A battery testing equipment in the voltage range of 0.02 to 3.00 V.

Figure 3.15 Image of battery tester.

3.2.15 CV and EIS tester

A CORRTEST CS100 device was used to test the cyclic voltammogram and EIS of the coin cell as shown in Fig 3.16.

Figure 3.16 Image of CV and EIs tester.

3.2.16 Multimeter

An ammeter, voltage tester, or ohmmeter can all be read with a multimeter, which is a multifunctional electrical tool. There are indicator needles for positive and negative values on a numeric LCD digital display. Using multimeters, one may test batteries, power sources, and electric motors. We used a multimeter to measure the open circuit voltage of the manufactured battery for our investigation (Fig. 3.17).

Figure 3.17 Image of a multimeter.

3.2.17 SEM machine

A scanning electron microscope used to investigate the morphology of as synthesized Ti_2C MXene and Ti_2AlC precursor.

3.2.18 XRD machine

The X-ray diffraction patterns of the Ti_2C MXene samples were observed by using Cu Kα as the radiation source (Empyrean, PANalytical-Netherlands). The diffraction patterns were recorded over a 2θ range from 10 to 90 at a step size of 0.10.

3.3 Etching

To separate the Al atom from Ti_2AlC Max phase etching process was carried out. Initially, 4 g of NaOH pellets were added to the 100 ml of distilled water to prepare 1 M of NaOH solution then 10 g of Ti_2AlC powder (~ 325 meshes) were gradually added to this solution. The solution was kept under continuous stirring for 48 h. To fully etch Al from Ti_2AlC another 4 g of NaOH pellets were added to the solution after 1st 24 hr as shown in Fig. 3.18.

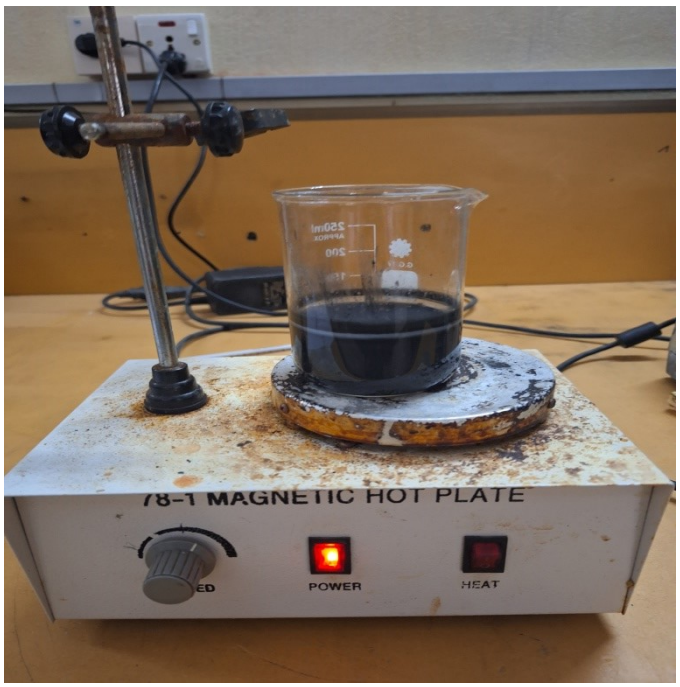

Figure 3.18 Etching process under stirring.

3.4 Filtration, Heating, and Ball milling

After completion of the etching process filtration was carried out to separate the residue from the solution and cleaned the separated residue by using distilled water several times as shown in Fig. 3.19.

Figure 3.19 Filtration process of Ti_2C MXene.

The moisture content present in the separated Ti_2C MXene was completely eliminated by heating up these powders in an oven at 105^0C for 30 hr.

Then the heated Ti_2C powders were ball milled for 4 hr at 400 rpm to minimize the particle size as shown in Fig. 3.20.

Figure 3.20 Ball milling process.

3.5 Characterization

The term "material characterization" describes the procedures or techniques used to quantify and identify a material's mechanical, chemical, physical, and microstructural characteristics. The as-synthesized samples were characterized at the BUET material laboratory in Dhaka. The morphology and structure of the Ti_2C MXene sample were examined using a high-resolution scanning electron microscope (SEM; JSM 7600F, JEOL-Japan). The crystal structure and composition of the sample were ascertained using an Energy Dispersive X-ray (EDX) and an X-ray diffractometer (XRD) (Empyrean, PANalytical-Netherlands) using radiation from the copper target (k, =0.15406 nm). The approach used in this thesis is described in the parts that follow.

3.5.1 X-ray diffraction (XRD)

One effective analytical method for examining the structure of crystalline materials is X-ray diffraction (XRD). Its foundation is the idea that atoms in a crystal lattice scatter X-rays, producing a characteristic diffraction pattern that reveals details about the atoms' arrangement inside the material. The XRD method can be used to determine if a material is amorphous or crystalline. With this adaptable, nondestructive method, exact details regarding a material's physical attributes, chemical makeup, and crystal structure can be obtained.

An X-ray source with Cu K radiation (= 1.5406) is used to perform the XRD analysis. Electromagnetic waves having a wavelength of only one and a size similar to atoms are called X-rays. The X-ray beam is made up of numerous distinct waves that may intersect and cause interference with one another. Interference is produced when X-ray beams and atoms in crystals interact. The interference is particular to the crystal structure and happens at an angle to the atomic planes. Fig. 3.21 shows how interference occurs by Bragg's law.

The formula for Bragg's law is $n\lambda = 2d\sin\theta$, wherein n is an integer, θ is the angle between the incoming X-ray beam and the scattering plane, d is the atomic layer separation, and λ is the X-ray wavelength.

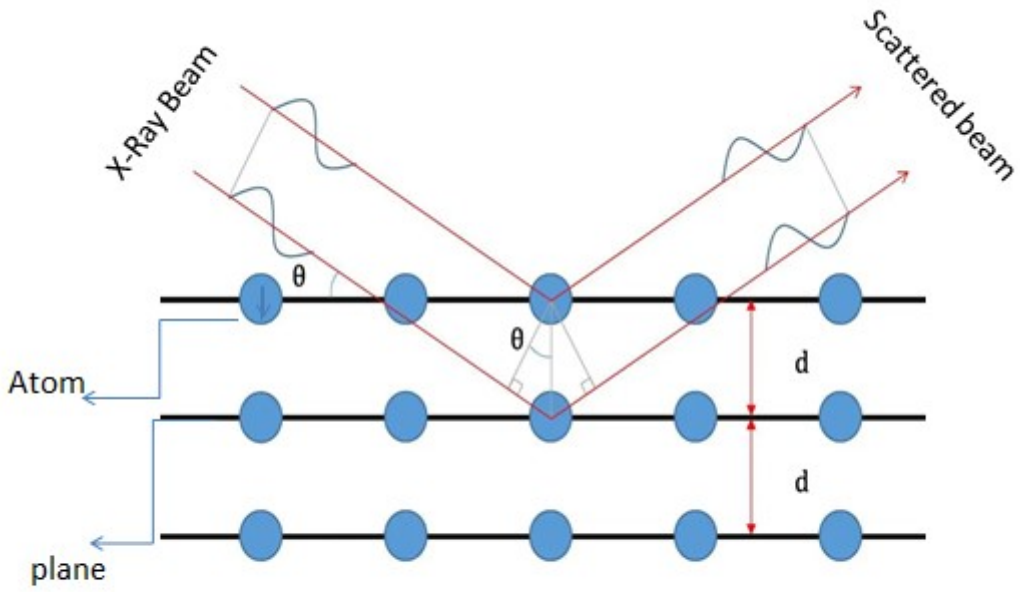

Figure 3.21 Schematic of Braggs law.

Acute interference maxima, or peaks, with the same symmetry as the atom distribution make up the scattered waves in crystals when the atoms are arranged in a regular sequence. Moreover, information about the structural properties of the crystals may be obtained from the diffraction peaks. The equation $D= 0.94\ \lambda / (\beta \cos\theta)$, where λ is the X-ray wavelength, β is the full width at half maximum of a reflation located at 2θ, and D is the average crystallite dimension, is commonly used to quantify the crystallite size of polycrystalline material..

3.5.2 Scanning electron microscopy (SEM)

Scanning electron microscopy (SEM) is a high magnification imaging method that is used to evaluate the surface shape and composition of a material. In-depth three-

dimensional details regarding the topography and structure of the sample are given. A beam of extremely intense electrons is produced in SEM by an electron source, which is usually a field emission cannon or tungsten filament. Electromagnetic lenses are used to direct the electron beam onto the sample, just as light is focused in an optical microscope. Fig. 3.22 shows the SEM working diagram.

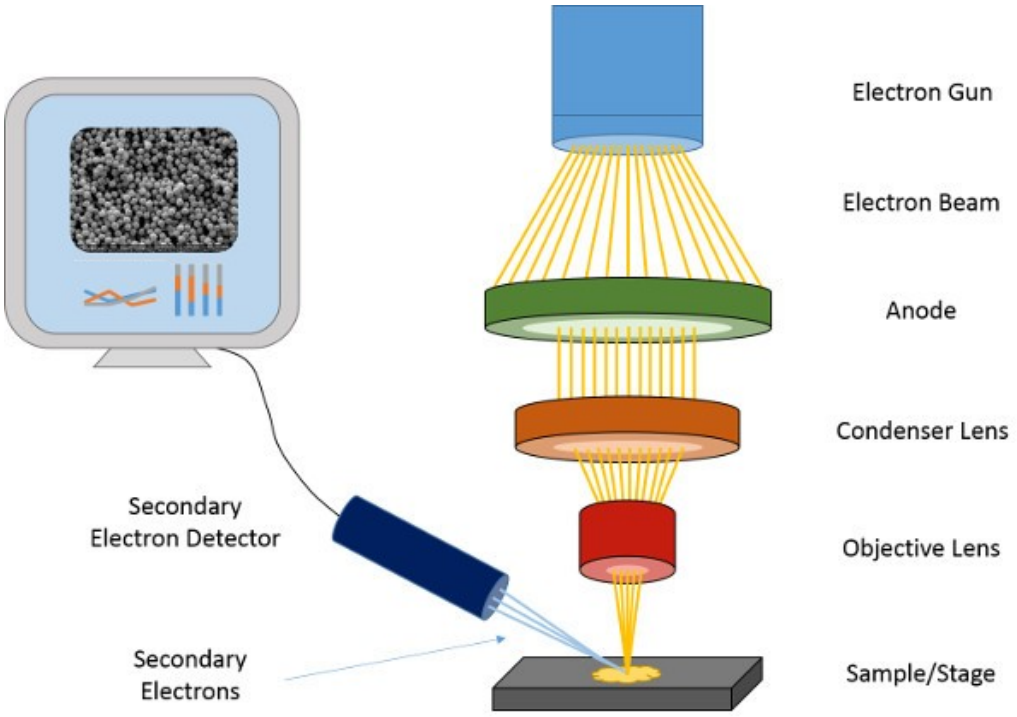

Figure 3.22 Schematic diagram of SEM working.

3.5.3 Energy-Dispersive X-ray Spectroscopy (EDX)

Finding a material's elemental composition can be done by an analysis process called energy-dispersive X-ray spectroscopy (EDX), sometimes known as energy dispersive X-ray analysis (EDX or EDXA). It frequently works in tandem with transmission and scanning electron microscopy techniques in electron microscopy research. The unique X-rays produced by EDX are created by the sample interacting with an electron beam. As high-energy electrons from the electron beam of the microscope impact the atoms in the sample, inner-shell electrons are activated or driven off of their orbits. The voids left by the displaced electrons are then filled with outer-shell electrons, releasing the energy as X-rays. Different energies in the emitted X-rays

correspond to the elements present in the sample. In an EDX system, the main component is an X-ray detector, which is typically a solid-state semiconductor detector. It recognizes these characteristic X-rays and measures their energy. After the observed X-rays are converted into electrical signals, their energy is measured using a spectrometer. By measuring the X-ray intensity at different energies, the spectrometer generates an energy-dispersive X-ray spectrum. The spectrum displays peaks at certain energies that correspond to the different X-rays that the different elements in the sample release. By comparing the observed X-ray energy to the known typical X-ray energies of the constituent elements, the composition of the sample can be determined. The intensity of the X-ray peaks indicates the relative abundance of the elements.

3.6 Anode Preparation

After characterization of the ball-milled Ti_2C MXene powder, the anode was prepared by mixing this powder with PVDF and NMP binder as shown in Fig. 3.23.

- A 3g mixer of Ti_2C MXene and PVDF was prepared where 2.4 g was Ti_2C and 0.6 g was PVDF powder.
- Added a sufficient amount of NMP binder to make the mixer paste-like.
- The paste was coated over the Cu foil and heated in the oven at 80 ^{0}C for 24 hr.
- A 15 mm in diameter was punched out to use as a coin cell anode.

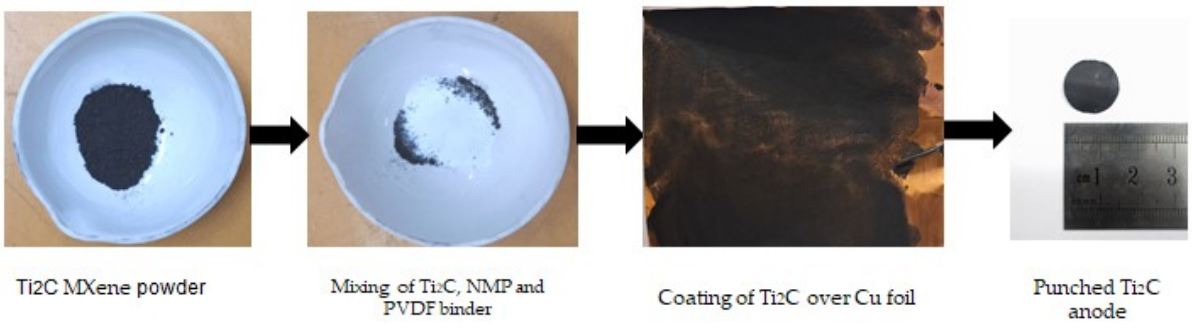

Figure 3.23 Anode preparation process.

3.7 Coin Cell assembly

An as-prepared anode and a 15 mm LiCoO2 disc were initially punched out of the strip. To prevent short circuits, the separator was punched slightly bigger (18 mm) than the electrodes. The CR2032 coin cell was put together in this work according to the order indicated in Figure 3.30. The CR2032 coin cell's positive shell was first connected to the anode, and then a plastic dropper was used to administer an electrolyte drop. After that, the separator was installed and moistened with an electrolyte drop. The spacer, wave spring, and negative coin cell enclosure were then gradually placed on top of the punched LiCoO2 cathode, as seen in Fig. 3.24. At last, a hydraulic battery crimper was used to crimp the coin cell.

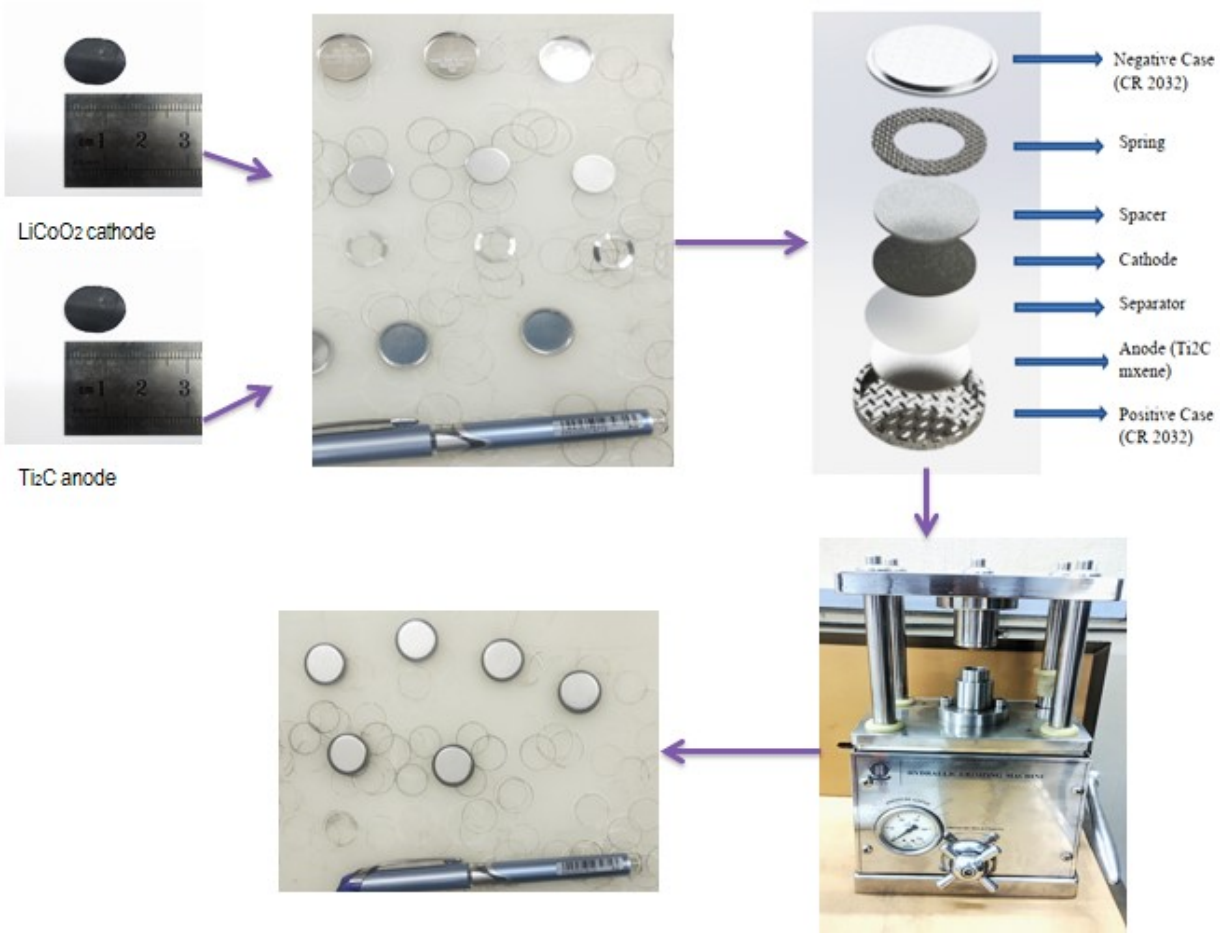

Figure 3.24 CR2032 coin cell preparation process.

3.8 Electrochemical Measurement

After crimping the coin cell the galvanostatic charge/discharge tests were carried out by using a LAND-CT2001A battery testing system in a voltage range between 0.02 and 3 V at various current rates. In addition, cyclic voltammogram and EIS analysis were performed in CORRTEST CS 100 at various scan rates between 100 to 1 m.

Chapter 04

RESULT AND DISCUSSION

4.1 Background

Energy storage and consumption efficiency, sustainability, and innovation have all been fueled by lithium-ion batteries, which have transformed many sectors and facets of everyday life. The majority of portable electronics run on it, and it also provides the high energy density required for electric cars to go far between charges, making them a competitive alternative to gasoline-powered vehicles. Additionally, it stores energy generated by renewable energy sources, especially wind and solar power and is increasingly being used for grid energy storage to assist utilities in managing demand and supply fluctuations, enhancing grid stability, and introducing additional renewable energy sources to the grid. It also helps reduce greenhouse gas emissions and dependency on fossil fuels. In addition to all of these benefits and applications, LIBs had low power and energy density as well as capacity fading problems during cycling. Several anode materials were investigated to create a high-performance lithium-ion battery to solve the aforementioned issues. Ti_2C MXene materials have several unique properties that make them interesting candidates for anode materials in lithium-ion batteries (LIBs). These properties include high electrical conductivity, a large specific surface area that can accommodate a high number of lithium ions in their layered structures, and good structural stability over cycles of lithium insertion and extraction. In this chapter, the electrochemical performance of Ti_2C MXene will be discussed along with its structural morphology.

4.2 XRD Analysis

The XRD pattern of Ti_2AlC powder before and after etching shown in Fig. 4.1. To synthesize Ti_2C MXene, Ti_2AlC was utilized as a precursor which resulted in the presence of some residual Ti_2AlC in the finished sample.

The XRD pattern of the precursor before etching shown at the bottom of the figure where the peaks at the angle of $2\theta = 13.01^0$, 36.07^0, 39.60^0, 41.88^0, 52.95^0, 71.59^0 were representing the characteristics peaks of Ti_2AlC powder[177].

After etching the Ti_2AlC powder by NaOH, the peaks at 13.01 vanished and a significant peak was observed at $2\theta = 7.25^0$ at the plane of (002), which was the characteristic peak of Ti_2C MXene[178]. In addition, nearly every peak was identified at the angle of $2\theta = 36.07^0$, 39.60^0, 41.88^0, and 52.95^0 which were also present in the XRD pattern before etching representing the presence of Ti_2AlC powder also noted in the XRD pattern after etching attributed to the partial etching of Ti_2AlC powder. Due to the lower concentration of NaOH during etching, the Al was not fully etched out and Ti_2AlC powder was present in the sample after etching.

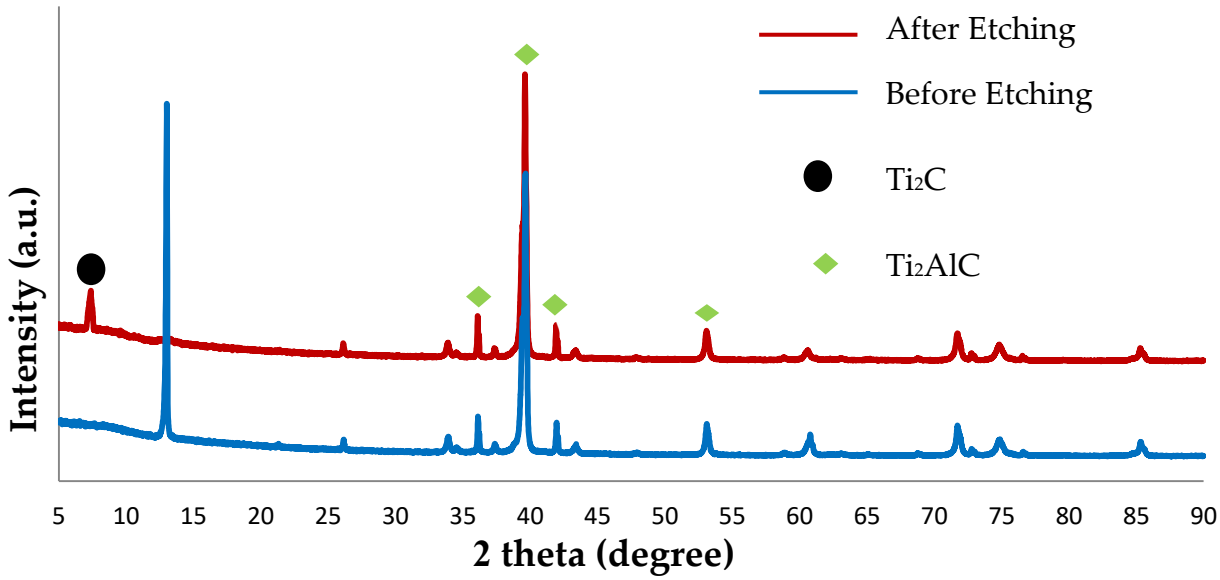

Figure 4.1 XRD pattern of Ti_2AlC precursor before and after etching.

4.3 SEM and EDX analysis

SEM analysis was performed to investigate the surface morphology of Ti_2AlC powder before and after etching. Fig. 4.2 (a) and (b) depicts the structure of Ti_2AlC powder before etching at lower and higher magnification. In low magnification image, large, flat and hexagonal or rectangular platelike structures were observed. These platelets varied in size and often appeared as larger aggregates or clusters. In high magnification image, the well-defined edges and corners as well as minor surface roughness and layered nature of the platelets were observed more clearly and showing how they stack or align in the material. Fig. 4.2 (c) and (d) displayed the low and high magnification image a Ti_2AlC powder after etching. variety of irregularly shaped and sized platelets and pebbles were seen. The materials appearance was uneven and less structured or aggregated indicating the incomplete etching of Ti_2AlC attributed to the low concentration of NaOH during etching.

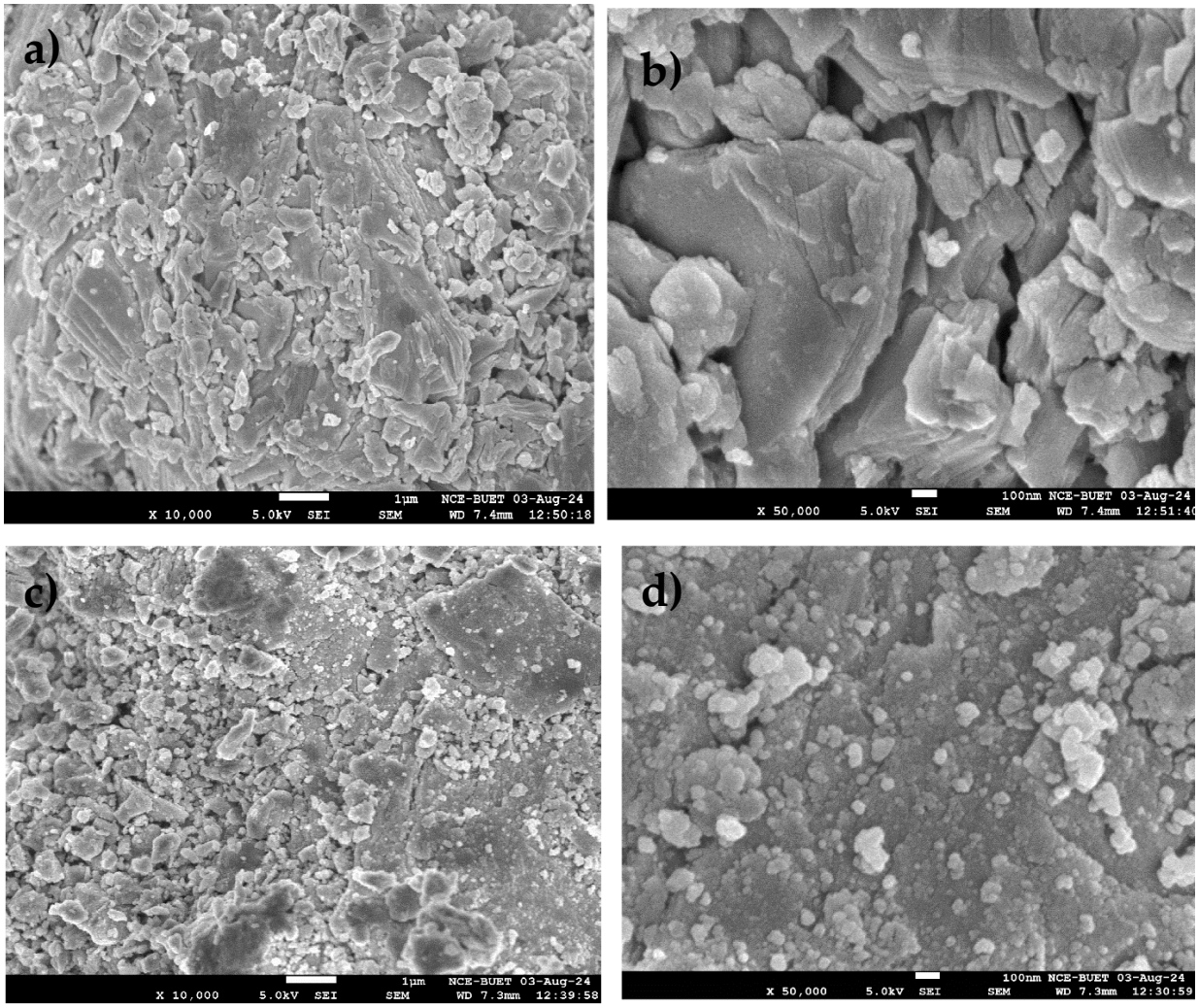

Figure 4.2 a) Low Magnification b) High magnification image of precursor before etching and c) Low Magnification d) High magnification image after etching.

EDX analysis was performed to reveal the mass fraction of Ti_2AlC before and after etching. Fig. 4.3 (b) and (d) depicted that the mass fraction of Al was reduced from 11.19% to 7.57% due to the etching of Ti_2AlC by using NaOH. The presence of Al after etching means that, the Ti_2AlC powder were partially etched attributed to the using lower concentration of NaOH during etching.

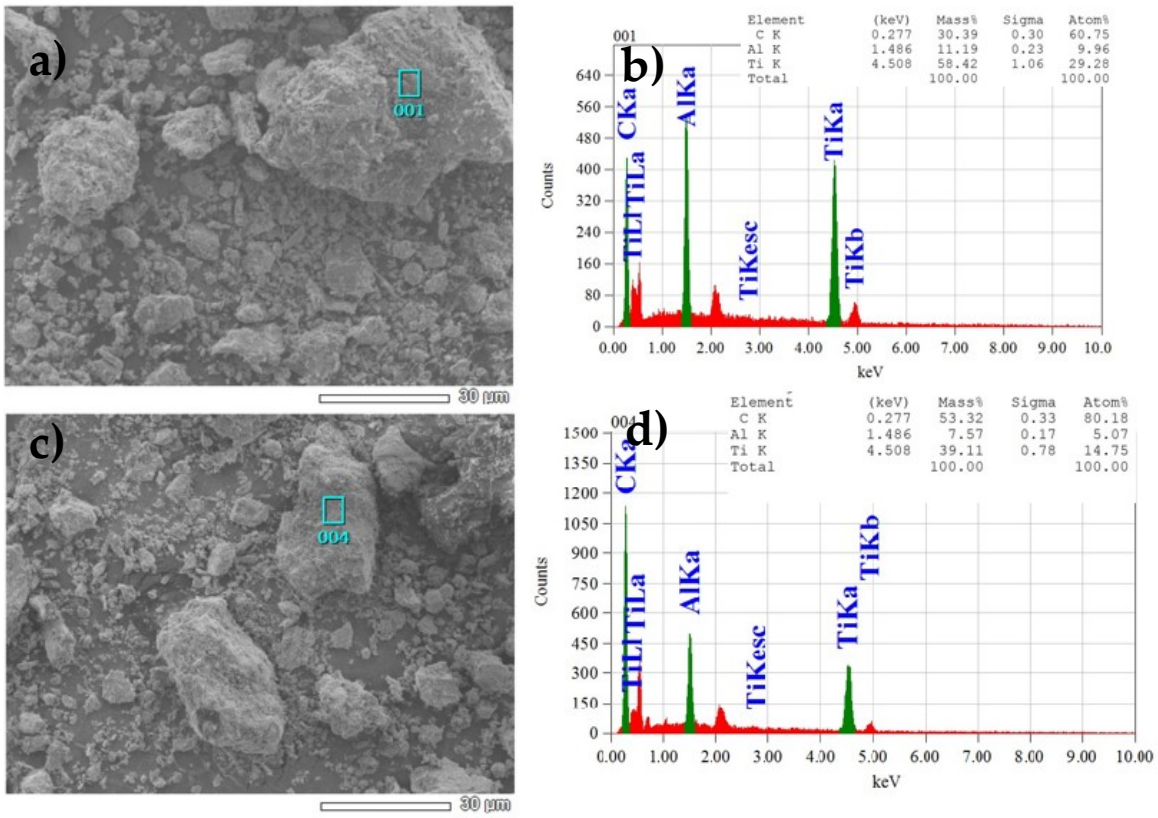

Figure 4.3 EDX analysis of Precursor before etching (a,b) after etching (c,d)

Fig. 4.4 (a) and (b) depicted the low and high magnification SEM image analysis of anode material. In low magnification image, the surface was smooth with minor porosity and at high magnification image, much irregular surface along with lots of cavities were seen. Fig. 4.4 (c) and (d) displayed the EDX analysis of mass percentage of anode material at (003) location. The percentage were C= 45.35%, F= 52.39%, Al=0.16% and Ti=1.75%.

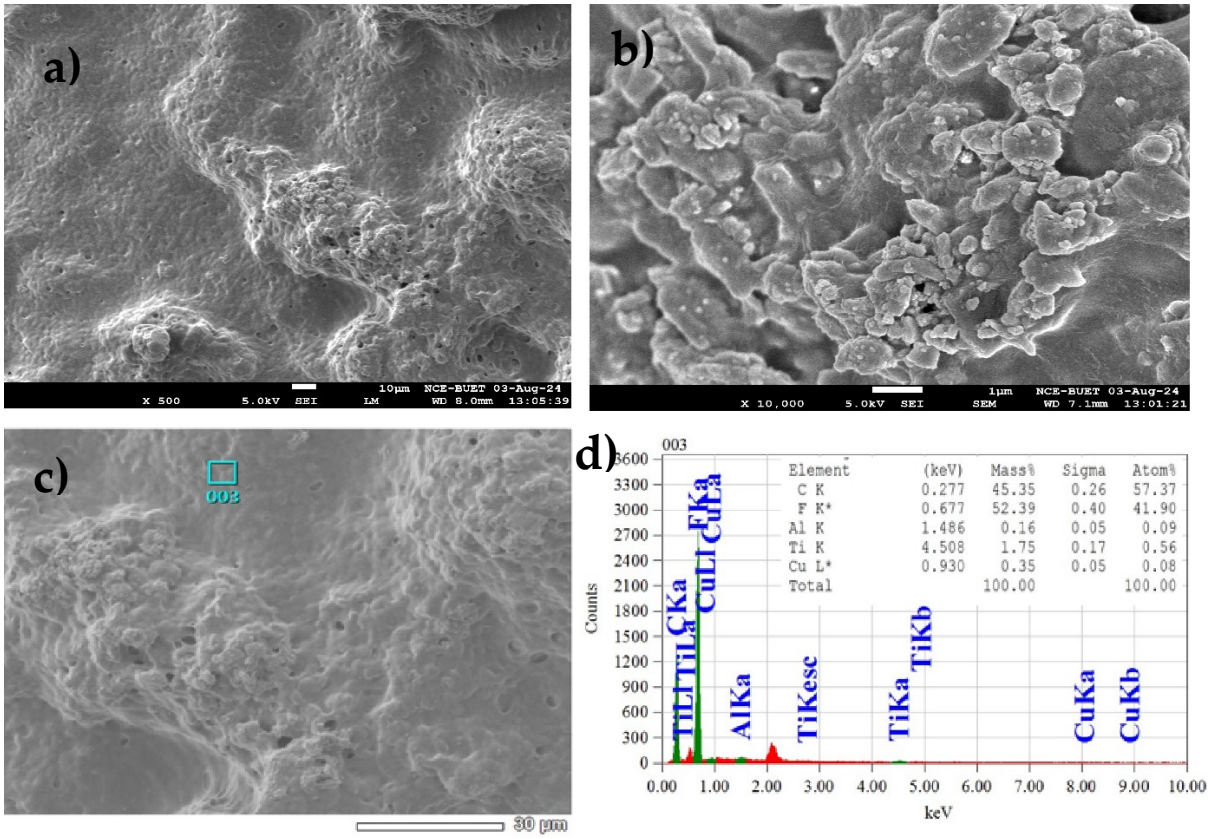

Figure 4.4 a) Low Magnification b) High Magnification image of anode (c,d) EDX analysis of anode.

4.4 Electrochemical analysis

The variation of voltage and current along with time over (a) 1-20 and (b) 21-40 galvanostatic Charge-Discharge cycles shown in Fig. 4.5 and Fig. 4.6.

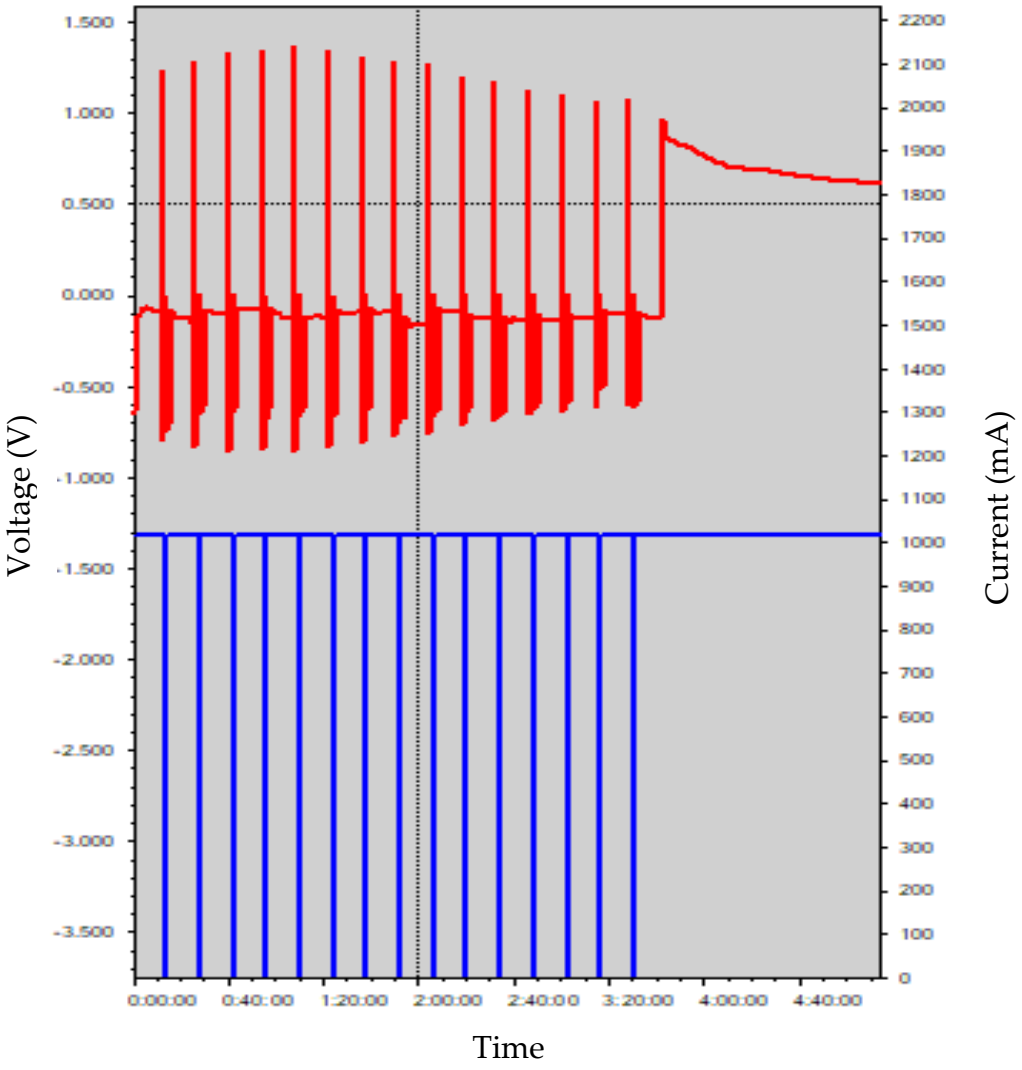

Figure 4.5 Change of Current and Voltage with respect to Time for 1-20 Charge-Discharge cycles.

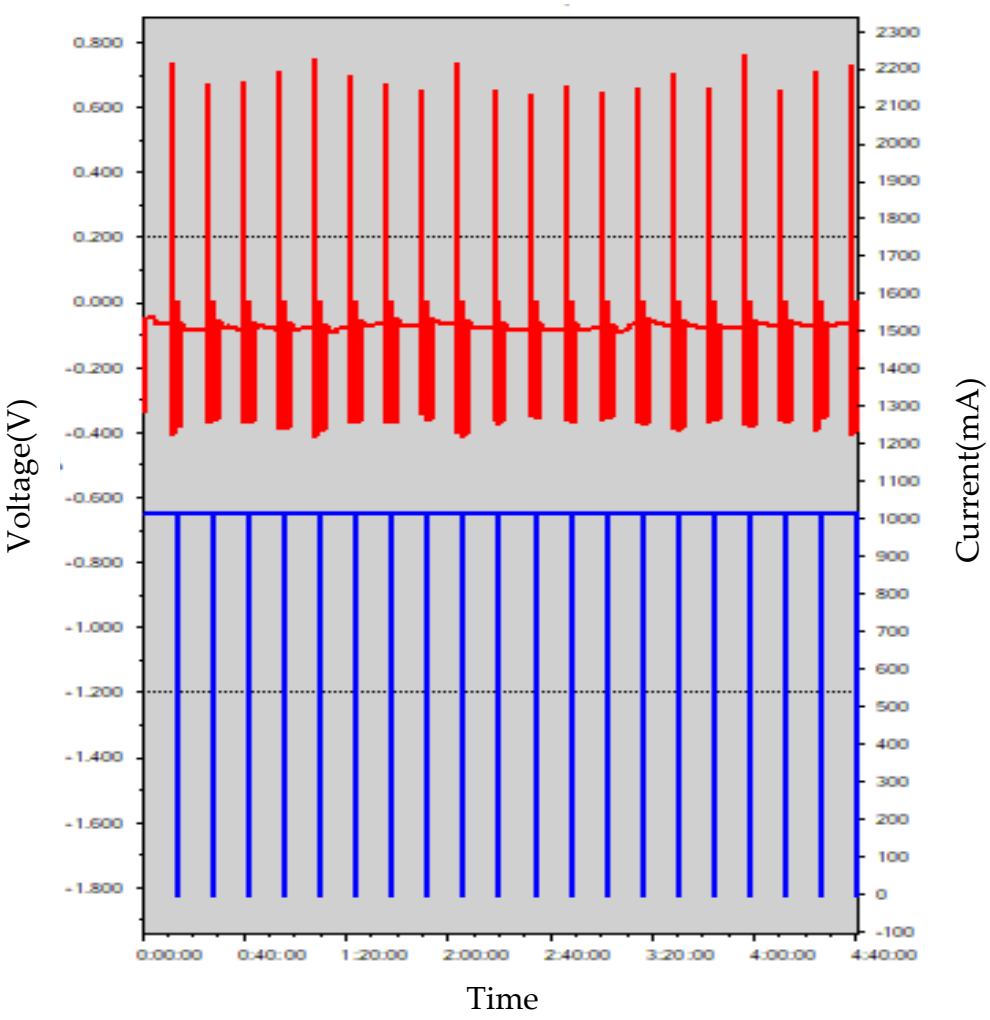

Figure 4.6 Change of Current and Voltage with respect to Time for 21-40 Charge-Discharge cycles.

The cutoff voltage was varying in the range of 0.3-1.3V. Initially, the voltage was 1.250 V. However, with the battery cycling the voltage drops drastically and at the end of the 100th cycle, the measured voltage was observed 0.407V.

The galvanostatic charge-discharge cycle was conducted to determine the electrochemical performance of the as-prepared Ti_2C MXene anode. Fig. 4.7 depicts the variation of capacity for 1-20 charge-discharge cycles at a current density of 50 mAg^{-1}.

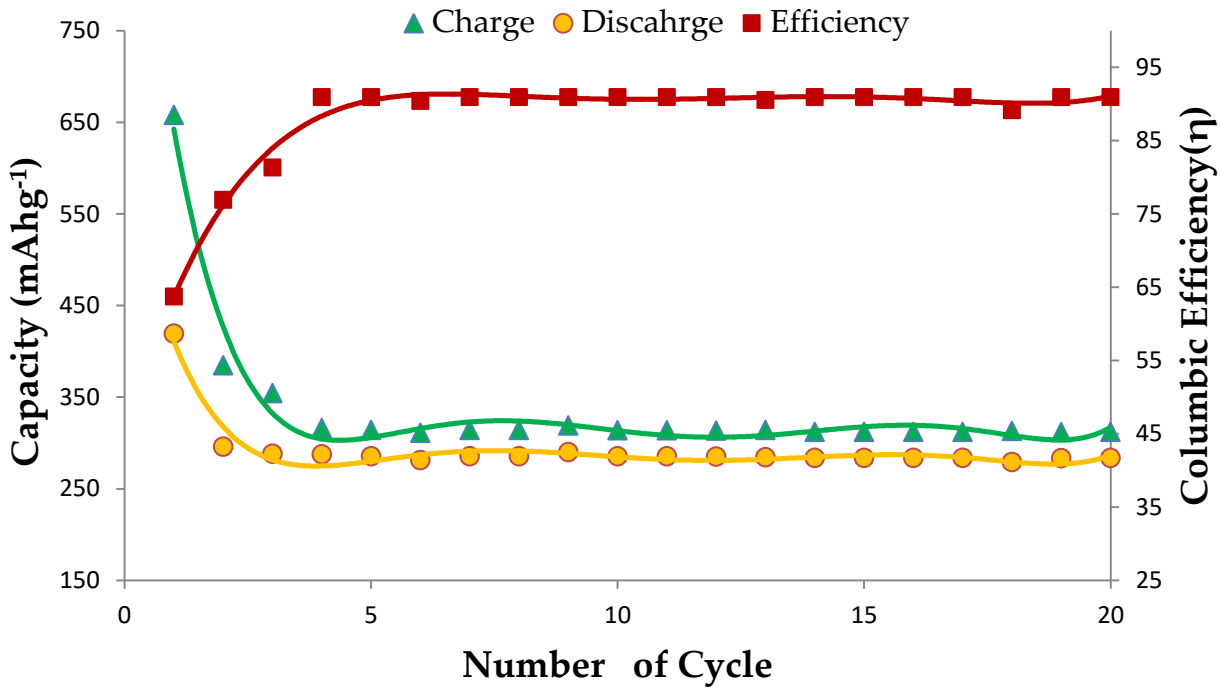

Figure 4.7 Cycling performance of Ti_2C MXene at 50 mAg^{-1}.

The first cycle Charge and discharge capacities were found to be 658.02 $mAhg^{-1}$ and 419.11 $mAhg^{-1}$ respectively with an initial columbic efficiency of 63.6%. The huge irreversible capacity loss in the first cycle could be attributed to the formation of SEI film on the electrode surface along with the irreversible reduction of electrochemically active surface groups such as –OH in this case [76]. However, in the subsequent 2nd cycle the charge-discharge capacity drastically reduced to 384.50 $mAhg^{-1}$ and 295.77 $mAhg^{-1}$ and the columbic efficiency increased sharply and stabilized within the range of 90%-92% after the third cycle. After 20 cycles, the Ti_2C MXene maintained a capacity of 283.7 $mAhg^{-1}$ corresponding to an efficiency of 90.9%. This stable capacity could be ascribed to the formation of stable SEI layer and the intercalation of Li^+ ion in the interlayer space between the Ti_2C sheets [23].

The rate performance of Ti_2C MXene was tested at different current densities as shown in Fig. 4.8. The capacities were decreased from 419.11 $mAhg^{-1}$ to 263.2 $mAhg^{-1}$, to 237.3 $mAhg^{-1}$ and to 203.7 $mAhg^{-1}$ as the current density increased from 50 mAg^{-1} to 100 mAg^{-1}, to 150 mAg^{-1} and 200 mAg^{-1}. When the current density again reduced to 50 mAg^{-1} excellent capacity retention with the capacity of 265.3 $mAhg^{-1}$ was observed.

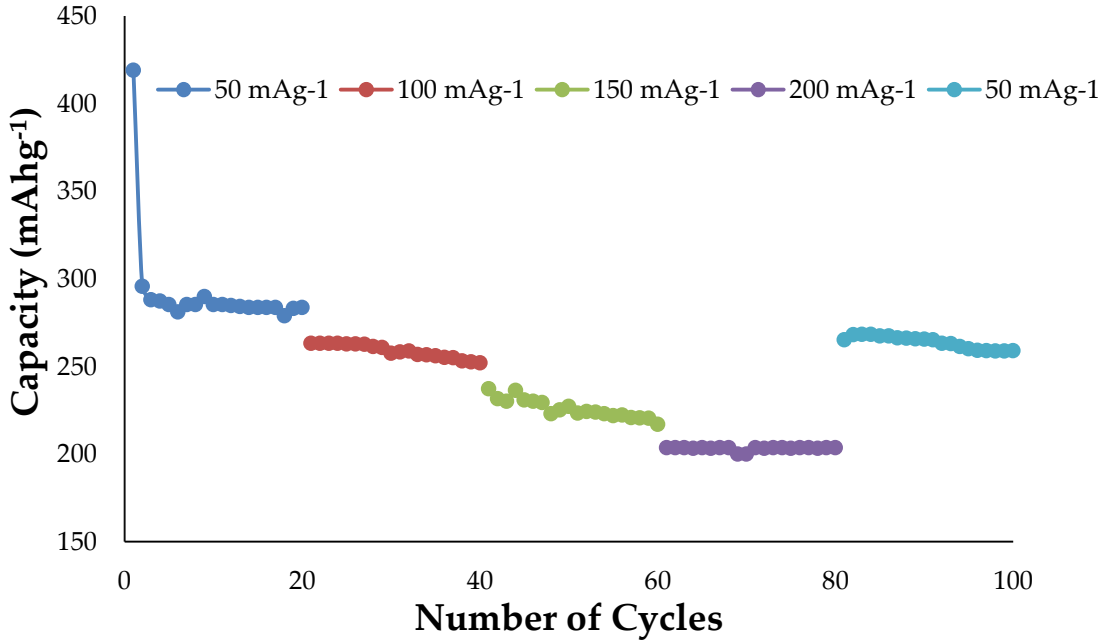

Figure 4.8 Cycling performance of Ti_2C MXene at different current densities.

Table 4.1 displays the comparison of the performance of as prepared Ti_2C MXene anode with other conventional anode materials.

Table 4.1 Comparison of Cycling performance of various anode material

Materials	**Synthesis Process**	**Discharge Capacity after n^{th} Cycle**	**Ref.**
Ti_2C	NaOH etching	259.1$mAhg^{-1}$ after 100 cycles at 50 mAg^{-1}	In this work
Ti_2C	HF etching	80 $mAhg^{-1}$ after 120 cycles at 3 C.	[179]

Materials	**Synthesis Process**	**Discharge Capacity after n^{th} Cycle**	**Ref.**
Ti_3C_2	HF etching	118.7 $mAhg^{-1}$ after 75 cycles at 1 C.	[180]
CNT/GP	CVD	290 $mAhg^{-1}$ after 40 cycles at 30 mAg^{-1}	[181]
Porous Graphite	Thermal Oxidation	175 $mAhg^{-1}$ after 100 cycles at 2.5 C	[182]
Anatyse TiO_2	Hydrolysis	148 $mAhg^{-1}$ after 40 cycles at 50 mAg^{-1}	[183]
Porous SnO_2	Spray pyrolysis	410 $mAhg^{-1}$ after 50 cycles.	[184]
MnO/C	Hydrothermal	618.3 $mAhg^{-1}$ after 200 cycles at 0.66 C	[185]
NiO/Ni	Thermal Oxidation	25 $mAhg^{-1}$ after 30 cycles at 1 C.	[186]

The high-rate performance along with cyclic stability with respect to other electrodes was facilitated by the wide surface area of the layered Ti_2C MXene structure, which also allows more lithium-ion deposition over the surface and allows more electrolytes to come in contact with the anode. The outstanding stability of Ti_2C MXene up to 100 cycles could be attributed to the lower volume change during lithium insertion and de-insertion.

The cyclic voltammetry curve for the first cycle charge-discharge at a scan rate of 0.2 mVs^{-1} shown in Fig. 4.9. Two broad reduction peaks were observed at 0.57 V and 1.25 V respectively, corresponding to the formation of SEI layer and reduction reaction. However, three broad oxidation peaks were observed in the oxidation process. The first, at 1.7 V was due to the oxidation reaction while the second at 1 V was due to the oxidation of Al and third was at 0.6 V due to the partial decomposition of the SEI layer [23,138] .

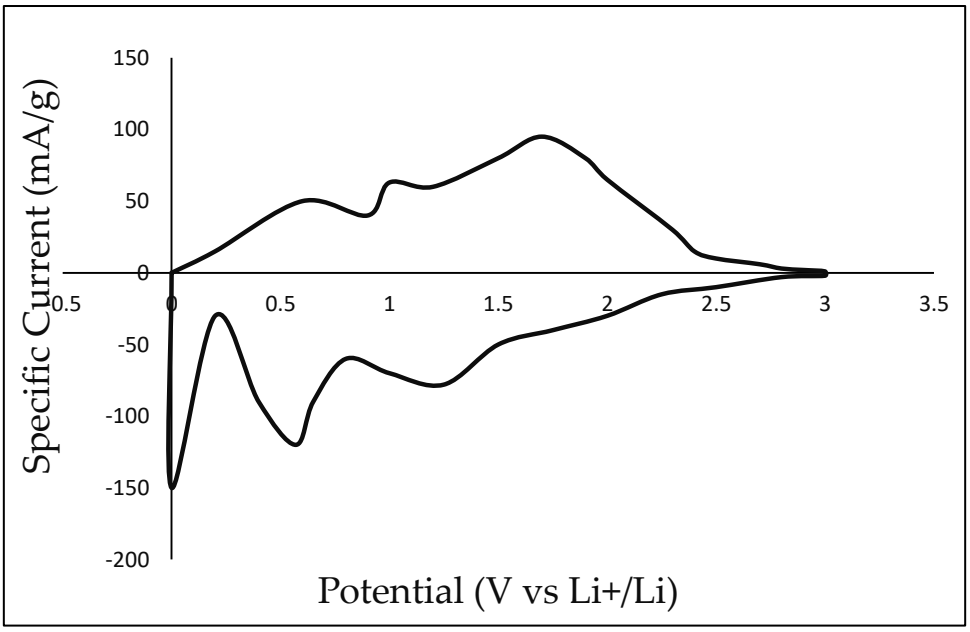

Figure 4.9 CV curves at 0.2 mVs^{-1}.

Throughout this chapter the morphology of as prepared anode and the electrochemical performance of as prepared lithium ion battery were investigated. To compare the performance of as prepared Ti_2C MXene anode with conventional graphite anode and TiO_2 anode, it was found that the theoretical capacity of TiO_2, Ti_2C and graphite were 336 $mAhg^{-1}$, 331 $mAhg^{-1}$ and 372 $mAhg^{-1}$ respectively as shown in Fig. 4.10. However, after 100 cycles the capacity delivered by TiO_2 and graphite were almost 210 $mAhg^{-1}$ and 230 $mAhg^{-1}$ respectively whereas the capacity shown by Ti_2C MXene was 259.1 $mAhg^{-1}$ at a higher density. That means, if pure

Ti_2C MXene can be prepared by completely etching Al from the precursor, this MXene could be a good replacement of conventional graphite anode.

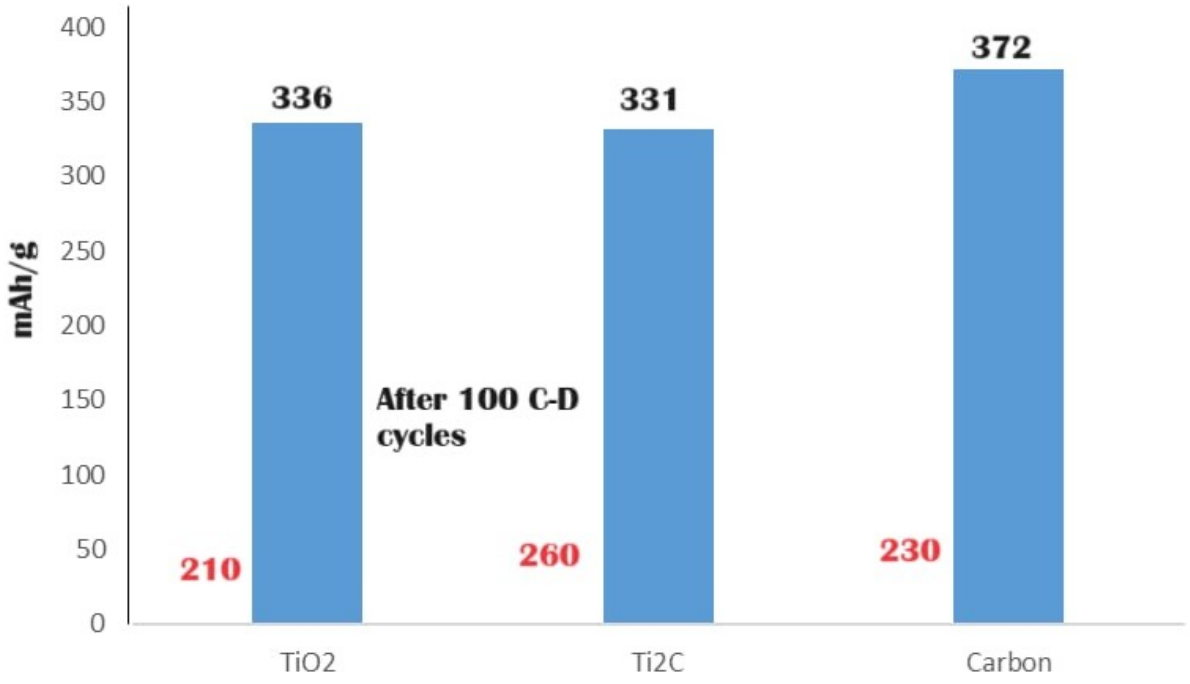

Figure 4.10 Comparison with different anode materials.

4.5 Summery

In this chapter, NaOH etched Ti_2C Mxene was used as anode material for lithium-ion Batteries. The surface morphology and electrochemical performance of as prepared anode were evaluated. The observed first cycle charge-discharge capacities were found 658.02 $mAhg^{-1}$ and 419.11 $mAhg^{-1}$ respectively with an initial columbic efficiency of 63.6% and excellent capacity retention of 259.1 $mAhg^{-1}$ obtained after 100 cycles at a current density of 50 mAg^{-1}. Outstanding rate performance was also observed when the current density increased from 50 to 200 mAg^{-1} the capacities varied from 419.11 $mAhg^{-1}$ to 203.7 $mAhg^{-1}$ respectively. The excellent cyclic performance and stability of this cell are attributed to the unique properties of MXene structure such as high electronic conductivity, low operating voltage, large surface area, and fast Li ion diffusion characteristics.

Chapter 05

Conclusion and Future Study

5.1 Conclusions

In this study, Ti_2C MXene was synthesized by selectively etching Al from the Ti_2AlC MAX phase. The etching process was carried out by using NaOH solution at room temperature with continuous stirring then the samples were ball milled to make it nanostructured. After that, the characterization was carried out to check the synthesis output. The findings of characterization and the performance of the as-prepared electrode include the following:

- From the XRD pattern analysis, it was observed that the Ti_2C MXene was produced by using NaOH etching which could be confirmed by the characteristics peaks at $2\theta=7.25^0$. However, the Ti_2AlC powders were partially etched.
- The first cycle charge-discharge capacities were found to be 658.02 $mAhg^{-1}$ and 419.11 $mAhg^{-1}$ with a columbic efficiency of 63.6%. The low efficiency during first cycle was caused by the formation of the SEI layer and the irreversible reaction of the electrolyte with the electrode surface. However, after the third cycle, the efficiency was stabilized and after 20 cycles a capacity of 283.7 $mAhg^{-1}$ was found with an efficiency of 90.9%.
- This electrode shows excellent rate performance, capacity retention, and stability up to 100 cycles ascribed to the formation of –OH terminal group on the surface of Ti_2C MXene.

5.2 Limitations

A novel two-dimensional Ti_2C MXene anode is fabricated and carefully investigated its performances. However, several limitations are encountered during the investigation. The following list are the limitations of this study:

- The Ti_2AlC MAX phase used in this study was bought from china, which was 99% pure.
- $LiCoO_2$ sheet, which was bought from China, served as the cathode material for this research. The voltage of the manufactured LIBS fell because there was less active material on the sheet.
- Volatile and photosensitive $LiPF_6$ was employed in the investigation. The electrolyte disintegrated readily in the open air. One of the main difficulties in this investigation was handling the electrolyte in an open setting.
- Lithium-ion batteries (LIBs) require a moisture-free environment for testing and installation. The best LIB is made in a glove box setup with an inert atmosphere in a well-controlled, moisture-free environment. The LIB battery was assembled in the open environment due to the lack of a glove box facility, which had an adverse effect on the battery's electrochemical performance.

5.3 Future Study

The number of applications for MXenes have recently been explored such as water purification, electromagnetic interference (EMI) shielding, biosensors, transparent conductive electrodes, and as electrodes for lithium, sodium, potassium, and aluminum- ion batteries. MXenes can be considered as promising anode materials for LIBs due to their superior mechanical properties, low Li^+ diffusion resistance, and metal conductivity as shown in Fig. 5.1.

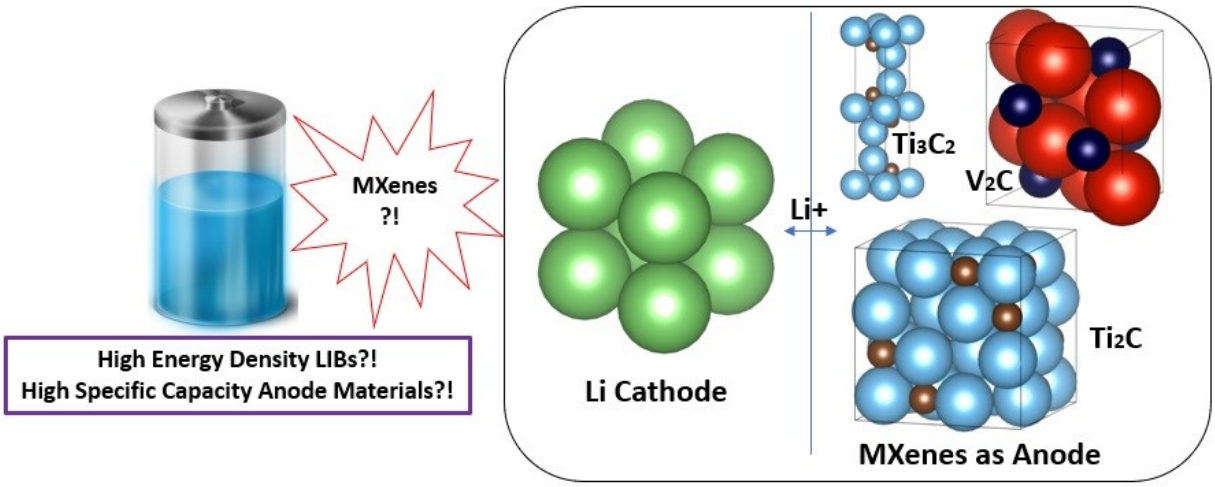

Figure 5.1 Schematic representation of LIB with MXene as anode.

However, there are still several key issues that need to be studied to improve the performance when MXenes are used as anode of LIBs are follows:

- Lithium compound is used as cathode materials of commercial LIBs when graphite is used as anode materials. However, pure Li metal is used as cathode materials in most of the studies when MXene materials are used as anode. Hence, it is necessary to find which commercial grade Li compound is more suitable to respective MXenes as anode of LIBs.
- As of right now, acid etching remains the primary way of obtaining MXenes; nevertheless, it comes with a high risk and low yield. As a result, there is a pressing need for safe, effective, high-quality, and environmentally friendly methods to synthesize MXenes that have a controlled number of layers, modifiable surface groups, enhanced layer spacing, and superior quality. To support the feasible large-scale commercial production of MXenes and MXenes-based materials, it is also necessary to do extensive research on the generation mechanism and optimize the currently available synthesis techniques. In addition, the surface chemistry of these materials is mostly unknown which is necessary to study more before using as anode of LIBs.
- At present, most synthesized MXenes are in powdered form which neEDX to be glued by using binder materials and pasted on the current collector. The

active materials of MXenes might lose connection during electrochemical cycling of LIBs and mixed with electrolyte which led to low practical energy density.

- The proper electrolytes need to be found that will not react with MXenes materials during the electrochemical cycling of LIBs.

Success in addressing these issues should lead to the successful application of MXenes as the anode of LIBs at this very early stage of this type of research.

REFERENCES

1. Zhong, Y.; Xia, X.H.; Shi, F.; Zhan, J.Y.; Tu, J.P.; Fan, H.J. Transition Metal Carbides and Nitrides in Energy Storage and Conversion. Advanced Science 2015, 3.

2. Nitta, N.; Wu, F.; Lee, J.T.; Yushin, G. Li-Ion Battery Materials: Present and Future. Materials Today 2015, 18, 252–264.

3. Pasta, M.; Wessells, C.D.; Liu, N.; Nelson, J.; McDowell, M.T.; Huggins, R.A.; Toney, M.F.; Cui, Y. Full Open-Framework Batteries for Stationary Energy Storage. Nat Commun 2014, 5, 1–9, doi:10.1038/ncomms4007.

4. Divya, K.C.; Østergaard, J. Battery Energy Storage Technology for Power Systems-An Overview. Electric Power Systems Research 2009, 79, 511–520, doi:10.1016/j.epsr.2008.09.017.

5. Yang, Y.; Bremner, S.; Menictas, C.; Kay, M. Battery Energy Storage System Size Determination in Renewable Energy Systems: A Review. Renewable and Sustainable Energy Reviews 2018, 91, 109–125, doi:10.1016/j.rser.2018.03.047.

6. Koohi-Fayegh, S.; Rosen, M.A. A Review of Energy Storage Types, Applications and Recent Developments. J Energy Storage 2020, 27, 101047, doi:10.1016/j.est.2019.101047.

7. Kumar, U.; Gaikwad, V.; Mayyas, M.; Sahajwalla, V.; Joshi, R.K. Extraordinary Supercapacitance in Activated Carbon Produced via a Sustainable Approach. J Power Sources 2018, 394, 140–147, doi:10.1016/j.jpowsour.2018.05.054.

8. Kim, B.K.; Sy, S.; Yu, A.; Zhang, J. Electrochemical Supercapacitors for Energy Storage and Conversion. Handbook of Clean Energy Systems 2015, 1–25, doi:10.1002/9781118991978.hces112.

9. Afif, A.; Rahman, S.M.; Tasfiah Azad, A.; Zaini, J.; Islam, M.A.; Azad, A.K. Advanced Materials and Technologies for Hybrid Supercapacitors for Energy Storage – A Review. J Energy Storage 2019, 25, 100852, doi:10.1016/j.est.2019.100852.

10. Liu, S.; Wei, L.; Wang, H. Review on Reliability of Supercapacitors in Energy Storage Applications. Appl Energy 2020, 278, 115436, doi:10.1016/j.apenergy.2020.115436.

11. Mitali, J.; Dhinakaran, S.; Mohamad, A.A. Energy Storage Systems: A Review. Energy Storage and Saving 2022, 1, 166–216, doi:10.1016/j.enss.2022.07.002.

12. Şahin, M.E.; Blaabjerg, F. A Hybrid PV-Battery/Supercapacitor System and a Basic Active Power Control Proposal in MATLAB/Simulink. Electronics (Basel) 2020, 9.

13. Fernão Pires, V.; Romero-Cadaval, E.; Vinnikov, D.; Roasto, I.; Martins, J.F. Power Converter Interfaces for Electrochemical Energy Storage Systems - A Review. Energy Convers Manag 2014, 86, 453–475, doi:10.1016/j.enconman.2014.05.003.

14. Manthiram, A. An Outlook on Lithium Ion Battery Technology. ACS Cent Sci 2017, 3, 1063–1069, doi:10.1021/acscentsci.7b00288.

15. No Title. https://manuallibbarish.z19.web.core.windows.net/lithium-ion-battery-schematic-diagram.html.

16. Nzereogu, P.U.; Omah, A.D.; Ezema, F.I.; Iwuoha, E.I.; Nwanya, A.C. Anode Materials for Lithium-Ion Batteries: A Review. Applied Surface Science Advances 2022, 9.

17. Arafat Rahman, M. Porous Anode Materials for High Performance Lithium-Ion Batteries; 2016;

18. Kumar Sen, U.; Shaligram, A.; Mitra, S. Intercalation Anode Material for Lithium Ion Battery Based on Molybdenum Dioxide. ACS Appl Mater Interfaces 2014, 6, 14311–14319, doi:10.1021/am503605u.

19. Kamali Heidari, E.; Kamyabi-Gol, A.; Heydarzadeh Sohi, M.; Ataie, A. Electrode Materials for Lithium Ion Batteries: A Review. Journal of Ultrafine Grained and Nanostructured Materials 2018, 51, 1–12, doi:10.22059/JUFGNSM.2018.01.01.

20. Zhang, L.; Wu, H. Bin; Lou, X.W. Iron-Oxide-Based Advanced Anode Materials for Lithium-Ion Batteries. Adv Energy Mater 2014, 4, doi:10.1002/aenm.201300958.

21. Yu, S.H.; Lee, S.H.; Lee, D.J.; Sung, Y.E.; Hyeon, T. Conversion Reaction-Based Oxide Nanomaterials for Lithium Ion Battery Anodes. Small 2016, 12, 2146–2172, doi:10.1002/smll.201502299.

22. Park, C.M.; Kim, J.H.; Kim, H.; Sohn, H.J. Li-Alloy Based Anode Materials for Li Secondary Batteries. Chem Soc Rev 2010, 39, 3115–3141, doi:10.1039/b919877f.

23. Naguib, M.; Come, J.; Dyatkin, B.; Presser, V.; Taberna, P.L.; Simon, P.; Barsoum, M.W.; Gogotsi, Y. MXene: A Promising Transition Metal Carbide Anode for Lithium-Ion Batteries. Electrochem commun 2012, 16, 61–64, doi:10.1016/j.elecom.2012.01.002.

24. Michael, J.; Qifeng, Z.; Danling, W. Titanium Carbide MXene: Synthesis, Electrical and Optical Properties and Their Applications in Sensors and Energy Storage Devices. Nanomaterials and Nanotechnology 2019, 9.

25. Paul, S.; Rahman, M.A.; Islam, M.S.; Islam, M.R.; Siddiqui, S.E.T. Nanostructured Anatase TiO2 as Anode of High-Performance Lithium-Ion Batteries. Battery Energy 2022, 1, 1–17, doi:10.1002/bte2.20220018.

26. Siddiqui, S.-E.-T.; Rahman, Md.A.; Islam, Md.S.; Kim, J.-H.; Barua, N. Microstructured Pebble Stone like Ni-NiO Composite as Anode of High-Performance Lithium-Ion Batteries. Future Sustainability 2024, 2, 1–13, doi:10.55670/fpll.fusus.2.1.1.

27. Rahman, M.A.; Rahman, M.M.; Song, G. A Review on Binder-Free NiO-Ni Foam as Anode of High Performance Lithium-Ion Batteries. Energy Storage 2022, 4, 1–11, doi:10.1002/est2.278.

28. Paul, A.; Rahman, Md.A.; Barua, N. Study of Temperature Cycling of Commercial Rechargeable Lithium-Ion Batteries. Future Sustainability 2023, 1, 23–31, doi:10.55670/fpll.fusus.1.1.3.

29. Lukatskaya, M.R.; Mashtalir, O.; Ren, C.E.; Dall'Agnese, Y.; Rozier, P.; Taberna, P.L.; Naguib, M.; Simon, P.; Barsoum, M.W.; Gogotsi, Y. Cation Intercalation and High Volumetric Capacitance of Two-Dimensional Titanium Carbide. Science (1979) 2013, 341, 1502–1505, doi:10.1126/science.1241488.

30. Zhan, C.; Sun, W.; Kent, P.R.C.; Naguib, M.; Gogotsi, Y.; Jiang, D.E. Computational Screening of MXene Electrodes for Pseudocapacitive Energy Storage. Journal of Physical Chemistry C 2019, 123, 315–321, doi:10.1021/acs.jpcc.8b11608.

31. Dahlqvist, M.; Lu, J.; Meshkian, R.; Tao, Q.; Hultman, L.; Rosen, J. Prediction and Synthesis of a Family of Atomic Laminate Phases with Kagomé-like and in-Plane Chemical Ordering. Sci Adv 2017, 3, 1–9, doi:10.1126/sciadv.1700642.

32. Frey, N.C.; Wang, J.; Vega Bellido, G.I.; Anasori, B.; Gogotsi, Y.; Shenoy, V.B. Prediction of Synthesis of 2D Metal Carbides and Nitrides (MXenes) and Their Precursors with Positive and Unlabeled Machine Learning. ACS Nano 2019, 13, 3031–3041, doi:10.1021/acsnano.8b08014.

33. Gogotsi, Y.; Anasori, B. The Rise of MXenes. ACS Nano 2019, 13, 8491–8494.

34. Sun, W.; Shah, S.A.; Chen, Y.; Tan, Z.; Gao, H.; Habib, T.; Radovic, M.; Green, M.J. Electrochemical Etching of Ti2AlC to Ti2CT:X (MXene) in Low-Concentration Hydrochloric Acid Solution. J Mater Chem A Mater 2017, 5, 21663–21668, doi:10.1039/c7ta05574a.

35. Li, M.; Lu, J.; Luo, K.; Li, Y.; Chang, K.; Chen, K.; Zhou, J.; Rosen, J.; Hultman, L.; Eklund, P.; et al. Element Replacement Approach by Reaction with Lewis Acidic Molten Salts to Synthesize Nanolaminated MAX Phases and MXenes. J Am Chem Soc 2019, 141, 4730–4737, doi:10.1021/jacs.9b00574.

36. Dall'Agnese, Y.; Taberna, P.L.; Gogotsi, Y.; Simon, P. Two-Dimensional Vanadium Carbide (MXene) as Positive Electrode for Sodium-Ion Capacitors. Journal of Physical Chemistry Letters 2015, 6, 2305–2309, doi:10.1021/acs.jpclett.5b00868.

37. Xie, X.; Zhao, M.Q.; Anasori, B.; Maleski, K.; Ren, C.E.; Li, J.; Byles, B.W.; Pomerantseva, E.; Wang, G.; Gogotsi, Y. Porous Heterostructured MXene/Carbon Nanotube Composite Paper with High Volumetric Capacity for Sodium-Based Energy Storage Devices. Nano Energy 2016, 26, 513–523, doi:10.1016/j.nanoen.2016.06.005.

38. Ren, C.E.; Zhao, M.Q.; Makaryan, T.; Halim, J.; Boota, M.; Kota, S.; Anasori, B.; Barsoum, M.W.; Gogotsi, Y. Porous Two-Dimensional Transition Metal Carbide (MXene) Flakes for High-Performance Li-Ion Storage. ChemElectroChem 2016, 3, 689–693, doi:10.1002/celc.201600059.

39. Naguib, M.; Kurtoglu, M.; Presser, V.; Lu, J.; Niu, J.; Heon, M.; Hultman, L.; Gogotsi, Y.; Barsoum, M.W. Two-Dimensional Nanocrystals Produced by Exfoliation of Ti 3AlC 2. Advanced Materials 2011, 23, 4248–4253, doi:10.1002/adma.201102306.

40. Barsoum, M.W. The MN+1AXN Phases: A New Class of Solids. Progress in Solid State Chemistry 2000, 28, 201–281, doi:10.1016/s0079-6786(00)00006-6.

41. Naguib, M.; Mochalin, V.N.; Barsoum, M.W.; Gogotsi, Y. 25th Anniversary Article: MXenes: A New Family of Two-Dimensional Materials. Advanced Materials 2014, 26, 992–1005, doi:10.1002/adma.201304138.

42. Cheng, R.; Hu, T.; Zhang, H.; Wang, C.; Hu, M.; Yang, J.; Cui, C.; Guang, T.; Li, C.; Shi, C.; et al. Understanding the Lithium Storage Mechanism of Ti 3 C 2 T x MXene. Journal of Physical Chemistry C 2019, 123, 1099–1109, doi:10.1021/acs.jpcc.8b10790.

43. Wang, H.W.; Naguib, M.; Page, K.; Wesolowski, D.J.; Gogotsi, Y. Resolving the Structure of Ti3C2Tx MXenes through Multilevel Structural Modeling of the Atomic Pair Distribution Function. Chemistry of Materials 2016, 28, 349–359, doi:10.1021/acs.chemmater.5b04250.

44. Anasori, B.; Lukatskaya, M.R.; Gogotsi, Y. 2D Metal Carbides and Nitrides (MXenes) for Energy Storage. Nat Rev Mater 2017, 2, doi:10.1038/natrevmats.2016.98.

45. Wang, X.; Shen, X.; Gao, Y.; Wang, Z.; Yu, R.; Chen, L. Atomic-Scale Recognition of Surface Structure and Intercalation Mechanism of Ti3C2X. J Am Chem Soc 2015, 137, 2715–2721, doi:10.1021/ja512820k.

46. Bashir, T.; Ismail, S.A.; Wang, J.; Zhu, W.; Zhao, J.; Gao, L. MXene Terminating Groups O, –F or –OH, –F or O, –OH, –F, or O, –OH, –Cl? Journal of Energy Chemistry 2023, 76, 90–104, doi:https://doi.org/10.1016/j.jechem.2022.08.032.

47. Halim, J.; Cook, K.M.; Naguib, M.; Eklund, P.; Gogotsi, Y.; Rosen, J.; Barsoum, M.W. X-Ray Photoelectron Spectroscopy of Select Multi-Layered Transition Metal Carbides (MXenes). Appl Surf Sci 2016, 362, 406–417, doi:10.1016/j.apsusc.2015.11.089.

48. Xie, Y.; Naguib, M.; Mochalin, V.N.; Barsoum, M.W.; Gogotsi, Y.; Yu, X.; Nam, K.W.; Yang, X.Q.; Kolesnikov, A.I.; Kent, P.R.C. Role of Surface Structure on

Li-Ion Energy Storage Capacity of Two-Dimensional Transition-Metal Carbides. J Am Chem Soc 2014, 136, 6385–6394, doi:10.1021/ja501520b.

49. Khazaei, M.; Arai, M.; Sasaki, T.; Chung, C.Y.; Venkataramanan, N.S.; Estili, M.; Sakka, Y.; Kawazoe, Y. Novel Electronic and Magnetic Properties of Two-Dimensional Transition Metal Carbides and Nitrides. Adv Funct Mater 2013, 23, 2185–2192, doi:10.1002/adfm.201202502.

50. Enyashin, A.N.; Ivanovskii, A.L. Atomic Structure, Comparative Stability and Electronic Properties of Hydroxylated Ti 2C and Ti 3C 2 Nanotubes. Comput Theor Chem 2012, 989, 27–32, doi:10.1016/j.comptc.2012.02.034.

51. Anasori, B.; Xie, Y.; Beidaghi, M.; Lu, J.; Hosler, B.C.; Hultman, L.; Kent, P.R.C.; Gogotsi, Y.; Barsoum, M.W. Two-Dimensional, Ordered, Double Transition Metals Carbides (MXenes). MXenes: From Discovery to Applications of Two-Dimensional Metal Carbides and Nitrides 2023, 55–77, doi:10.1201/9781003306511-6.

52. Lang, Z.; Zhuang, Z.; Li, S.; Xia, L.; Zhao, Y.; Zhao, Y.; Han, C.; Zhou, L. MXene Surface Terminations Enable Strong Metal-Support Interactions for Efficient Methanol Oxidation on Palladium. ACS Appl Mater Interfaces 2020, 12, 2400–2406, doi:10.1021/acsami.9b17088.

53. Ling, C.; Shi, L.; Ouyang, Y.; Wang, J. Searching for Highly Active Catalysts for Hydrogen Evolution Reaction Based on O-Terminated MXenes through a Simple Descriptor. Chemistry of Materials 2016, 28, 9026–9032, doi:10.1021/acs.chemmater.6b03972.

54. Gao, G.; O'Mullane, A.P.; Du, A. 2D MXenes: A New Family of Promising Catalysts for the Hydrogen Evolution Reaction. ACS Catal 2017, 7, 494–500, doi:10.1021/acscatal.6b02754.

55. Enyashin, A.N.; Ivanovskii, A.L. Structural and Electronic Properties and Stability of MX Enes Ti 2C and Ti3C2 Functionalized by Methoxy Groups. Journal of Physical Chemistry C 2013, 117, 13637–13643, doi:10.1021/jp401820b.

56. Bai, Y.; Zhou, K.; Srikanth, N.; Pang, J.H.L.; He, X.; Wang, R. Dependence of Elastic and Optical Properties on Surface Terminated Groups in Two-Dimensional MXene Monolayers: A First-Principles Study. RSC Adv 2016, 6, 35731–35739, doi:10.1039/c6ra03090d.

57. Mashtalir, O.; Naguib, M.; Mochalin, V.N.; Dall'Agnese, Y.; Heon, M.; Barsoum, M.W.; Gogotsi, Y. Intercalation and Delamination of Layered Carbides and Carbonitrides. Nat Commun 2013, 4, 1–7, doi:10.1038/ncomms2664.

58. Ladha, D.G. A Review on Density Functional Theory–Based Study on Two-Dimensional Materials Used in Batteries. Mater Today Chem 2019, 11, 94–111, doi:10.1016/j.mtchem.2018.10.006.

59. Li, J.; Yuan, X.; Lin, C.; Yang, Y.; Xu, L.; Du, X.; Xie, J.; Lin, J.; Sun, J. Achieving High Pseudocapacitance of 2D Titanium Carbide (MXene) by Cation Intercalation and Surface Modification. Adv Energy Mater 2017, 7, doi:10.1002/aenm.201602725.

60. Weijia Liu, La Li, Chuqiao Hu, Di Chen, G.S. Intercalation of Small Organic Molecules into Ti3C2Tx MXene Cathodes for Flexible High-Volume-Capacitance Zn-Ion Microsupercapacitor. Adv Mater Technol 2022, 7, doi:https://doi.org/10.1002/admt.202200158.

61. Zhang, P.; Wang, L.; Du, K.; Wang, S.; Huang, Z.; Yuan, L.; Li, Z.; Wang, H.; Zheng, L.; Chai, Z.; et al. Effective Removal of U(VI) and Eu(III) by Carboxyl Functionalized MXene Nanosheets. J Hazard Mater 2020, 396, doi:10.1016/j.jhazmat.2020.122731.

62. Wang, Y.; Feng, W.; Chen, Y. Chemistry of Two-Dimensional MXene Nanosheets in Theranostic Nanomedicine. Chinese Chemical Letters 2020, 31, 937–946, doi:10.1016/j.cclet.2019.11.016.

63. Tang, M.; Li, J.; Wang, Y.; Han, W.; Xu, S.; Lu, M.; Zhang, W.; Li, H. Surface Terminations of MXene: Synthesis, Characterization, and Properties. Symmetry (Basel) 2022, 14, doi:10.3390/sym14112232.

64. Shahzad, A.; Rasool, K.; Nawaz, M.; Miran, W.; Jang, J.; Moztahida, M.; Mahmoud, K.A.; Lee, D.S. Heterostructural TiO2/Ti3C2Tx (MXene) for Photocatalytic Degradation of Antiepileptic Drug Carbamazepine. Chemical Engineering Journal 2018, 349, 748–755, doi:10.1016/j.cej.2018.05.148.

65. Li, X.; Huang, Z.; Zhi, C. Environmental Stability of MXenes as Energy Storage Materials. Front Mater 2019, 6, 2–10, doi:10.3389/fmats.2019.00312.

66. Mehta, V.; Saini, H.S.; Srivastava, S.; Kashyap, M.K.; Tankeshwar, K. S-Functionalized Mo2C Monolayer as a Novel Electrode Material in Li-Ion Batteries. Journal of Physical Chemistry C 2019, 123, 25052–25060, doi:10.1021/acs.jpcc.9b05679.

67. Urbankowski, P.S. Synthesis of Two-Dimensional Transition Metal Nitrides. Drexel University 2019.

68. Yang, S.; Zhang, P.; Wang, F.; Ricciardulli, A.G.; Lohe, M.R.; Blom, P.W.M.; Feng, X. Fluoride-Free Synthesis of Two-Dimensional Titanium Carbide (MXene) Using A Binary Aqueous System. Angewandte Chemie 2018, 130, 15717–15721, doi:10.1002/ange.201809662.

69. Rahman, M.A.; Kim, J.H.; Hossain, S. Recent Advances of Energy Storage Technologies for Grid: A Comprehensive Review. Energy Storage 2022, 4, 1–28, doi:10.1002/est2.322.

70. Rahman, M.A.; Wang, X.; Wen, C. Enhanced Electrochemical Performance of Li-Ion Batteries with Nanoporous Titania as Negative Electrodes. Journal of Energy Chemistry 2015, 24, 157–170, doi:10.1016/S2095-4956(15)60296-0.

71. Chaudhari, N.K.; Jin, H.; Kim, B.; San Baek, D.; Joo, S.H.; Lee, K. MXene: An Emerging Two-Dimensional Material for Future Energy Conversion and Storage Applications. J Mater Chem A Mater 2017, 5, 24564–24579, doi:10.1039/c7ta09094c.

72. Rahman, M.A.; Wong, Y.C.; Song, G.; Zhu, D.M.; Wen, C. Improvement on Electrochemical Performances of Nanoporous Titania as Anode of Lithium-Ion Batteries through Annealing of Pure Titanium Foils. Journal of Energy Chemistry 2018, 27, 250–263, doi:10.1016/j.jechem.2017.07.004.

73. Rahman, M.A.; Song, G.; Bhatt, A.I.; Wong, Y.C.; Wen, C. Nanostructured Silicon Anodes for High-Performance Lithium-Ion Batteries. Adv Funct Mater 2016, 26, 647–678, doi:10.1002/adfm.201502959.

74. Ghidiu, M.; Kota, S.; Halim, J.; Sherwood, A.W.; Nedfors, N.; Rosen, J.; Mochalin, V.N.; Barsoum, M.W. Alkylammonium Cation Intercalation into Ti3C2 (MXene): Effects on Properties and Ion-Exchange Capacity Estimation. Chemistry of Materials 2017, 29, 1099–1106, doi:10.1021/acs.chemmater.6b04234.

75. Magnuson, M.; Greczynski, G.; Eriksson, F.; Hultman, L.; Högberg, H. Electronic Structure of β-Ta Films from X-Ray Photoelectron Spectroscopy and First-Principles Calculations. Appl Surf Sci 2019, 470, 607–612, doi:10.1016/j.apsusc.2018.11.096.

76. Sun, D.; Wang, M.; Li, Z.; Fan, G.; Fan, L.Z.; Zhou, A. Two-Dimensional Ti3C2 as Anode Material for Li-Ion Batteries. Electrochem commun 2014, 47, 80–83, doi:10.1016/j.elecom.2014.07.026.

77. Zhang, T.; Pan, L.; Tang, H.; Du, F.; Guo, Y.; Qiu, T.; Yang, J. Synthesis of Two-Dimensional Ti3C2TxMXene Using HCl+LiF Etchant: Enhanced Exfoliation and Delamination. J Alloys Compd 2017, 695, 818–826, doi:10.1016/j.jallcom.2016.10.127.

78. Huang, L.; Li, T.; Liu, Q.; Gu, J. Fluorine-Free Ti3C2Tx as Anode Materials for Li-Ion Batteries. Electrochem commun 2019, 104, doi:10.1016/j.elecom.2019.05.021.

79. Chen, X.; Zhu, Y.; Zhu, X.; Peng, W.; Li, Y.; Zhang, G.; Zhang, F.; Fan, X. Partially Etched Ti3AlC2 as a Promising High-Capacity Lithium-Ion Battery Anode. ChemSusChem 2018, 11, 2677–2680, doi:10.1002/cssc.201801200.

80. Zhao, Q.; Zhu, Q.; Miao, J.; Zhang, P.; Wan, P.; He, L.; Xu, B. Flexible 3D Porous MXene Foam for High-Performance Lithium-Ion Batteries. Small 2019, 15, 1–9, doi:10.1002/smll.201904293.

81. Li, K.; Liang, M.; Wang, H.; Wang, X.; Huang, Y.; Coelho, J.; Pinilla, S.; Zhang, Y.; Qi, F.; Nicolosi, V.; et al. 3D MXene Architectures for Efficient Energy Storage and Conversion. Adv Funct Mater 2020, 30, 1–22, doi:10.1002/adfm.202000842.

82. Kong, F.; He, X.; Liu, Q.; Qi, X.; Zheng, Y.; Wang, R.; Bai, Y. Improving the Electrochemical Properties of MXene Ti3C2 Multilayer for Li-Ion Batteries by Vacuum Calcination; Elsevier Ltd, 2018; Vol. 265; ISBN 8645186403.

83. Meng, J.; Zhang, F.; Zhang, L.; Liu, L.; Chen, J.; Yang, B.; Yan, X. Rolling up MXene Sheets into Scrolls to Promote Their Anode Performance in Lithium-Ion Batteries. Journal of Energy Chemistry 2020, 46, 256–263, doi:10.1016/j.jechem.2019.10.008.

84. Zhang, S.; Ying, H.; Huang, P.; Wang, J.; Zhang, Z.; Yang, T.; Han, W.Q. Rational Design of Pillared SnS/Ti3C2TxMXene for Superior Lithium-Ion Storage. ACS Nano 2020, 14, 17665–17674, doi:10.1021/acsnano.0c08770.

85. Dai, H.; Zhao, X.; Xu, H.; Yang, J.; Zhou, J.; Chen, Q.; Sun, G. Design of Vertically Aligned Two-Dimensional Heterostructures of Rigid Ti3C2TX MXene and Pliable Vanadium Pentoxide for Efficient Lithium Ion Storage. ACS Nano 2022, 16, 5556–5565, doi:10.1021/acsnano.1c10212.

86. Wang, Y.; Li, Y.; Qiu, Z.; Wu, X.; Zhou, P.; Zhou, T.; Zhao, J.; Miao, Z.; Zhou, J.; Zhuo, S. Fe3O4@Ti3C2 MXene Hybrids with Ultrahigh Volumetric Capacity as an Anode Material for Lithium-Ion Batteries. J Mater Chem A Mater 2018, 6, 11189–11197, doi:10.1039/c8ta00122g.

87. Li, T.; Ding, B.; Wang, J.; Qin, Z.; Fernando, J.F.S.; Bando, Y.; Nanjundan, A.K.; Kaneti, Y.V.; Golberg, D.; Yamauchi, Y. Sandwich-Structured Ordered Mesoporous Polydopamine/MXene Hybrids as High-Performance Anodes for Lithium-Ion Batteries. ACS Appl Mater Interfaces 2020, 12, 14993–15001, doi:10.1021/acsami.9b18883.

88. Liu, H.; Zhang, X.; Zhu, Y.; Cao, B.; Zhu, Q.; Zhang, P.; Xu, B.; Wu, F.; Chen, R. Electrostatic Self-Assembly of 0D–2D SnO2 Quantum Dots/Ti3C2Tx MXene Hybrids as Anode for Lithium-Ion Batteries. Nanomicro Lett 2019, 11, 1–12, doi:10.1007/s40820-019-0296-7.

89. Liu, F.; Zhou, J.; Wang, S.; Wang, B.; Shen, C.; Wang, L.; Hu, Q.; Huang, Q.; Zhou, A. Preparation of High-Purity V 2 C MXene and Electrochemical Properties as Li-Ion Batteries . J Electrochem Soc 2017, 164, A709–A713, doi:10.1149/2.0641704jes.

90. Zhao, S.; Meng, X.; Zhu, K.; Du, F.; Chen, G.; Wei, Y.; Gogotsi, Y.; Gao, Y. Li-Ion Uptake and Increase in Interlayer Spacing of Nb4C3 MXene. Energy Storage Mater 2017, 8, 42–48, doi:10.1016/j.ensm.2017.03.012.

91. Zhou, J.; Lin, S.; Huang, Y.; Tong, P.; Zhao, B.; Zhu, X.; Sun, Y. Synthesis and Lithium Ion Storage Performance of Two-Dimensional V4C3 MXene. Chemical Engineering Journal 2019, 373, 203–212, doi:10.1016/j.cej.2019.05.037.

92. Dong, H.; Xiao, P.; Jin, N.; Wang, B.; Liu, Y.; Lin, Z. Molten Salt Derived Nb2CTx MXene Anode for Li-Ion Batteries. ChemElectroChem 2021, 8, 957–962, doi:10.1002/celc.202100142.

93. Zhao, J.; Wen, J.; Bai, L.; Xiao, J.; Zheng, R.; Shan, X.; Li, L.; Gao, H.; Zhang, X. One-Step Synthesis of Few-Layer Niobium Carbide MXene as a Promising Anode Material for High-Rate Lithium Ion Batteries. Dalton Transactions 2019, 48, 14433–14439, doi:10.1039/c9dt03260f.

94. Luo, W.; Liu, Y.; Li, F.; Huo, J.; Zhao, D.; Zhu, J.; Guo, S. H2O2 Assisted Hydrothermal Oxidation of Partially Etched Vanadium Carbides (MXene) and Their Electrochemical Properties as Anode for Li-Ion Batteries. Appl Surf Sci 2020, 523, 146387, doi:10.1016/j.apsusc.2020.146387.

95. Guo, Y.; Liu, D.; Huang, B.; Wang, L.; Xia, Q.; Zhou, A. Effects of Surface Compositions and Interlayer Distance on Electrochemical Performance of Mo2CTx MXene as Anode of Li-Ion Batteries. Journal of Physics and Chemistry of Solids 2023, 176, 111238, doi:10.1016/j.jpcs.2023.111238.

96. Zhou, J.; Zha, X.; Zhou, X.; Chen, F.; Gao, G.; Wang, S.; Shen, C.; Chen, T.; Zhi, C.; Eklund, P.; et al. Synthesis and Electrochemical Properties of Two-Dimensional Hafnium Carbide. ACS Nano 2017, 11, 3841–3850, doi:10.1021/acsnano.7b00030.

97. Du, F.; Tang, H.; Pan, L.; Zhang, T.; Lu, H.; Xiong, J.; Yang, J.; Zhang, C. (John) Environmental Friendly Scalable Production of Colloidal 2D Titanium Carbonitride MXene with Minimized Nanosheets Restacking for Excellent Cycle Life Lithium-Ion Batteries. Electrochim Acta 2017, 235, 690–699, doi:10.1016/j.electacta.2017.03.153.

98. Kim, S.J.; Naguib, M.; Zhao, M.; Zhang, C.; Jung, H.T.; Barsoum, M.W.; Gogotsi, Y. High Mass Loading, Binder-Free MXene Anodes for High Areal Capacity Li-Ion Batteries. Electrochim Acta 2015, 163, 246–251, doi:10.1016/j.electacta.2015.02.132.

99. Naguib, M.; Halim, J.; Lu, J.; Cook, K.M.; Hultman, L.; Gogotsi, Y.; Barsoum, M.W. New Two-Dimensional Niobium and Vanadium Carbides as Promising Materials for Li-Ion Batteries. J Am Chem Soc 2013, 135, 15966–15969, doi:10.1021/ja405735d.

100. Mei, J.; Ayoko, G.A.; Hu, C.; Bell, J.M.; Sun, Z. Two-Dimensional Fluorine-Free Mesoporous Mo2C MXene via UV-Induced Selective Etching of Mo2Ga2C for Energy Storage. Sustainable Materials and Technologies 2020, 25, e00156, doi:10.1016/j.susmat.2020.e00156.

101. Zhang, T.; Pan, L.; Tang, H.; Du, F.; Guo, Y.; Qiu, T.; Yang, J. Synthesis of Two-Dimensional Ti3C2TxMXene Using HCl+LiF Etchant: Enhanced Exfoliation and Delamination. J Alloys Compd 2017, 695, 818–826, doi:10.1016/j.jallcom.2016.10.127.

102. Cheng, Y.; Yang, L.; Yin, S. Synthesis and Lithium Ion Storage Performance of Novel Two Dimensional Vanadium Niobium Carbide (VNbCT x) MXene. Composites Communications 2023, 40, 101588, doi:10.1016/j.coco.2023.101588.

103. Liu, W.; Cao, J.; Song, F.; Zhang, D.D.; Okhawilai, M.; Yi, J.; Qin, J.Q.; Zhang, X.Y. A Double Transition Metal Ti2NbC2Tx MXene for Enhanced Lithium-Ion Storage. Rare Metals 2023, 42, 100–110, doi:10.1007/s12598-022-02120-z.

104. Wang, Y.; Zheng, W.; Zhang, P.; Tian, W.; Chen, J.; Sun, Z.M. Preparation of (Vx, Ti1−x)2C MXenes and Their Performance as Anode Materials for LIBs. J Mater Sci 2019, 54, 11991–11999, doi:10.1007/s10853-019-03756-6.

105. Syamsai, R.; Rodriguez, J.R.; Pol, V.G.; Van Le, Q.; Batoo, K.M.; Farooq, S.A.; Pandiaraj, S.; Muthumareeswaran, M.R.; Raslan, E.H.; Grace, A.N. Double Transition Metal MXene (TixTa4−xC3) 2D Materials as Anodes for Li-Ion Batteries. Sci Rep 2021, 11, 1–13, doi:10.1038/s41598-020-79991-8.

106. Yang, J.; Naguib, M.; Ghidiu, M.; Pan, L.M.; Gu, J.; Nanda, J.; Halim, J.; Gogotsi, Y.; Barsoum, M.W. Two-Dimensional Nb-Based M4C3 Solid Solutions (MXenes). Journal of the American Ceramic Society 2016, 99, 660–666, doi:10.1111/jace.13922.

107. Liu, W.; Cao, J.; Song, F.; Zhang, D.D.; Okhawilai, M.; Yi, J.; Qin, J.Q.; Zhang, X.Y. A Double Transition Metal Ti2NbC2Tx MXene for Enhanced Lithium-Ion Storage. Rare Metals 2023, 42, 100–110, doi:10.1007/s12598-022-02120-z.

108. Li, C.; Xue, Z.; Qin, J.; Sawangphruk, M.; Yu, P.; Zhang, X.; Liu, R. Synthesis of Nickel Hydroxide/Delaminated-Ti3C2 MXene Nanosheets as Promising Anode Material for High Performance Lithium Ion Battery. J Alloys Compd 2020, 842, 155812, doi:10.1016/j.jallcom.2020.155812.

109. Zhang, R.; Xue, Z.; Qin, J.; Sawangphruk, M.; Zhang, X.; Liu, R. NiCo-LDH/Ti3C2 MXene Hybrid Materials for Lithium Ion Battery with High-Rate Capability and Long Cycle Life. Journal of Energy Chemistry 2020, 50, 143–153, doi:10.1016/j.jechem.2020.03.018.

110. Li, C.; Zhang, D.; Cao, J.; Yu, P.; Okhawilai, M.; Yi, J.; Qin, J.; Zhang, X. Ti3C2MXene-Encapsulated NiFe-LDH Hybrid Anode for High-Performance Lithium-Ion Batteries and Capacitors. ACS Appl Energy Mater 2021, 4, 7821–7828, doi:10.1021/acsaem.1c01171.

111. Hui, X.; Zhao, R.; Zhang, P.; Li, C.; Wang, C.; Yin, L. Low-Temperature Reduction Strategy Synthesized Si/Ti3C2 MXene Composite Anodes for High-Performance Li-Ion Batteries. Adv Energy Mater 2019, 9, 1–10, doi:10.1002/aenm.201901065.

112. Zhou, H.; Zhang, J.; Liu, J.; Feng, S.; Li, C.; Marsili, E.; Zhang, X. Silicon Nanospheres Supported on Conductive MXene Nanosheets as Anodes for Lithium-Ion Batteries. ACS Appl Energy Mater 2023, 6, 160–169, doi:10.1021/acsaem.2c02706.

113. Tian, Y.; An, Y.; Feng, J. Flexible and Freestanding Silicon/MXene Composite Papers for High-Performance Lithium-Ion Batteries. ACS Appl Mater Interfaces 2019, 11, 10004–10011, doi:10.1021/acsami.8b21893.

114. Zhang, Z.; Ying, H.; Huang, P.; Zhang, S.; Zhang, Z.; Yang, T.T.; Han, W.Q. Porous Si Decorated on MXene as Free-Standing Anodes for Lithium-Ion Batteries with Enhanced Diffusion Properties and Mechanical Stability. Chemical Engineering Journal 2023, 451, 138785, doi:10.1016/j.cej.2022.138785.

115. Bashir, T.; Li, X.; Yang, S.; Song, Y.; Zhou, S.; Wang, J.; Zhu, W.; Yang, J.; Zhao, J.; Gao, L. Enhancing Role of Structurally Integrated V2C MXene Nanosheets on Silicon Anode for Lithium Storage. J Alloys Compd 2022, 922, 166213, doi:10.1016/j.jallcom.2022.166213.

116. Maughan, P.A.; Bouscarrat, L.; Seymour, V.R.; Shao, S.; Haigh, S.J.; Dawson, R.; Tapia-Ruiz, N.; Bimbo, N. Pillared Mo2TiC2MXene for High-Power and Long-Life Lithium and Sodium-Ion Batteries. Nanoscale Adv 2021, 3, 3145–3158, doi:10.1039/d1na00081k.

117. Mu, G.; Mu, D.; Wu, B.; Ma, C.; Bi, J.; Zhang, L.; Yang, H.; Wu, F. Microsphere-Like SiO2/MXene Hybrid Material Enabling High Performance Anode for Lithium Ion Batteries. Small 2020, 16, 1–9, doi:10.1002/smll.201905430.

118. Han, X.; Zhou, W.; Chen, M.; Chen, J.; Wang, G.; Liu, B.; Luo, L.; Chen, S.; Zhang, Q.; Shi, S.; et al. Interfacial Nitrogen Engineering of Robust Silicon/MXene Anode toward High Energy Solid-State Lithium-Ion Batteries. Journal of Energy Chemistry 2022, 67, 727–735, doi:10.1016/j.jechem.2021.11.021.

119. Zhang, K.; Zhao, D.; Qian, Z.; Gu, X.; Yang, J.; Qian, Y. N-Doped Ti3C2Tx MXene Sheet-Coated SiOx to Boost Lithium Storage for Lithium-Ion Batteries. Sci China Mater 2023, 66, 51–60, doi:10.1007/s40843-022-2142-1.

120. Choudhury, R.; Kurra, N.; Meduri, P. Doped Micro-Silicon and Vanadium Carbide MXene Composite as Anode for High Stability and High Capacity Li-Ion Batteries. Results in Engineering 2023, 19, 101338, doi:10.1016/j.rineng.2023.101338.

121. Zhao, N.; Yang, Y.; Yi, D.; Xiao, Y.; Wang, K.; Cui, W.; Wang, X. Regulating Fe–O Bond in Ti3C2Tx MXene Anode for High-Capacity Li-Ion Batteries. Chemical Engineering Journal 2021, 422, 130018, doi:10.1016/J.CEJ.2021.130018.

122. Huang, P.; Zhang, S.; Ying, H.; Yang, W.; Wang, J.; Guo, R.; Han, W. Fabrication of Fe Nanocomplex Pillared Few-Layered Ti3C2Tx MXene with Enhanced Rate Performance for Lithium-Ion Batteries. Nano Res 2021, 14, 1218–1227, doi:10.1007/s12274-020-3221-y.

123. Wan, L.; Chua, D.H.C.; Sun, H.; Chen, L.; Wang, K.; Lu, T.; Pan, L. Construction of Two-Dimensional Bimetal (Fe-Ti) Oxide/Carbon/MXene Architecture from Titanium Carbide MXene for Ultrahigh-Rate Lithium-Ion Storage. J Colloid Interface Sci 2021, 588, 147–156, doi:10.1016/j.jcis.2020.12.071.

124. Zhang, Z.; Weng, L.; Rao, Q.; Yang, S.; Hu, J.; Cai, J.; Min, Y. Highly-Dispersed Iron Oxide Nanoparticles Anchored on Crumpled Nitrogen-Doped MXene Nanosheets as Anode for Li-Ion Batteries with Enhanced Cyclic and Rate Performance. J Power Sources 2019, 439, 227107, doi:10.1016/j.jpowsour.2019.227107.

125. He, L.; Tan, C.; Sheng, C.; Chen, Y.; Yu, F.; Chen, Y. A β-FeOOH/MXene Sandwich for High-Performance Anodes in Lithium-Ion Batteries. Dalton Transactions 2020, 49, 9268–9273, doi:10.1039/d0dt01531h.

126. Nam, S.; Umrao, S.; Oh, S.; Shin, K.H.; Park, H.S.; Oh, I.K. Sonochemical Self-Growth of Functionalized Titanium Carbide Nanorods on Ti3C2 Nanosheets for High Capacity Anode for Lithium-Ion Batteries. Compos B Eng 2020, 181, 107583, doi:10.1016/j.compositesb.2019.107583.

127. Lv, X.; Deng, Z.; Wang, M.; Deng, J. Ti3C2 MXene Derived Carbon-Doped TiO2 Multilayers Anchored with Fe2O3 Nanoparticles as Anode for Enhanced Lithium-Ion Storage. J Alloys Compd 2022, 918, 165697, doi:10.1016/j.jallcom.2022.165697.

128. Wu, Z.; Zhu, S.; Bai, X.; Liang, M.; Zhang, X.; Zhao, N. One-Step in-Situ Synthesis of Sn-Nanoconfined Ti 3 C 2 T x MXene Composites for Li-Ion Battery Anode. Electrochim Acta 2022, 407, 139916, doi:10.1016/j.electacta.2022.139916.

129. Luo, J.; Tao, X.; Zhang, J.; Xia, Y.; Huang, H.; Zhang, L.; Gan, Y.; Liang, C.; Zhang, W. Sn4+ Ion Decorated Highly Conductive Ti3C2 MXene: Promising Lithium-Ion Anodes with Enhanced Volumetric Capacity and Cyclic Performance. ACS Nano 2016, 10, 2491–2499, doi:10.1021/acsnano.5b07333.

130. Ahmed, B.; Anjum, D.H.; Gogotsi, Y.; Alshareef, H.N. Atomic Layer Deposition of SnO2 on MXene for Li-Ion Battery Anodes. Nano Energy 2017, 34, 249–256, doi:10.1016/j.nanoen.2017.02.043.

131. Liu, D.; Wang, L.; He, Y.; Liu, L.; Yang, Z.; Wang, B.; Xia, Q.; Hu, Q.; Zhou, A. Enhanced Reversible Capacity and Cyclic Performance of Lithium-Ion Batteries Using SnO2 Interpenetrated MXene V2C Architecture as Anode Materials. Energy Technology 2021, 9, doi:10.1002/ente.202000753.

132. Fan, W.; Xue, J.; Wang, D.; Chen, Y.; Liu, H.; Xia, X. Sandwich-Structured Sn4P3@MXene Hybrid Anodes with High Initial Coulombic Efficiency for High-Rate Lithium-Ion Batteries. ACS Appl Mater Interfaces 2021, 13, 61055–61066, doi:10.1021/acsami.1c17297.

133. Li, J.; Han, L.; Li, Y.; Li, J.; Zhu, G.; Zhang, X.; Lu, T.; Pan, L. MXene-Decorated SnS2/Sn3S4 Hybrid as Anode Material for High-Rate Lithium-Ion Batteries. Chemical Engineering Journal 2020, 380, 122590, doi:10.1016/j.cej.2019.122590.

134. Zhu, M.; Deng, X.; Ke, J.; Feng, Z.; He, M.; Feng, Y.; Xiong, D. Graphite Nano-Modified SnO2-Ti2C MXene as Anode Material for High-Performance Lithium-Ion Batteries. J Alloys Compd 2021, 886, 161139, doi:10.1016/j.jallcom.2021.161139.

135. Zuo, D. chuan; Song, S. chao; An, C. sheng; Tang, L. bo; He, Z. jiang; Zheng, J. chao Synthesis of Sandwich-like Structured Sn/SnOx@MXene Composite through in-Situ Growth for Highly Reversible Lithium Storage. Nano Energy 2019, 62, 401–409, doi:10.1016/j.nanoen.2019.05.062.

136. Abdurehman Tariq, H.; Nisar, U.; James Abraham, J.; Ahmad, Z.; AlQaradawi, S.; Kahraman, R.; Shakoor, R.A. TiO2 Encrusted MXene as a High-Performance Anode Material for Li-Ion Batteries. Appl Surf Sci 2022, 583, 152441, doi:10.1016/j.apsusc.2022.152441.

137. Jia, Y.; Liu, J.; Shang, L. Layered Structure 2D MXene/TiO2 Composites as High-Performance Anodes for Lithium-Ion Batteries. Ionics (Kiel) 2023, 29, 531–537, doi:10.1007/s11581-022-04862-3.

138. Ahmed, B.; Anjum, D.H.; Hedhili, M.N.; Gogotsi, Y.; Alshareef, H.N. H2O2 Assisted Room Temperature Oxidation of Ti2C MXene for Li-Ion Battery Anodes. Nanoscale 2016, 8, 7580–7587, doi:10.1039/c6nr00002a.

139. Zhang, X.; Li, J.; Han, L.; Li, H.; Wang, J.; Lu, T.; Pan, L. In-Situ Fabrication of Few-Layered MoS2 Wrapped on TiO2-Decorated MXene as Anode Material for Durable Lithium-Ion Storage. J Colloid Interface Sci 2021, 604, 30–38, doi:10.1016/j.jcis.2021.07.013.

140. He, Y.; Wang, L.; Wang, X.; Shen, C.; Hu, Q.; Zhou, A.; Liu, X. Surface Reformation of 2D MXene by in Situ LaF3-Decorated and Enhancement of Energy Storage in Lithium-Ion Batteries. Journal of Materials Science: Materials in Electronics 2020, 31, 6735–6743, doi:10.1007/s10854-020-03230-z.

141. Yuan, K.; Hao, P.; Hu, X.; Zhang, J.; Zhou, Y. Experimental and Computational Studies on S-Decorated Ti3C2 MXene as Anode Material in Li-Ion Batteries. J Mater Sci 2022, 57, 7001–7011, doi:10.1007/s10853-022-06983-6.

142. Zhang, W.; Qian, M.; Luo, G.; Feng, X.; Wu, C.; Qin, W. Improved Lithium Ion Storage Performance of Ti 3 C 2 T x MXene @ S Composite with Carboxymethyl Cellulose Binder. J Colloid Interface Sci 2023, 641, 15–25, doi:10.1016/j.jcis.2023.03.074.

143. Zou, G.; Zhang, Z.; Guo, J.; Liu, B.; Zhang, Q.; Fernandez, C.; Peng, Q. Synthesis of MXene/Ag Composites for Extraordinary Long Cycle Lifetime Lithium Storage at High Rates. ACS Appl Mater Interfaces 2016, 8, 22280–22286, doi:10.1021/acsami.6b08089.

144. Wang, Z.; Duan, C.; Zhou, Y.; Wen, F.; Lu, Q.; Liu, D.; Wang, F. Ag Decorated 3D Honeycomb-like MXene Architecture as an Advanced Lithium-Ion Anode Material towards High Capacity and Long-Term Cycle Capability. Appl Surf Sci 2023, 615, 156406, doi:10.1016/j.apsusc.2023.156406.

145. Huang, Y.; Yang, H.; Zhang, Y.; Zhang, Y.; Wu, Y.; Tian, M.; Chen, P.; Trout, R.; Ma, Y.; Wu, T.H.; et al. A Safe and Fast-Charging Lithium-Ion Battery Anode Using MXene Supported Li3VO4. J Mater Chem A Mater 2019, 7, 11250–11256, doi:10.1039/c9ta02037c.

146. Liu, R.; Cao, W.; Han, D.; Mo, Y.; Zeng, H.; Yang, H.; Li, W. Nitrogen-Doped Nb2CTx MXene as Anode Materials for Lithium Ion Batteries. J Alloys Compd 2019, 793, 505–511, doi:10.1016/J.JALLCOM.2019.03.209.

147. Zhong, S.; Ju, S.; Shao, Y.; Chen, W.; Zhang, T.; Huang, Y.; Zhang, H.; Xia, G.; Yu, X. Magnesium Hydride Nanoparticles Anchored on MXene Sheets as High Capacity Anode for Lithium-Ion Batteries. Journal of Energy Chemistry 2021, 62, 431–439, doi:10.1016/j.jechem.2021.03.049.

148. Liu, C.; Zhao, Y.; Yi, R.; Wu, H.; Yang, W.; Li, Y.; Mitrovic, I.; Taylor, S.; Chalker, P.; Liu, R.; et al. Enhanced Electrochemical Performance by GeOx-Coated MXene Nanosheet Anode in Lithium-Ion Batteries. Electrochim Acta 2020, 358, 1–12, doi:10.1016/j.electacta.2020.136923.

149. Melchior, S.A.; Palaniyandy, N.; Sigalas, I.; Iyuke, S.E.; Ozoemena, K.I. Probing the Electrochemistry of MXene (Ti2CTx)/Electrolytic Manganese Dioxide (EMD) Composites as Anode Materials for Lithium-Ion Batteries. Electrochim Acta 2019, 297, 961–973, doi:10.1016/j.electacta.2018.12.013.

150. Zhang, P.; Wang, D.; Zhu, Q.; Sun, N.; Fu, F.; Xu, B. Plate - to - Layer Bi 2 MoO 6 / MXene - Heterostructured Anode for Lithium - Ion Batteries. Nanomicro Lett 2019, doi:10.1007/s40820-019-0312-y.

151. Abdah, M.A.A.M.; Cherusseri, J.; Dzulkarnain, N.A.; Mokhtar, M.; Su'ait, M.S.; Tan, Y.S.; Mustafa, M.N.; Khalid, M.; Numan, A.; Radwan, A. Facile Synthesis of Microwave-Etched Ti3C2 MXene/Activated Carbon Hybrid for Lithium-Ion Battery Anode. Journal of Electroanalytical Chemistry 2023, 928, doi:10.1016/j.jelechem.2022.117050.

152. Liu, H.; He, P.; Cao, J.; Duan, T.; Kong, Q.; Yao, W. Multidimensional VO 2 Nanotubes / Ti 3 C 2 MXene Composite for Efficient Electrochemical Lithium / Sodium-Ion Storage. J Power Sources 2022, 521, 230946, doi:10.1016/j.jpowsour.2021.230946.

153. Ma, Q.; Zhang, Z.; Kou, P.; Wang, D.; Wang, Z.; Sun, H.; Zheng, R.; Liu, Y. In-Situ Synthesis of Niobium-Doped TiO2 Nanosheet Arrays on Double Transition Metal MXene (TiNbCTx) as Stable Anode Material for Lithium-Ion

Batteries. J Colloid Interface Sci 2022, 617, 147–155, doi:10.1016/j.jcis.2022.03.007.

154. Xu, C.; Feng, K.; Yang, X.; Cheng, Y.; Zhao, X.; Yang, L.; Yin, S. In-Situ Construction of Metallic Oxide (VNbO5) on VNbCTx MXene for Enhanced Li-Ion Batteries Performance. J Energy Storage 2023, 69, doi:10.1016/j.est.2023.107888.

155. Luo, Y.; Zhao, Y.; Ma, J.; Huang, Y.; Han, S.; Zhou, M.; Lin, H. Sandwich-like Na2Ti3O7Nanosheet/Ti3C2MXene Composite for High-Performance Lithium/Sodium-Ion Batteries. Journal of Physical Chemistry C 2022, 126, 18229–18237, doi:10.1021/acs.jpcc.2c05670.

156. Gong, S.; Wang, Y.; Zhang, P.; Li, M.; Wen, Y.; Qiu, J.; Xu, B.; Wang, H. Self-Assembly TiNb2O7@MXene Anode Material for Fast and Stable Lithium Storage. Energy and Fuels 2023, 37, 3159–3165, doi:10.1021/acs.energyfuels.2c03623.

157. Qi, X.; Xu, W.X.; Tang, J.L.; Xu, Y.T.; Gao, Y.; Li, L.; Sasaki, S. ichi; Tamiaki, H.; Wang, X.F. Chlorophyll Derivative Intercalation into Nb2C MXene for Lithium-Ion Energy Storage. J Mater Sci 2022, 57, 9971–9979, doi:10.1007/s10853-022-06929-y.

158. Tian, S.; Wang, D.; Liu, Z.; Liu, G.; Zeng, Q.; Sun, X.; Yang, H.; Han, C.; Tao, K.; Peng, S. Highly Reversible Lithium-Ion Battery with Excellent Rate Performance and Cycle Stability Based on a Ti3C2/CoS2 Composite Anode. ACS Appl Mater Interfaces 2023, 15, 44996–45004, doi:10.1021/acsami.3c09605.

159. Shen, C.; Wang, L.; Zhou, A.; Zhang, H.; Chen, Z.; Hu, Q.; Qin, G. MoS 2 - Decorated Ti 3 C 2 MXene Nanosheet as Anode Material in Lithium-Ion Batteries . J Electrochem Soc 2017, 164, A2654–A2659, doi:10.1149/2.1421712jes.

160. Chen, C.; Xie, X.; Anasori, B.; Sarycheva, A.; Makaryan, T.; Zhao, M.; Urbankowski, P.; Miao, L.; Jiang, J.; Gogotsi, Y. MoS2-on-MXene Heterostructures as Highly Reversible Anode Materials for Lithium-Ion Batteries. Angewandte Chemie - International Edition 2018, 57, 1846–1850, doi:10.1002/anie.201710616.

161. Kamat, R.S.; Padwal, C.; Pham, H.D.; Wang, X.; Jadhav, L.D.; Dubal, D.P. Selenium Enriched Over-Oxidized Mo3Se4 Decorated MXene as a High-Performance Li-Ion Battery Anode Material. J Energy Storage 2023, 73, 108916, doi:10.1016/j.est.2023.108916.

162. Bai, J.; Zhao, B.; Lin, S.; Li, K.; Zhou, J.; Dai, J.; Zhu, X.; Sun, Y. Construction of Hierarchical V4C3-MXene/MoS2/C Nanohybrids for High Rate Lithium-Ion Batteries. Nanoscale 2020, 12, 1144–1154, doi:10.1039/c9nr07646h.

163. Wei, C.; Fei, H.; Tian, Y.; An, Y.; Zeng, G.; Feng, J.; Qian, Y. Room-Temperature Liquid Metal Confined in MXene Paper as a Flexible, Freestanding, and Binder-Free Anode for Next-Generation Lithium-Ion Batteries. Small 2019, 15, 1–9, doi:10.1002/smll.201903214.

164. Zhang, P.; Soomro, R.A.; Guan, Z.; Sun, N.; Xu, B. 3D Carbon-Coated MXene Architectures with High and Ultrafast Lithium/Sodium-Ion Storage. Energy Storage Mater 2020, 29, 163–171, doi:10.1016/j.ensm.2020.04.016.

165. Wang, C.; Xie, H.; Chen, S.; Ge, B.; Liu, D.; Wu, C.; Xu, W.; Chu, W.; Babu, G.; Ajayan, P.M.; et al. Atomic Cobalt Covalently Engineered Interlayers for Superior Lithium-Ion Storage. Advanced Materials 2018, 30, 1–9, doi:10.1002/adma.201802525.

166. Li, X.; Zhu, J.; Fang, Y.; Lv, W.; Wang, F.; Liu, Y.; Liu, H. Hydrothermal Preparation of CoO/Ti3C2 Composite Material for Lithium-Ion Batteries with Enhanced Electrochemical Performance. Journal of Electroanalytical Chemistry 2018, 817, 1–8, doi:10.1016/j.jelechem.2018.03.031.

167. Zhao, Y.; Liu, C.; Yi, R.; Li, Z.; Chen, Y.; Li, Y.; Mitrovic, I.; Taylor, S.; Chalker, P.; Yang, L.; et al. Facile Preparation of Co3O4 Nanoparticles Incorporating with Highly Conductive MXene Nanosheets as High-Performance Anodes for Lithium-Ion Batteries. Electrochim Acta 2020, 345, 136203, doi:10.1016/j.electacta.2020.136203.

168. Oh, H.G.; Park, S. Two-Dimensional Composite of Nitrogen-Doped Graphitic Carbon-Coated Cobaltosic Oxide Nanocrystals on MXene Nanosheets as High-Performance Anode for Lithium-Ion Batteries. Appl Surf Sci 2021, 564, 150415, doi:10.1016/j.apsusc.2021.150415.

169. Zhang, H.; Dong, H.; Zhang, X.; Xu, Y.; Fransaer, J. Cu2O Hybridized Titanium Carbide with Open Conductive Frameworks for Lithium-Ion Batteries. Electrochim Acta 2016, 202, 24–31, doi:10.1016/j.electacta.2016.04.009.

170. Lin, Z.; Sun, D.; Huang, Q.; Yang, J.; Barsoum, M.W.; Yan, X. Carbon Nanofiber Bridged Two-Dimensional Titanium Carbide as a Superior Anode for Lithium-Ion Batteries. J Mater Chem A Mater 2015, 3, 14096–14100, doi:10.1039/c5ta01855b.

171. Mashtalir, O.; Lukatskaya, M.R.; Zhao, M.Q.; Barsoum, M.W.; Gogotsi, Y. Amine-Assisted Delamination of Nb2C MXene for Li-Ion Energy Storage Devices. Advanced Materials 2015, 27, 3501–3506, doi:10.1002/adma.201500604.

172. Halim, J.; Kota, S.; Lukatskaya, M.R.; Naguib, M.; Zhao, M.Q.; Moon, E.J.; Pitock, J.; Nanda, J.; May, S.J.; Gogotsi, Y.; et al. Synthesis and Characterization of 2D Molybdenum Carbide (MXene). Adv Funct Mater 2016, 26, 3118–3127, doi:10.1002/adfm.201505328.

173. Cheng, R.; Wang, Z.; Cui, C.; Hu, T.; Fan, B.; Wang, H.; Liang, Y.; Zhang, C.; Zhang, H.; Wang, X. One-Step Incorporation of Nitrogen and Vanadium between Ti 3 C 2 T x MXene Interlayers Enhances Lithium Ion Storage

Capability . The Journal of Physical Chemistry C 2020, 124, 6012–6021, doi:10.1021/acs.jpcc.0c00524.

174. Maughan, P.A.; Bouscarrat, L.; Seymour, V.R.; Shao, S.; Haigh, S.J.; Dawson, R.; Tapia-Ruiz, N.; Bimbo, N. Pillared Mo2TiC2MXene for High-Power and Long-Life Lithium and Sodium-Ion Batteries. Nanoscale Adv 2021, 3, 3145–3158, doi:10.1039/d1na00081k.

175. Zhang, K.; Zhao, D.; Qian, Z.; Gu, X.; Yang, J.; Qian, Y. N-Doped Ti 3 C 2 T x MXene Sheet-Coated SiO x to Boost Lithium Storage for Lithium-Ion Batteries. 2023, 66, 51–60.

176. Zhang, P.; Soomro, R.A.; Guan, Z.; Sun, N.; Xu, B. 3D Carbon-Coated MXene Architectures with High and Ultrafast Lithium/Sodium-Ion Storage. Energy Storage Mater 2020, 29, 163–171, doi:10.1016/j.ensm.2020.04.016.

177. Zhu, K.; Jin, Y.; Du, F.; Gao, S.; Gao, Z.; Meng, X.; Chen, G.; Wei, Y.; Gao, Y. Synthesis of Ti 2 CT x MXene as Electrode Materials for Symmetric Supercapacitor with Capable Volumetric Capacitance. Journal of Energy Chemistry 2019, 11–18, doi:10.1016/j.jechem.2018.03.010.

178. Jin, S.; Hu, Q.; Zhou, A. Composition and Hydrogen Storage Structure of Ti 2 CT x MXene with Ultrahigh Hydrogen Storage Capacity. 2013, 1–6.

179. Naguib, M.; Come, J.; Dyatkin, B.; Presser, V.; Taberna, P.L.; Simon, P.; Barsoum, M.W.; Gogotsi, Y. MXene: A Promising Transition Metal Carbide Anode for Lithium-Ion Batteries. Electrochem commun 2012, 16, 61–64, doi:10.1016/j.elecom.2012.01.002.

180. Sun, D.; Wang, M.; Li, Z.; Fan, G.; Fan, L.Z.; Zhou, A. Two-Dimensional Ti3C2 as Anode Material for Li-Ion Batteries. Electrochem commun 2014, 47, 80–83, doi:10.1016/j.elecom.2014.07.026.

181. Li, S.; Luo, Y.; Lv, W.; Yu, W.; Wu, S.; Hou, P.; Yang, Q.; Meng, Q.; Liu, C.; Cheng, H. Vertically Aligned Carbon Nanotubes Grown on Graphene Paper as Electrodes in Lithium-Ion Batteries and Dye-Sensitized Solar Cells. Adv Energy Mater 2011, 1, 486–490, doi:10.1002/aenm.201100001.

182. Shim, J.-H.; Lee, S. Characterization of Graphite Etched with Potassium Hydroxide and Its Application in Fast-Rechargeable Lithium Ion Batteries. J Power Sources 2016, 324, 475–483, doi:10.1016/j.jpowsour.2016.05.094.

183. Liu, Z.; Hong, L.; Guo, B. Physicochemical and Electrochemical Characterization of Anatase Titanium Dioxide Nanoparticles. J Power Sources 2005, 143, 231–235, doi:10.1016/j.jpowsour.2004.11.056.

184. Yuan, L.; Guo, Z.P.; Konstantinov, K.; Liu, H.K.; Dou, S.X. Nano-Structured Spherical Porous SnO2 Anodes for Lithium-Ion Batteries. J Power Sources 2006, 159, 345–348, doi:10.1016/j.jpowsour.2006.04.048.

185. Xu, G.-L.; Xu, Y.-F.; Sun, H.; Fu, F.; Zheng, X.-M.; Huang, L.; Li, J.-T.; Yang, S.-H.; Sun, S.-G. Facile Synthesis of Porous MnO/C Nanotubes as a High Capacity Anode Material for Lithium Ion Batteries. Chemical Communications 2012, 48, 8502, doi:10.1039/c2cc34218a.

186. Rahman, M.A.; Wen, C. A Study of the Capacity Fade of Porous NiO/Ni Foam as Negative Electrode for Lithium-Ion Batteries. Ionics (Kiel) 2016, 22, 173–184, doi:10.1007/s11581-015-1542-8.